UNIVERSITÀ DEGLI STUDI DI PARMA

Dottorato di Ricerca in Tecnologie dell'Informazione

XXVII Ciclo

KERR-INDUCED POLARIZATION ATTRACTION IN TELECOM FIBERS

Coordinatore:

Chiar.mo Prof. Marco Locatelli

Tutor:

Chiar.mo Prof. Armando Vannucci

Dottorando: *Matteo Barozzi*

Gennaio 2015

A Chiara

Alla Famiglia

Ad Armando

Contents

Introduction

The framework within which I have developed my research activity is that of the *transparent all-optical networks* of future generation. Such a technology represents a serious candidate for building network infrastructures supporting high data-rate communications, able to satisfy the growing demand for global data traffic transmission [1]. Current optical networks employ electronic devices to implement some signal processing and regeneration (as, e.g., add-drop multiplexing, ...). The use of electronic devices within an optical network, in addition to requiring the conversion of the signals carrying the information from the optical to the electrical domain (and vice-versa), imposes a limit on the maximum data-rate employable, given the limited operation bandwidth of such a devices. All-optical networks aim at eliminating the *bottleneck* given by the electronic devices, by directly implementing signal processing and regeneration in the optical domain, thus keeping the data signals entirely in the optical domain from source to destination; the latter property is referred to as *transparency*. The development of future transparent networks thus demands the availability of devices able to perform a *fast all-optical signal processing*, with low cost and energy consumption. Among these, I have concentrated my attention on optical devices able to perform a fast all-optical control of the state of polarization (SOP) of the signal.

Among the physical properties characterizing a light beam, i.e., the number of photons, the wavelength and the polarization, the last **"remains so far the most elusive uncontrolled variable, that one would like to control as finely as possible"** [2, 3], especially in optical fiber-based systems [4, 5]. In fact, an optical signal propagating in such a systems undergoes different polarization impairments, brought about by the fiber and by the other channels propagating within the same medium, that change the signal SOP unpredictably. In particular, despite the significant progress in optical fiber manufacturing, the residual birefringence of the medium and the linked polarization mode dispersion (PMD), which is a linear effect brought about

by the fiber, can spoil the signal SOP after propagating over a few hundred meters [4]. Moreover, in a multi-channels scenario, i.e., in a wavelength division multiplexing (WDM) optical system, each channel within the WDM comb nonlinearly interacts with the other channels. While self- and cross- phase modulation (SPM and XPM, respectively) are nonlinear scalar effect that do not affect the signal polarization, the cross-polarization modulation (XpolM) produces nonlinear polarization rotation (NPR) of the signal SOP depending on the power of the adjacent (in frequency) channels [4]. The unwanted variation of the signal polarization could be a problem in optical signal processing [6], since many devices are polarization sensitive (e.g., Nonlinear Optical Loop Mirror [7, 8], signal reshaping [9] or semiconductor optical amplifier (SOA) [10, 11]), as well as in optical coherent system, where the polarization fluctuations could dramatically affect the receiver's performance [12–15]. Below, I list a series of optical devices used to gain control over the SOP of light, classified according to their response time, i.e., their operation bandwidth, and their capability to preserve (or not) the signal intensity.

The simpler and most popular polarization controller is the *ideal (passive) polarizer*. Such a device is a polarization filter that suppresses all the polarization components of the signal, but the component aligned with its transparent eigenstate. Hence, the ideal polarizer transforms every input signal with a random distribution of its SOP into an output signal with a well-defined deterministic SOP, with a response time that could be considered instantaneous. On the other hand, all the signal power that is orthogonally polarized with respect to the transparent eigenstate, would be suppress by the ideal polarizer which thus causes a loss of signal power, called *polarization dependent loss* (PDL). For an unpolarized input signal beam, the ideal polarizer brings about (on average) a waste of 50% of the signal energy. Moreover, any fluctuation of the signal polarization is converted into a fluctuation of the signal intensity, that would lead to severe receiver's performance degradation [16]. All together, these considerations explain the actually limited use of the ideal polarizer within optical communications systems.

The first appearance of a polarization controller able to preserve the signal energy is due, to the best of my knowledge, to Heebner *et al.* [17], where it was experimentally demonstrated that the effect of two-wave mixing in a *photorefractive* material could be used for the amplification of one polarization component of a light beam by using the orthogonal component as a pump beam. The major advantage of this technique is that the energy of the beam is conserved in the repolarization process, as stated, hence the device developed by Heebner can be classified as a *nonlinear loss-*

less polarizer (NLP)[1]. Due to this conservation property, the NLP preserves the intensity of the outcoming beam, even if the polarization of the incoming beam changes with time. Moreover, NLPs offer a light-by-light control over the SOP of the signal beam, which provides a more robust, reliable, and potentially faster technology than what is available with mechanically or electrically controlled systems. On the other hand, the *photorefractive* material employed by Heebner needs a long transient time to reach an equilibrium state of the polarization, that ranges from few seconds to minutes [17]. Hence, the response time of such a device is incompatible with the speed demanded by the current optical transmission systems. Thus, with an eye toward *fast* optical control of the SOP, slow *photorefractive* materials should be changed to media with a faster nonlinear response. The immediate candidate is the optical fiber, with its virtually instantaneous nonlinearity.

The fiber-based polarization controllers could be classified in two categories, depending on the particular nonlinear effect that is exploited to control the polarization of the signal [3]. In nonlinear *active* polarizers, the control of the SOP is performed by exploiting a nonlinear (selective) amplification of one polarization component that is favorite, i.e., more amplified, with respect to the orthogonal component. Polarization controller devices belonging to this category can exploit the Raman [18–27], the Brillouin [28–30], or the parametric amplification of the signal [31–33]. Since these devices do not conserve the energy of the signal, due to the polarization-selective amplification, they introduce a *polarization dependent gain* (PDG) and thus suffer from a large amount of output relative intensity noise (RIN). Thus, as happens by employing an ideal polarizer, any fluctuation of the signal polarization is converted into a large fluctuation of the signal intensity. On the other hand, in (fiber-based) nonlinear lossless polarizers, the control of the SOP is performed by exploiting the Kerr nonlinearity of the optical fiber, hence the intensity of the signal is preserved. The response time of the fiber-based polarization controllers is compatible with the speeds needed to control the SOP in current and future optical networks, both for the active and for the lossless polarizers. Despite that, during my Ph.D., I focused my research activity mostly on the lossless polarizer devices. Since fiber-based NLPs allow to perform a fast control of the optical signal SOP, while preserving the signal intensity, it is my opinion that they represent a promising solution to be employed in transparent all-optical networks of future generation.

In particular, the fiber-based NLP perform polarization control by exploiting the physical phenomenon of *lossless polarization attraction* (LPA). LPA is a nonlin-

[1]Note the 50% threshold, explicitly mentioned in the title of Heebner's paper, for the power efficiency of the device, which is that of the ideal polarizer mentioned above.

ear two-channel phenomenon, based on the Kerr effect, occurring between the signal whose SOP has to be controlled and a fully-polarized continuous wave (CW) pump laser. Thanks to the interactions between signal and pump dictated by cross-polarization modulation (XpolM, i.e., the polarization-sensitive part of the Kerr effect), the signal SOP at the fiber output is attracted towards that of the controlling pump, regardless of the signal SOP at the fiber input, provided that the nonlinear fiber is randomly birefringent. Indeed, as I have pointed out during my research activity, the effectiveness of LPA strongly depends on the joint action between the XpolM effect and the relative propagation velocity between the signal and the pump, i.e., the signal-pump walk-off [34]. The first experimental demonstration of LPA occurring between signals at telecommunications wavelengths, instead, was obtained by injecting counter-propagating beams with large power (tens of Watt), into a short (2 m) isotropic fiber [6]. Anyway, it was the experimental observation of LPA between signals with moderate power (hundreds of milliWatt), counter-propagating in a long (20 km) birefringent telecom fiber [2] that has significantly spurred the intense research activity in the last five years. In fact, several research groups have produced both theoretical [35–40] and numerical analyses [34, 41–46], eventually leading to practical applications showing the potentials of the NLP [47–53]. The fully-polarized CW pump, in designing a NLP device, can either be injected at the opposite fiber end, with respect to the signal, thus implementing a *counter-propagating NLP*, or at the same fiber end with respect to the signal, thus implementing a *co-propagating NLP*. Within the original counter-propagating configuration of the NLP, LPA requires long (microseconds) transient times and large signal power (watts) [41], due to the relative propagation velocity between signal and pump imposed by the geometry, that is fixed and relativistic (i.e., equal to the speed of light). As a consequence, a counter-propagating NLP can repolarize only powerful signals with a slowly-varying polarization [46]. Instead, when pump and signal co-propagate, their relative propagation velocity can in turn be optimized (for given power levels), as a function of the symbol period [34]. As a consequence, a co-propagating NLP can repolarize also signals with a fast-varying polarization [45], and can employ lower power levels.

This thesis is organized as follows.

Chapter 1 reviews the theoretical frameworks I have used to study lossless polarization attraction. Here, I analyze the equation that governs the propagation of the field within an optical fiber. In particular, since I have been interested in studying polarization attraction induced by the Kerr nonlinearity of the fiber, I focus on a two channel scenario, where the optical fields propagate together within the fiber, in nonlinear regime. Finally, I define the analytical instruments that allow to quantify the

polarization attraction phenomenon, hence to quantify the performance of the nonlinear lossless polarizer device.

Chapter 2 discusses results regarding a counter-propagating nonlinear lossless polarizer. To solve numerically the counter-propagation of optical signals, I introduce a fast and simple iterative algorithm, based on the split-step Fourier method, named SCAOS, that has been conceived during my Ph.D. Resorting to the SCAOS algorithm, I characterize the performance of a counter-propagating NLP, thus providing the design guidelines to realize such a device.

Chapter 3 discusses results regarding the design of a co-propagating nonlinear lossless polarizer. First, I characterize the performance of the device as a function of the relative propagation velocity between signal and pump. At the same time, I shall cast new light on the central role of walk-off in the dynamics of lossless polarization attraction, by showing the interval of walk-off, in order to reach the polarization attraction regime. Moreover, I show how the NLP performance degrades when the device is realized by employing an optical fiber with high polarization mode dispersion. Finally, I introduce, for the first time to my knowledge, some early results regarding the NLP realized with two (or more) (co-polarized) pump lasers.

Chapter 4 presents a comprehensive picture of a noise cleaner device based on the nonlinear lossless polarizer, realized in either counter- or co-propagating configuration. The noise cleaner, that has been conceived during my Ph.D, is an all-optical fiber-based device able to enhance the optical signal-to-noise ratio (OSNR) of a (possibly depolarized) signal affected by unpolarized additive noise. I shall compare the two solutions, with counter- and co-propagating pump, for signals with a fast or slowly varying polarization. Moreover, I shall quantify the performance of the proposed noise cleaner by measuring the OSNR gain provided by it. Finally, I propose a method to theoretically estimate the OSNR gain achieved by the noise cleaner.

Finally, appendices report some useful matrix properties, that have been employed within the thesis.

Remarks on notation I adopted the following notation throughout this thesis. All vectors are denoted by an arrow, while unit magnitude vectors by an hat, except for 4-D Pauli vectors, which are underlined. Moreover, (2×1) (complex) Jones vectors are denoted by capital letters (e.g., $\overrightarrow{A}$ or $\hat{J}$), while (3×1) (real) Stokes vectors are denoted by lower-case letters (e.g., $\overrightarrow{a}$ or $\hat{j}$). The Stokes reference frame is defined according to the engineering notation, hence the first Stokes coordinate $\hat{s}_1$ represents the linear-horizontal polarization, while the third Stokes coordinate $\hat{s}_3$ represents the right-circular polarization. The (2×2) complex Jones matrices are de-

noted by bold-capital letters (e.g., **B**). The (2×2) Pauli matrices are denoted by σ_i, with $i=0,1,2,3$, where σ_0 is the (2×2) identity matrix, while the spin vector is denoted by $\overrightarrow{\sigma} \triangleq [\sigma_1,\sigma_2,\sigma_3]^T$. The Symbols $\cdot$ and $\times$ represent the scalar and cross product, respectively, symbol $*$ represents the convolution and symbol $\|\bullet\|$ represents the euclidean norm. Moreover, symbols $\langle a\rangle$ and $E[a]=\overline{a}$ represent the time- and statistical-average of a, respectively. Finally, symbol ^{T} represents the transpose operator, symbol * represents the conjugate operator and symbol † represents the adjoint operator, i.e., the transpose-conjugate.

Tables 1 and 2 summarize the notation adopted.

	Jones	Stokes
Vector	$\overrightarrow{A}$	$\overrightarrow{a}$
Unit magnitude vector	$\hat{f}$	$\hat{j}$
Matrix	**B**	$\mathscr{B}$

Table 1: Notation adopted to denote Jones and Stokes vectors or matrices.

	Symbols
Pauli matrices	σ_i, with $i=0,1,2,3$
Spin vector	$\overrightarrow{\sigma} \triangleq [\sigma_1,\sigma_2,\sigma_3]^T$
Transposed; Conjugate; Adjoint	$\overrightarrow{v}^T$; $\overrightarrow{v}^*$; $\overrightarrow{v}^\dagger$
Time-; Statistically-average	$\langle a\rangle$; $E[a]=\overline{a}$
Scalar-; Cross-product	$\overrightarrow{v}_1\cdot\overrightarrow{v}_2$; $\overrightarrow{v}_1\times\overrightarrow{v}_2$
Convolution; Euclidean norm	$a*b$; $\|\overrightarrow{v}\|$

Table 2: Symbols adopted throughout this thesis.

Chapter 1

Nonlinear polarization interactions

This chapter reviews the theoretical framework I have used to study lossless polarization attraction. As a first step, I will introduce the formalism used to describe the state of polarization of an optical field. Then, I will analyze the equation that governs the propagation of the field within an optical fiber. In particular, since I have been interested in studying polarization attraction induced by the Kerr nonlinearity of the fiber, I have focused on a probe-pump scenario, where the two optical fields propagate together within the fiber, in nonlinear regime. Finally, I will define the analytical instruments that allow to quantify the polarization attraction phenomenon, hence to quantify the performance of the nonlinear lossless polarizer device described within this thesis.

1.1 State of polarization

Let vector $\overrightarrow{E}(z,t)$ represent a continuous wave (CW) (transverse) optical field, propagating along the longitudinal direction $\hat{z}$ of the fiber, whose complex envelope $\overrightarrow{A}(z)$, constant in time, is such that

$$\overrightarrow{E}(z,t) = \Re\left\{\overrightarrow{A}(z)\, \mathrm{e}^{j(\omega_0 t - \beta_0 z)}\right\}, \tag{1.1}$$

where β_0 is the wavenumber at the carrier frequency ω_0. By decomposing the complex envelope $\overrightarrow{A}(z) = A_x(z)\hat{x} + A_y(z)\hat{y}$ in its two complex components $A_x(z)$ and $A_y(z)$ aligned along the orthogonal directions $\hat{x}$ and $\hat{y}$, respectively, which form the

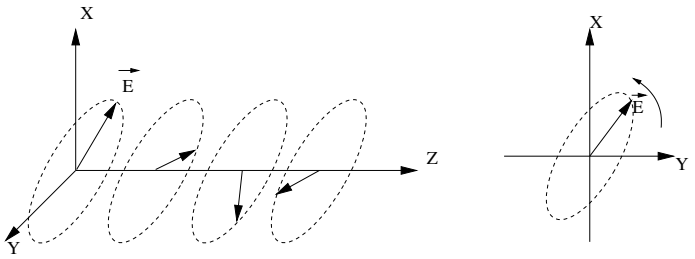

Figure 1.1: State of polarization of the optical field $\overrightarrow{E}(z,t)$: evolution along the propagation direction z (example).

transverse plane (orthogonal to the propagation direction $\hat{z}$, hence $\hat{x} = [1,0]^T$ and $\hat{y} = [0,1]^T$ correspond to the "canonical axes"), it can be written as

$$\overrightarrow{A}(z) = \begin{bmatrix} |A_x(z)|\, e^{j\phi_x(z)} \\ |A_y(z)|\, e^{j\phi_y(z)} \end{bmatrix}. \tag{1.2}$$

In (1.2), $|A_i(z)|$ and $\phi_i(z)$, with $i = x,y$, represent the amplitude and phase of the component i, respectively. From (1.2) and (1.1), the optical field $\overrightarrow{E}(z,t) = E_x(z,t)\hat{x} + E_y(z,t)\hat{y}$ can be expressed as a function of its (real) components, $E_x(z,t)$ and $E_y(z,t)$, as

$$\overrightarrow{E}(z,t) = \begin{bmatrix} |A_x(z)| \cos(\omega_0 t - \beta_0 z + \phi_x(z)) \\ |A_y(z)| \cos(\omega_0 t - \beta_0 z + \phi_y(z)) \end{bmatrix}. \tag{1.3}$$

In general, $E_x(z,t)$ and $E_y(z,t)$ oscillate, along the orthogonal directions $\hat{x}$ and $\hat{y}$, respectively, with different amplitudes ($|A_x(z)|$ and $|A_y(z)|$) and starting from different initial positions, identified by initial phases $\phi_x(0)$ and $\phi_y(0)$. Thus, at a given position z', the vector $\overrightarrow{E}(z',t)$ describes (in time) an elliptical trajectory in the transverse plane (x,y), that results in an helical trajectory followed by $\overrightarrow{E}(z,t)$ propagating along z, as shown in Fig. 1.1. The *state of polarization* (SOP) of the optical field describes the oscillations of the vector $\overrightarrow{E}(z,t)$ in the transverse plane (x,y). Polarization can be described with two formalisms, the Jones formalism or the Stokes formalism, which identify two *isomorphic* spaces where the SOP can be represented.

1.1.1 Jones formalism

Let me consider, without loss of generality, the complex envelope $\overrightarrow{A} \triangleq \overrightarrow{A}(0)$, at $z = 0$. By starting from (1.2), the field $\overrightarrow{A}$ can be written as

$$\overrightarrow{A} = A \begin{bmatrix} \cos\chi e^{j\phi_x} \\ \sin\chi e^{j\phi_y} \end{bmatrix} = A e^{j\bar{\phi}} \begin{bmatrix} \cos\chi \\ \sin\chi e^{j\phi} \end{bmatrix}, \tag{1.4}$$

where $A^2 = \left\| \overrightarrow{A} \right\|^2$ is the field intensity ($\|\bullet\|$ represents the euclidean norm), $\bar{\phi} \triangleq \phi_x$ is the "common" phase so that $\phi \triangleq \phi_y - \phi_x \in [-\pi; +\pi]$ is the differential phase and $\chi \in \left[0; \frac{\pi}{2}\right]$ is the angle defined as $\chi \triangleq \arctan\left(\frac{|A_y|}{|A_x|}\right)$[1]. In (1.4), the scalar term ($Ae^{j\bar{\phi}}$), i.e., the term common to both components of the field, and the vectorial term ($\left[\cos\chi, \sin\chi e^{j\phi}\right]^T$), i.e., the *differential* term between the two polarizations of the field, have been separated. Thus, the unit magnitude vector

$$\hat{f} \triangleq \begin{bmatrix} \cos\chi \\ \sin\chi e^{j\phi} \end{bmatrix} \in \mathbb{C}^2, \tag{1.5}$$

known as *Jones vector*, univocally identifies the SOP of the optical field $\overrightarrow{A}$ [54]. Vector $\hat{f}$ in (1.5) can be univocally identified by the two angles $\phi \in [-\pi; \pi]$ and $\chi \in [0; \pi/2]$, hence the SOP of the field only depends on the differential phase between the two components, $A_x(z)$ and $A_y(z)$, and on the ratio between their amplitudes. Fig. 1.2 shows a polarization ellipse, as an example.

In the literature, polarization is often identified by other two angles, the *azimuth* θ and the *ellipticity* ε, as shown in Fig. 1.3, so that the Jones vector results

$$\hat{f} = \begin{bmatrix} \cos\theta\cos\varepsilon - j\sin\theta\sin\varepsilon \\ \sin\theta\cos\varepsilon + j\cos\theta\sin\varepsilon \end{bmatrix} = \begin{bmatrix} \cos\theta & -\sin\theta \\ \sin\theta & \cos\theta \end{bmatrix} \begin{bmatrix} \cos\varepsilon \\ j\sin\varepsilon \end{bmatrix}. \tag{1.6}$$

Namely, the azimuth $-\frac{\pi}{2} \leq \theta \leq \frac{\pi}{2}$ is the angle between the positive direction x and the principal axis of the ellipse, aligned along x', thus it represents the ellipse orientation with respect to the standard reference (x, y). Instead, the *ellipticity* $\varepsilon \triangleq \arctan\left(\frac{b}{a}\right)$, where a (b) is the length of the major (minor) semi-axis of the ellipse, takes values in the range $-\frac{\pi}{4} \leq \varepsilon \leq \frac{\pi}{4}$ and represents the *eccentricity* of the ellipse. In particular, with $\varepsilon = 0$, independently of θ, the ellipse degenerates in a straight line, thus representing a *linear polarization*, while with $\varepsilon = \pi/4$, independently of θ, the

[1] The sign of A_x is attributed to the scalar amplitude A.

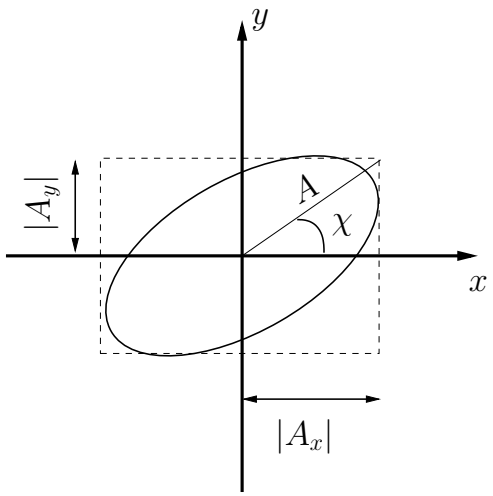

Figure 1.2: Polarization ellipse: the state of polarization (SOP) of the optical field is univocally determined by angles χ and ϕ (not shown).

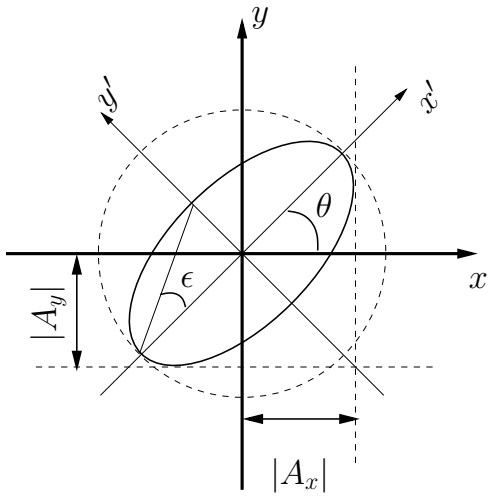

Figure 1.3: Polarization ellipse: the state of polarization (SOP) of the optical field is univocally determined by the *azimuth* θ and the *ellipticity* ε angles.

ellipse degenerates in a circle, thus representing a *circular polarization*. Finally, the sign of ε is related to the field's direction of rotation.

Whatever the form in which the Jones vector $\hat{J}$ is defined (as a function of (χ,ϕ) or (θ,ε)), the Jones vector $\hat{J}_o$ orthogonal to $\hat{J}$, is such that $\hat{J}^\dagger\hat{J}_o = \hat{J}_o^\dagger\hat{J} = 0$, where $\dagger$ represents the adjoint operator, hence the transposed and conjugate of a vector. The pair $\hat{J}$ and $\hat{J}_o$ form an orthonormal base for the SOP representation, obeying the "completeness relationship" $\hat{J}^\dagger\hat{J}_o + \hat{J}_o^\dagger\hat{J} = \sigma_0$, where σ_0 is the 2×2 identity matrix (see Appendix A).

1.1.2 Stokes formalism

Typically, in polarimetry, polarization is described by using the Stokes formalism, instead of the Jones formalism introduced in Sec. 1.1.1, since the SOP representation in the Stokes domain is more intuitive and geometrically meaningful.

In general, the "Jones-Stokes isomorphism" transforms a 2×1 complex vector $\overrightarrow{A}$ into a 4×1 real vector $\underline{a}$, by defining

$$a_i = \overrightarrow{A}^\dagger \sigma_i \overrightarrow{A}. \tag{1.7}$$

In (1.7), a_i represent the (real) components ($i = 0,...,3,$) of vector $\underline{a}$, while σ_i represent the *Pauli matrices*, defined in Appendix A. By applying transformation (1.7) to vector $\overrightarrow{A} = \overrightarrow{A}(0)$, as defined in (1.2), vector $\underline{a}$ results

$$\underline{a} = \begin{bmatrix} a_0 \\ a_1 \\ a_2 \\ a_3 \end{bmatrix} = \begin{bmatrix} |A_x|^2 + |A_y|^2 \\ |A_x|^2 - |A_y|^2 \\ 2\Re\{A_x^* A_y\} \\ 2\Im\{A_x^* A_y\} \end{bmatrix} = \begin{bmatrix} A^2 \\ |A_x|^2 - |A_y|^2 \\ A_y^* A_x + A_y A_x^* \\ j\left(A_y^* A_x - A_y A_x^*\right) \end{bmatrix}. \tag{1.8}$$

As stated, all coefficients a_i are real, due to the Pauli matrices which are hermitian (so that $a_i = a_i^\dagger = a_i^*$, in (1.7)), and they can be measured in a laboratory by using a polarimeter. Moreover, from (1.8), coefficients a_i satisfy the relation $a_0^2 = \sum_{i=1}^3 a_i^2$, where $a_0 = A^2$ is the field intensity ($\left\|\overrightarrow{A}\right\|^2$), meaning that the optical field $\overrightarrow{A}$ can be completely represented, in the Stokes domain, by the *Stokes vector* $\overrightarrow{a} \in \mathbb{R}^3$, whose elements are $\overrightarrow{a} = [a_1, a_2, a_3]^T$ (^{T} represents the transposed of a vector), as defined in (1.8). By factoring out the field intensity $a_0 = \|\overrightarrow{a}\|$, the Stokes vector can be written as $\overrightarrow{a} = a_0\hat{j}$, where $\hat{j} \in \mathbb{R}^3$ is the unit magnitude vector which identifies the field SOP. As a consequence, the Stokes vector $\hat{j}$, hence the field SOP, can be visualized on a unitary-radius sphere, called the *Poincaré sphere*, whose reference axes are

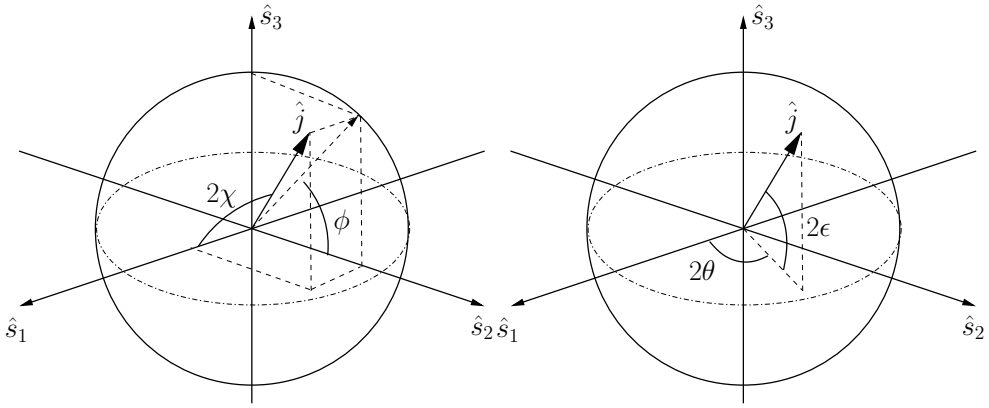

Figure 1.4: Poincaré sphere: the state of polarization (SOP) of the optical field is univocally determined by the Stokes vector $\hat{j}$, expressed as a function of angles (χ,ϕ) (left) or (θ,ε) (right).

$(\hat{s}_1,\hat{s}_2,\hat{s}_3)$. Starting from the Jones versor $\hat{J}$ expressed as a function of angles (χ,ϕ), as in (1.5), or (θ,ε), as in (1.6), the corresponding Stokes vector $\hat{j}$ can be expressed in two different ways:

$$\hat{j} = \begin{bmatrix} \cos(2\chi) \\ \sin(2\chi)\cos\phi \\ \sin(2\chi)\sin\phi \end{bmatrix} = \begin{bmatrix} \cos(2\theta)\cos(2\varepsilon) \\ \sin(2\theta)\cos(2\varepsilon) \\ \sin(2\varepsilon) \end{bmatrix}.$$

Figure (1.4) shows an example of the Stokes vector $\hat{j}$, expressed as a function of angles (χ,ϕ) (left) or (θ,ε) (right), visualized on the Poincaré sphere. Note that all angles, but the differential phase ϕ, are doubled in the transformation from Jones to Stokes domain. The locus of points that lies on the equator of the sphere, characterized by $\varepsilon = 0$, represents all the linear polarizations, while the poles of the sphere $\pm\hat{s}_3$, characterized by $\varepsilon = \pm\pi/2$, represent the circular polarizations. Any other point on the Poincaré sphere represents an elliptical polarization, characterized by $0 < |\varepsilon| < \pi/4$. Moreover, the Jones vector $\hat{J}_o$ orthogonal to $\hat{J}$ becomes the opposite vector in Stokes domain, hence $\hat{j}_o = -\hat{j}$.

Table (1.1) reports some special SOPs, which are pairwise orthonormal (hence which form an orthonormal basis for the SOP representation), along with the corresponding Jones and Stokes vectors.

SOP	$\hat{J}$	$\hat{j}$	(χ,ϕ)	(θ,ε)
Linear Horizontal (LH)	$\hat{x}=\begin{bmatrix}1\\0\end{bmatrix}$	$\hat{s}_1=\begin{bmatrix}1\\0\\0\end{bmatrix}$	$(0,\forall)$	$(0,0)$
Linear Vertical (LV)	$\hat{y}=\begin{bmatrix}0\\1\end{bmatrix}$	$-\hat{s}_1=\begin{bmatrix}-1\\0\\0\end{bmatrix}$	$(\frac{\pi}{2},\forall)$	$(\pm\frac{\pi}{2},0)$
Linear +45°	$\frac{1}{\sqrt{2}}\begin{bmatrix}1\\1\end{bmatrix}$	$\hat{s}_2=\begin{bmatrix}0\\1\\0\end{bmatrix}$	$(\frac{\pi}{4},0)$	$(\frac{\pi}{4},0)$
Linear -45°	$\frac{1}{\sqrt{2}}\begin{bmatrix}1\\-1\end{bmatrix}$	$-\hat{s}_2=\begin{bmatrix}0\\-1\\0\end{bmatrix}$	$(\frac{\pi}{4},\pm\pi)$	$(-\frac{\pi}{4},0)$
Right Circular (RC)	$\frac{1}{\sqrt{2}}\begin{bmatrix}1\\j\end{bmatrix}$	$\hat{s}_3=\begin{bmatrix}0\\0\\1\end{bmatrix}$	$(\frac{\pi}{4},\frac{\pi}{2})$	$(\forall,\frac{\pi}{4})$
Left Circular (LC)	$\frac{1}{\sqrt{2}}\begin{bmatrix}1\\-j\end{bmatrix}$	$-\hat{s}_3=\begin{bmatrix}0\\0\\-1\end{bmatrix}$	$(\frac{\pi}{4},-\frac{\pi}{2})$	$(\forall,-\frac{\pi}{4})$

Table 1.1: Significant state of polarization (SOP).

1.1.3 Degree of polarization

Until now, I have considered a continuous wave optical field, whose complex envelope $\overrightarrow{A}$ is constant in time. By removing this hypothesis, hence considering a time-varying Jones vector $\overrightarrow{A}(t)$, the corresponding Stokes vector $\overrightarrow{a}(t)$ is also time-varying, hence its time-average $\langle \overrightarrow{a}(t) \rangle$ can be evaluated. Thus, the time-averaged Stokes parameters $\langle a_i(t) \rangle$ are

$$\langle a_i(t) \rangle \triangleq \frac{1}{T} \int_0^T a_i(t) dt, \tag{1.9}$$

where T is the averaging interval. In such a case, the relation between time-averaged Stokes parameters becomes $\langle a_0(t) \rangle = \langle \| \overrightarrow{a}(t) \| \rangle \geq \| \langle \overrightarrow{a}(t) \rangle \|$, where the equal sign holds if and only if $\overrightarrow{a}(t)$ is constant in time (as for a CW field). The ratio between $\| \langle \overrightarrow{a}(t) \rangle \|$ and $\langle a_0(t) \rangle$, when $T \to \infty$, defines the *degree of polarization* (DOP) [55] of the field

$$\mathrm{DOP} \triangleq \frac{\| \langle \overrightarrow{a}(t) \rangle \|}{\langle a_0(t) \rangle}. \tag{1.10}$$

The DOP quantifies the variations of the signal polarization in time and takes values in the range $[0;1]$. For a fully-polarized field, $\mathrm{DOP} = 1$, meaning that $\overrightarrow{a}(t)$ is constant in time and it is represented by a single point on the Poincaré sphere, while for an unpolarized field, $\mathrm{DOP} = 0$, meaning that $\overrightarrow{a}(t)$ is represented by a cloud of points that uniformly cover the Poincaré sphere. For a partially depolarized field, $0 < \mathrm{DOP} < 1$, meaning that $\overrightarrow{a}(t)$ is represented by a cloud of scattered points.

1.2 Nonlinear propagation in optical fibers

1.2.1 Vectorial nonlinear Schroedinger equation

In this section, I introduce the vectorial (or coupled) nonlinear Schroedinger equation (VNLSE), that governs the nonlinear propagation of a signal within an optical fiber. Since I am interested in studying polarization attraction generated by the Kerr-induced polarization interactions between two signals, I will concentrate here on the nonlinear term of the VNLSE, that governs signals propagation in nonlinear regime.

Let $\overrightarrow{A}(0,t)$ be the complex envelope of the optical field (in Jones domain) at the

fiber input; the VNLSE for $\overrightarrow{A}(z,t)$ can be written as [56]

$$\begin{aligned}\frac{\partial \overrightarrow{A}(z,t)}{\partial z} &= -\frac{\alpha}{2}\overrightarrow{A}(z,t) - j\mathbf{B}(z,t) * \overrightarrow{A}(z,t) - \\ &\quad -j\gamma\left\{\frac{2}{3}\left\|\overrightarrow{A}(z,t)\right\|^2 \overrightarrow{A}(z,t) + \frac{1}{3}\overrightarrow{A}^*(z,t)\overrightarrow{A}^T(z,t)\overrightarrow{A}(z,t)\right\}, \quad (1.11)\end{aligned}$$

where the term $-\frac{\alpha}{2}\overrightarrow{A}(z,t) - j\mathbf{B}(z,t) * \overrightarrow{A}(z,t)$, that governs the linear propagation of $\overrightarrow{A}(z,t)$, includes the fiber attenuation α and the 2×2 birefringence matrix $\mathbf{B}(z,t)$, while the term $-j\gamma\left\{\frac{2}{3}\left\|\overrightarrow{A}(z,t)\right\|^2 \overrightarrow{A}(z,t) + \frac{1}{3}\overrightarrow{A}^*(z,t)\overrightarrow{A}^T(z,t)\overrightarrow{A}(z,t)\right\}$, that governs the nonlinear propagation of $\overrightarrow{A}(z,t)$, is proportional to the nonlinear Kerr coefficient γ. Moreover, symbol $*$ represents the convolution, $\|\cdot\|$ represents the euclidean norm, ^{T} represents the transposed operator and * represents the complex conjugate.

Since I concentrate here on the nonlinear propagation of the optical field, I assume to remove, for the moment, the linear term of (1.11), so that it becomes

$$\frac{\partial \overrightarrow{A}(z,t)}{\partial z} = -j\gamma e^{-\alpha z}\left\{\frac{2}{3}\left\|\overrightarrow{A}(z,t)\right\|^2 \overrightarrow{A}(z,t) + \frac{1}{3}\overrightarrow{A}^*(z,t)\overrightarrow{A}^T(z,t)\overrightarrow{A}(z,t)\right\}. \quad (1.12)$$

In (1.12), the scalar term $e^{-\alpha z}$ accounts for power attenuation of the field due to the fiber loss α. Note that in the transition from (1.11) to (1.12), I apply the change of variable $\overrightarrow{A}'(z,t) = e^{-\frac{\alpha}{2}z}\overrightarrow{A}(z,t)$, from the unattenuated field $\overrightarrow{A}(z,t)$, in (1.11), to the attenuated field $\overrightarrow{A}'(z,t)$, in (1.12). However, in order not to overburden the notation, I keep using the notation $\overrightarrow{A}(z,t)$ to refer to the attenuated field in (1.12). If $\overrightarrow{A}(z,t)$ refers to the unattenuated or to the attenuated field it is clear from the equation; if the term $\frac{\alpha}{2}\overrightarrow{A}(z,t)$ appears (as in (1.11)), $\overrightarrow{A}(z,t)$ refers to the unattenuated field, while if the term $e^{-\alpha z}$ appears (as in (1.12)), $\overrightarrow{A}(z,t)$ refers to the attenuated field.

Manipulating the two terms (in curly brackets) on the right-hand side of (1.12), they can be both written as a function of the *projector matrix* $P_A \triangleq \overrightarrow{A}\overrightarrow{A}^\dagger$ and its transposed $P_A^T = \overrightarrow{A}^*\overrightarrow{A}^T$ (defined in Appendix A). In fact, by recognizing that $\left\|\overrightarrow{A}(z,t)\right\|^2 = \overrightarrow{A}^\dagger(z,t)\overrightarrow{A}(z,t)$, the first term becomes $\left\|\overrightarrow{A}(z,t)\right\|^2 \overrightarrow{A}(z,t) = P_A(z,t)\overrightarrow{A}(z,t)$. On the other hand, the second term becomes $\overrightarrow{A}^*(z,t)\overrightarrow{A}^T(z,t)\overrightarrow{A}(z,t) = P_A^T(z,t)\overrightarrow{A}(z,t) = (P_A(z,t) - a_3\sigma_3)\overrightarrow{A}(z,t)$, where a_3 is the third component (related to the field ellipticity) of the signal Stokes vector $\overrightarrow{a}(z,t)$ and σ_3 is the third Pauli matrix (see Appendix

A). Hence, by using the projector as above, (1.12) can be written as

$$\frac{\partial \overrightarrow{A}(z,t)}{\partial z} = -j\gamma e^{-\alpha z}\left\{P_A(z,t) - \frac{1}{3}a_3(z,t)\sigma_3\right\}\overrightarrow{A}(z,t). \tag{1.13}$$

Finally, by exploiting the property of the projector matrix for which $P_A\overrightarrow{A} = a_0\overrightarrow{A}$ (where $a_0 = \left\|\overrightarrow{A}\right\|^2$ is the signal intensity), equation (1.13) becomes

$$\frac{\partial \overrightarrow{A}(z,t)}{\partial z} = -j\gamma e^{-\alpha z}\left\{a_0(z,t)\sigma_0 - \frac{1}{3}a_3(z,t)\sigma_3\right\}\overrightarrow{A}(z,t). \tag{1.14}$$

Equation (1.14) is an hybrid form of the VNLSE, since the optical field appears both in Jones coordinates $\overrightarrow{A}(z,t)$ and in Stokes coordinates $a_i(z,t)$ (in particular, only the signal intensity a_0 and the third Stokes coordinate a_3 appears in (1.14))[2].

Equation (1.14) means that an optical signal propagating in nonlinear regime undergoes two "separate" effects, taken into account by the two terms in curly brackets, $a_0\sigma_0$ and $\frac{1}{3}a_3\sigma_3$. The first term, proportional to a_0, implies a scalar phase distortion of $\overrightarrow{A}(z,t)$, hence it does not affect the field polarization. In the literature, this term is known as *self phase modulation* (SPM), since the phase distortion of the field $\overrightarrow{A}(z,t)$ is proportional to its own intensity a_0. The second term, proportional to $a_3\sigma_3$, can be written as $a_3\hat{s}_3\cdot\overrightarrow{\sigma}$, where $\hat{s}_3$ is the third Stokes axis of the reference system, $\overrightarrow{\sigma}$ is the spin vector (defined in Appendix A) and $\cdot$ represents the inner product; it indicates a *nonlinear polarization rotation* (NPR) of $\overrightarrow{A}(z,t)$, which thus affects the signal polarization. More details about the dynamics of the NPR are given below.

Moreover, (1.14) highlights that the nonlinear response of the fiber to a powerful propagating signal depends on the polarization of the signal. Assuming, for example, $\overrightarrow{A}(0,t)$ is linearly polarized, the third Stokes component of the vector $\overrightarrow{a}$ is $a_3 = 0$, hence (1.14) reduces to $\frac{\partial \overrightarrow{A}(z,t)}{\partial z} = -j\gamma e^{-\alpha z}a_0\overrightarrow{A}(z,t)$. On the other hand, assuming $\overrightarrow{A}(0,t)$ is circularly polarized, all signal intensity is aligned along the third Stokes component $\hat{s}_3$, hence vector $\overrightarrow{a} = a_3\hat{s}_3$, with $a_3 = a_0$; thus, (1.14) reduces to $\frac{\partial \overrightarrow{A}(z,t)}{\partial z} = -j\frac{2}{3}\gamma e^{-\alpha z}a_0\overrightarrow{A}(z,t)$. In both cases, (1.14) implies a scalar phase distortions (SPM), without any NPR effect, but the strength of the distortion differs in the two cases. For a linearly polarized field, the strength of the SPM is proportional to the

[2]Knowing that $a_3(z,t) = \left(\overrightarrow{A}^{\dagger}(z,t)\sigma_3\overrightarrow{A}(z,t)\right)$, it is possible write (1.14) in terms of the Jones field $\overrightarrow{A}(z,t)$ only, as $\frac{\partial \overrightarrow{A}(z,t)}{\partial z} = -j\gamma e^{-\alpha z}\left\{\left\|\overrightarrow{A}(z,t)\right\|^2\sigma_0 - \frac{1}{3}\left(\overrightarrow{A}^{\dagger}(z,t)\sigma_3\overrightarrow{A}(z,t)\right)\sigma_3\right\}\overrightarrow{A}(z,t)$ [57].

nonlinear coefficient γ, while for a circularly polarized field, the strength of the SPM is proportional to a "new" nonlinear coefficient $\gamma' \triangleq \frac{2}{3}\gamma$, that is weaker with respect to γ. Generalizing, for an elliptically polarized optical field $\overrightarrow{A}(0,t)$, the fiber nonlinearity involves both SPM and NPR and the strength of SPM would be proportional to a nonlinear coefficient $\gamma' = g\gamma$, with $\frac{2}{3} < g < 1$.

Equation of motion

To understand how the signal SOP evolves during the nonlinear propagation within the optical fiber, it is useful to translate the propagation equation (1.14), for the Jones field $\overrightarrow{A}(z,t)$, in the *equation of motion* for the Stokes vector $\overrightarrow{a}(z,t)$. By exploiting the conversion rule reported in Appendix A and recognizing that $h_0 = h_{0r} = 2\gamma e^{-\alpha z} a_0$ and $\overrightarrow{h} = -\frac{2}{3}\gamma e^{-\alpha z} a_3 \hat{s}_3$, the equation of motion for $\overrightarrow{a}(z,t)$ results

$$\frac{\partial \overrightarrow{a}(z,t)}{\partial z} = -\frac{2}{3}\gamma e^{-\alpha z} a_3(z,t)\left[\hat{s}_3 \times \overrightarrow{a}(z,t)\right], \tag{1.15}$$

where $\times$ represents the cross product. Equation (1.15) implies a rotation of $\overrightarrow{a}(z,t)$ around the third Stokes axis $\hat{s}_3$, thereby keeping the third Stokes coordinate $a_3(z,t)$ of $\overrightarrow{a}(z,t)$ constant along the fiber, hence equal to $a_3(0,t)$. Thus, the exact solution of (1.15) for $\overrightarrow{a}(z,t)$ results

$$\overrightarrow{a}(z,t) = e^{-\frac{2}{3}\gamma a_3(0,t) L_{eff}[\hat{s}_3\times]}\overrightarrow{a}(0,t), \tag{1.16}$$

that represents the rotation of $\overrightarrow{a}(z,t)$ around $\hat{s}_3$ of an angle $\varphi = -\frac{2}{3}\gamma a_3(0,t) L_{eff}$ ($L_{eff} \triangleq (1-e^{-\alpha z})/\alpha$ is the effective fiber length) proportional to the ellipticity $a_3(0,t)$ of the input optical field. Fig. (1.5) shows an example of the Stokes vector evolution, on the Poincaré sphere, for a CW input signal $\overrightarrow{a}(0,t) = \overrightarrow{a}(0)$ elliptically polarized (left), linearly polarized (center) and circularly polarized (right). Without loss of generality, in Fig. (1.5) the signal intensity $a_0 = 1$, so that vector $\overrightarrow{a}$ lies on the sphere. As can be seen, only elliptically polarized signals undergo nonlinear polarization rotation.

1.2.2 The Manakov-PMD equation

In Sec. (1.2.1), I concentrated on the nonlinear term of the VNLSE only. Here, the case where the linear and nonlinear terms of the VNLSE are both present is considered. In this case, the polarization of the signal $\overrightarrow{A}(z,t)$ changes, during the propagation within the fiber, even because of the birefringence (linear term represented

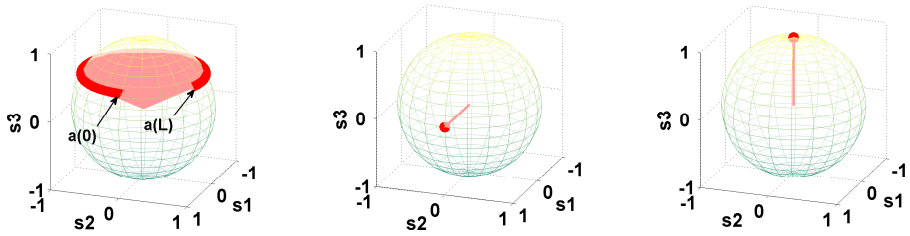

Figure 1.5: Evolution of the Stokes vector $\overrightarrow{a}(z,t)$, on the Poincaré sphere, governed by the VNLSE. The CW input signal $\overrightarrow{a}(0)$, with unit magnitude, is elliptically polarized (left), linearly polarized (center) or circularly polarized (right).

by matrix **B**), in addition to the nonlinear effect (NPR). Since the nonlinear term of the VNLSE depends on the signal polarization, whenever the signal SOP changes due to the birefringence, the strength of nonlinearity ($\gamma' = g\gamma$) changes accordingly. For a long fiber (at least a few kilometers) with a sufficient random birefringence (as in typical telecom fibers), it can be assumed that the polarization of the signal is scattered, due to the birefringence, on the whole Poincaré sphere [58]. Thus, the polarization of the signal can be assumed as a random variable, uniformly distributed on the Poincaré sphere. By applying this assumption, the right-hand side of equation (1.14) can be averaged with respect to the signal polarization, as follows [58]

$$\begin{aligned} E[NL] &= -j\gamma e^{-\alpha z}\left\{a_0(z,t)\sigma_0\overrightarrow{A}(z,t) - \frac{1}{3}E\left[a_3(z,t)\sigma_3\overrightarrow{A}(z,t)\right]\right\} \\ &= -j\frac{8}{9}\gamma e^{-\alpha z}a_0(z,t)\overrightarrow{A}(z,t), \end{aligned} \tag{1.17}$$

where $E[\cdot]$ represents the expectation operator. A rigorous proof of such an average operation has been given in [58][3]. Nevertheless, below I provide an intuitive proof of (1.17). Specifically, for a signal whose polarization is uniformly distributed on the Poincaré sphere, it can be assumed that signal intensity a_0 is uniformly distributed among the three signal Stokes coordinates a_i, $(i = 1,...,3)$. Hence, each Stokes coordinate a_i, on average, "weights" one third with respect to the signal intensity a_0. Thus, the average $E\left[a_3\sigma_3\overrightarrow{A}(z,t)\right]$ becomes $\frac{1}{3}a_0\overrightarrow{A}(z,t)$.

[3] In order for the average operation to be meaningful, we should assume that the "nonlinear length" L_{NL}, i.e., the fiber length over which nonlinear effects become appreciable, is much larger than the "beat length" L_B, i.e., the fiber length over which the SOP varies significantly. As stated, this condition, $L_{NL} \gg L_B$, is met by standard telecom fibers, which are moderately nonlinear and randomly birefringent.

The complete propagation equation, with the approximated nonlinear term as in (1.17), results

$$\frac{\partial \overrightarrow{A}(z,t)}{\partial z} = -\frac{\alpha}{2}\overrightarrow{A}(z,t) - j\mathbf{B}(z,t) * \overrightarrow{A}(z,t) - j\frac{8}{9}\gamma \left\| \overrightarrow{A}(z,t) \right\|^2 \overrightarrow{A}(z,t). \qquad (1.18)$$

Equation (1.18) is the well-known *Manakov-PMD equation* [58], a simplification of the VNLSE which holds for long randomly birefringent fibers, that differs from the VNLSE (1.11) only in the nonlinear term. In (1.18), the nonlinearity reduces to a simple scalar phase distortion (SPM) of $\overrightarrow{A}(z,t)$, whose strength is proportional to the nonlinear coefficient $\gamma' = \frac{8}{9}\gamma$ (hence $\frac{2}{3} < g = \frac{8}{9} < 1$), for every signal polarizations. As opposed to the VNLSE, in the Manakov-PMD equation the nonlinear polarization rotation is absent, hence the signal polarization changes only because of the fiber birefringence (linear effect), during the propagation.

Manakov-PMD equation (1.18) is simpler and faster to solve numerically, with respect to the VNLSE (1.11), but it can be used only if the birefringence of the fiber is sufficiently random to make the signal SOP uniformly distributed over the Poincaré sphere, so that the nonlinearity of the fiber "sees" only an average signal SOP. Otherwise, for example in a polarization maintaining fiber or in a short isotropic fiber, signal propagation is governed by the VNLSE, hence Manakov-PMD equation cannot be used. Typically, in telecom systems, a randomly birefringent fiber is employed, hence signal propagation can be numerically solved by the Manakov-PMD equation.

1.2.3 Multi-channel propagation: probe-pump scheme

The VNLSE (1.11) and the Manakov-PMD equation (1.18) govern the optical signals propagation when the signal $\overrightarrow{A}$ propagates alone within the fiber, hence when a *single channel* scenario is considered. As already stated, the lossless polarization attraction process is a *two-channel* phenomenon, since LPA is generated by the (nonlinear) interaction between the signal and a pump laser. Hence, in this section, I am going to show how the propagation equation, either the VNLSE (1.11) or the Manakov-PMD (1.18), changes when two signals propagate together within the same optical fiber.

To start the analysis, I assume that two separated channels are injected into the fiber, the probe channel $\overrightarrow{A}_s(0,t)$ and the pump channel $\overrightarrow{A}_p(0,t)$, so that the complex envelope of the overall optical field $\overrightarrow{A}(0,t)$, at the fiber input, can be written as

$$\vec{A}(0,t) = \overrightarrow{A}_s(0,t) + \overrightarrow{A}_p(0,t)\mathrm{e}^{j\Delta\omega t}. \qquad (1.19)$$

In (1.19), the low-pass frequency ω is evaluated with respect to the probe carrier frequency ω_0, hence $\Delta\omega$ represents the frequency displacement between the probe

channel and the pump. Moreover, I assume that each separate channel is isolated by an optical filter centered on each channel frequency, at the fiber output (ω_0 for the probe or $\omega_0 + \Delta\omega$ for the pump).

To obtain the propagation equations for the probe and for the pump, either from the VNLSE or the Manakov-PMD equation, substitute optical field (1.19) in (1.11) or (1.18), respectively. Considering probe and pump propagating in linear regime, they undergo the same (linear) impairments in both VNLSE and Manakov frameworks (compare (1.11) and (1.18)). Moreover, due to the superposition of effects, probe and pump do not affect each other during linear propagation, hence each channel propagates as a single channel. Thus, by isolating the terms at $\omega = 0$ for the probe and $\omega = \Delta\omega$ for the pump, the linear term of the propagation equation, either for the VNLSE or the Manakov-PMD, can be written as

$$\frac{\partial \overrightarrow{A}_i(z,t)}{\partial z} = -\frac{\alpha}{2}\overrightarrow{A}_i(z,t) - j\mathbf{B}_i(z,t) * \overrightarrow{A}_i(z,t), \tag{1.20}$$

where $i = s, p$, thus representing the probe (s) or the pump (p) channel, while $\mathbf{B}_i$ represent the different birefringence acting on probe and pump: namely, $\mathbf{B}_p(z,t) = \mathbf{B}_s(z,t)\mathrm{e}^{-j\Delta\omega t}$, and $\mathbf{B}_s(z,t) = \mathbf{B}(z,t)$ is the original matrix appearing in (1.18).

This is no longer true when the signals propagate in nonlinear regime, where probe and pump (nonlinearly) interact. Since the Manakov nonlinear term (1.17) is contained in that of the VNLSE (1.12), I concentrate on the VNLSE equation for calculations. Hence, by considering the nonlinear equation (1.12) written for field in (1.19):

$$\begin{aligned}\frac{\partial \overrightarrow{A}_s}{\partial z} + \frac{\partial \overrightarrow{A}_p}{\partial z}\mathrm{e}^{j\Delta\omega t} &= -j\gamma\mathrm{e}^{-\alpha z}\left\{\frac{2}{3}\left\|\overrightarrow{A}_s + \overrightarrow{A}_p\mathrm{e}^{j\Delta\omega t}\right\|^2\left(\overrightarrow{A}_s + \overrightarrow{A}_p\mathrm{e}^{j\Delta\omega t}\right) + \right. \\ &\left. + \frac{1}{3}\left(\overrightarrow{A}_s + \overrightarrow{A}_p\mathrm{e}^{j\Delta\omega t}\right)^*\left(\overrightarrow{A}_s + \overrightarrow{A}_p\mathrm{e}^{j\Delta\omega t}\right)^T\left(\overrightarrow{A}_s + \overrightarrow{A}_p\mathrm{e}^{j\Delta\omega t}\right)\right\}. \end{aligned} \tag{1.21}$$

In (1.21) I omitted the dependence on z and t of probe and pump, for simplicity of notation. By expliciting all vectorial products between the terms within the curly brackets on the right-hand side of (1.21), the nonlinear interactions between probe and pump generate contributions at different frequencies, listed below.

1. Probe frequency $\omega = 0$. The terms that give contributions within the probe bandwidth are $\left(\overrightarrow{A}_s^{\dagger}\overrightarrow{A}_s\overrightarrow{A}_s\right)$, $\left(\overrightarrow{A}_p^{\dagger}\overrightarrow{A}_s\overrightarrow{A}_p\right)$ and $\left(\overrightarrow{A}_p^{\dagger}\overrightarrow{A}_p\overrightarrow{A}_s\right)$, which are common to both the VNLSE and the Manakov-PMD (since they derive from the first term in curly brackets); the terms $\left(\overrightarrow{A}_s^{*}\overrightarrow{A}_s^{T}\overrightarrow{A}_s\right)$ and $2\left(\overrightarrow{A}_p^{*}\overrightarrow{A}_p^{T}\overrightarrow{A}_s\right)$ appear only in the VNLSE (since they derive from the second term in curly brackets).

2. Pump frequency $\omega = \Delta\omega$. The terms that give contributions within the pump bandwidth are $\left(\overrightarrow{A}_p^{\dagger}\overrightarrow{A}_p\overrightarrow{A}_p\right)$, $\left(\overrightarrow{A}_s^{\dagger}\overrightarrow{A}_p\overrightarrow{A}_s\right)$ and $\left(\overrightarrow{A}_s^{\dagger}\overrightarrow{A}_s\overrightarrow{A}_p\right)$ (common to both the VNLSE and the Manakov-PMD); the terms $\left(\overrightarrow{A}_p^{*}\overrightarrow{A}_p^{T}\overrightarrow{A}_p\right)$ and $2\left(\overrightarrow{A}_s^{*}\overrightarrow{A}_s^{T}\overrightarrow{A}_p\right)$ (which appear only in the VNLSE).

3. Frequency $\omega = 2\Delta\omega$. The term $\left(\overrightarrow{A}_s^{\dagger}\overrightarrow{A}_p\overrightarrow{A}_p\right)$ (common to both the VNLSE and the Manakov-PMD); the term $\left(\overrightarrow{A}_s^{*}\overrightarrow{A}_p^{T}\overrightarrow{A}_p\right)$ (which appears only in the VNLSE).

4. Frequency $\omega = -\Delta\omega$. The term $\left(\overrightarrow{A}_p^{\dagger}\overrightarrow{A}_s\overrightarrow{A}_s\right)$ (common to both the VNLSE and the Manakov-PMD); the term $\left(\overrightarrow{A}_p^{*}\overrightarrow{A}_s^{T}\overrightarrow{A}_s\right)$ (which appears only in the VNLSE).

Note that, while at the fiber input there are only two frequencies, $\omega = 0$ and $\omega = \Delta\omega$ for probe and pump, respectively, at the fiber output other two contributions arise at the *four-wave mixing* frequencies $\omega = 2\Delta\omega$ and $\omega = -\Delta\omega$, due to the nonlinear interaction between the two channels. Moreover, the contributions at the probe and pump frequencies are specular, hence once calculated for one field, they can be obtained from the other by just changing s into p and vice-versa. Thus, by considering only the propagation equation for the probe channel, hence by taking into account only the terms that give contributions within the probe bandwidth ($\omega = 0$), the (nonlinear) propagation equations VNLSE and Manakov can be written, in a two channel scenario, as

$$VNLSE \quad \frac{\partial\overrightarrow{A}_s(z,t)}{\partial z} = -j\gamma e^{-\alpha z}\left\{\frac{2}{3}\left[\left\|\overrightarrow{A}_s\right\|^2+\left\|\overrightarrow{A}_p\right\|^2+P_p\right]\overrightarrow{A}_s+\frac{1}{3}\left[P_s^T+2P_p^T\right]\overrightarrow{A}_s\right\} \tag{1.22}$$

$$Manakov \quad \frac{\partial\overrightarrow{A}_s(z,t)}{\partial z} = -j\gamma e^{-\alpha z}\frac{8}{9}\left[\left\|\overrightarrow{A}_s\right\|^2+\left\|\overrightarrow{A}_p\right\|^2+P_p\right]\overrightarrow{A}_s \tag{1.23}$$

In (1.22) and (1.23) it is recognized that $\overrightarrow{A}_i^{\dagger}\overrightarrow{A}_i = \left\|\overrightarrow{A}_i\right\|^2$ (for $i = s,p$), $\overrightarrow{A}_p^{\dagger}\overrightarrow{A}_s\overrightarrow{A}_p = \overrightarrow{A}_p\overrightarrow{A}_p^{\dagger}\overrightarrow{A}_s = P_p\overrightarrow{A}_s$ and $\overrightarrow{A}_i^{*}\overrightarrow{A}_i^{T} = P_i^T$ (for $i = s,p$), where P_p is the projector matrix for the pump vector $\overrightarrow{A}_p$, while P_i^T (for $i = s,p$) is the transposed of the the projector matrix for the probe $\overrightarrow{A}_s$ or pump $\overrightarrow{A}_p$ vector. By exploiting the projector matrix properties (reported in Appendix A), the two equations (1.22) and (1.23) can be written

in the hybrid Jones-Stokes form a

$$VNLSE \quad \frac{\partial \overrightarrow{A}_s(z,t)}{\partial z} = -j\gamma e^{-\alpha z}\frac{2}{3}\left[\frac{3}{2}s_{0s}\sigma_0 + 2s_{0p}\sigma_0 + \overrightarrow{\overrightarrow{s}}_p \cdot \overrightarrow{\sigma} - \frac{1}{2}s_{3s}\sigma_3\right]\overrightarrow{A}_s \tag{1.24}$$

$$Manakov \quad \frac{\partial \overrightarrow{A}_s(z,t)}{\partial z} = -j\gamma e^{-\alpha z}\frac{8}{9}\left[s_{0s}\sigma_0 + \frac{3}{2}s_{0p}\sigma_0 + \frac{1}{2}\overrightarrow{s}_p \cdot \overrightarrow{\sigma}\right]\overrightarrow{A}_s \tag{1.25}$$

where $\overrightarrow{s}_i = [s_{1i}, s_{2i}, s_{3i}]^T$ (for $i = s, p$) is the probe (s) or pump (p) Stokes vector with intensity s_{0i}. Moreover, in (1.24) I resort to the projector matrix property for which the transposed projector is $P_s^T = P_s - s_{3s}\sigma_3$ and $P_s\overrightarrow{A}_s = s_{0s}\overrightarrow{A}_s$ and define $\overrightarrow{\overrightarrow{s}}_p = [s_{1p}, s_{2p}, 0]^T$ the pump Stokes vector with the third component null, hence $\overrightarrow{\overrightarrow{s}}_p$ identifies the linear part of the pump Stokes vector $\overrightarrow{s}_p$.

Equations (1.24) and (1.25), together with the related equations governing the pump propagation, represent a system of nonlinear differential equations (VNLSE or Manakov) that governs the simultaneous propagation, in nonlinear regime, of probe and pump channels within an optical fiber. Concentrating on the probe field $\overrightarrow{A}_s$, its (nonlinear) propagation together with the pump generates three effects, both in the VNLSE and in the Manakov framework. The first effect, proportional to the probe intensity a_0, represents the SPM (hence a scalar phase distortion), as appears in the single channel scenario (see Sec. 1.2.1). The second effect, proportional to the pump intensity p_0, is formally identical to SPM, hence it represents a scalar phase distortion, but dictated by the pump power. In the literature, this term is called *cross phase modulation* (XPM), since the phase distortion depends on the power of the other channel propagating with the probe. The SPM and XPM effects differ, from VNLSE (1.24) to Manakov (1.25), only in the coefficients, hence only in the strength with which they occur. This is no longer true for the last effect, accounting for the vectorial interactions between probe and pump, hence accounting for the nonlinear polarization rotations. In the VNLSE framework (1.24), the NPR affecting the probe, represented by the term $\overrightarrow{\overrightarrow{s}}_p \cdot \overrightarrow{\sigma} - \frac{1}{2}s_{3s}\sigma_3$, depends on both the pump Stokes vector $\overrightarrow{\overrightarrow{s}}_p$ (that acts only through its linear components) and its own ellipticity s_{3s} (as in the single channel scenario, discussed in Sec. 1.2.1). On the other hand, in the Manakov framework (1.25), the NPR affecting the probe, represented by the term $\overrightarrow{s}_p \cdot \overrightarrow{\sigma}$, depends only on the (complete) pump Stokes vector $\overrightarrow{s}_p$. In the literature, the NPR of the probe due to the (nonlinear) interaction with the pump is also known as *cross polarization modulation* (XpolM).

To summarize, the presence of a second channel (the pump) propagating together

with the probe through an optical fiber generates, with respect to the case of single channel propagation, two additional effects on the probe: a (scalar) phase distortion proportional to the pump power (XPM) and a polarization rotation depending on the pump polarization (XpolM). Since lossless polarization attraction arises from the XpolM between the probe and the pump signals, I analyze in detail such a term resorting to the equation of motion for the signals Stokes vectors.

Equation of motion

To understand how the polarizations of probe and pump evolve during their propagation, I translate equations (1.24) and (1.25) in the Stokes domain. I start considering the Manakov equation, which is easier to analyze, before moving to the VNLSE. Starting from equation (1.25) and considering the related propagation equation for the pump, the complete system of equations for probe and pump Stokes vectors results

$$\begin{cases} \frac{\partial \overrightarrow{s}_s(z,t)}{\partial z} = & \frac{8}{9}\gamma \mathrm{e}^{-\alpha z}\left[\overrightarrow{s}_p(z,t)\times\overrightarrow{s}_s(z,t)\right] \\ \frac{\partial \overrightarrow{s}_p(z,t)}{\partial z} = & \frac{8}{9}\gamma \mathrm{e}^{-\alpha z}\left[\overrightarrow{s}_s(z,t)\times\overrightarrow{s}_p(z,t)\right] \end{cases}. \tag{1.26}$$

System (1.26), obtained by exploiting the Jones-Stokes conversion rule reported in Appendix A, can be analytically solved, hence a closed-form solution for vectors $\overrightarrow{s}_s(z,t)$ and $\overrightarrow{s}_p(z,t)$ exists [59].

By taking the sum of the equations in system (1.26), $\frac{\partial \overrightarrow{s}_s(z,t)}{\partial z} + \frac{\partial \overrightarrow{s}_p(z,t)}{\partial z}$, it is obtained

$$\frac{\partial\left(\overrightarrow{s}_s(z,t)+\overrightarrow{s}_p(z,t)\right)}{\partial z} = \frac{8}{9}\gamma \mathrm{e}^{-\alpha z}\left[\overrightarrow{s}_p(z,t)\times\overrightarrow{s}_s(z,t) - \overrightarrow{s}_p(z,t)\times\overrightarrow{s}_s(z,t)\right] = 0, \tag{1.27}$$

where the property $a\times b = -b\times a$ for the cross-product is used. Equality (1.27) means that the vector sum between the probe and pump Stokes vectors, $\overrightarrow{s}_s(z,t)+\overrightarrow{s}_p(z,t)$, remains constant along the fiber, hence $\overrightarrow{s}_s(z,t)+\overrightarrow{s}_p(z,t) = \overrightarrow{s}_s(0,t)+\overrightarrow{s}_p(0,t)$. Thus, it is possible to introduce the constant (in z) *pivot* Stokes vector $\overrightarrow{m}(t) = m_0(t)\hat{m}(t) = \overrightarrow{s}_s(0,t)+\overrightarrow{s}_p(0,t)$, that is an invariant quantity for the system (1.26). The pivot magnitude $m_0 = \sqrt{s_{0s}^2 + s_{0p}^2 + 2s_{0s}s_{0p}\cos\chi_{in}}$ depends on the probe and pump intensity and on the angle χ_{in} between the two input signals Stokes vectors, while the pivot direction $\hat{m}$ depends on the input signals polarizations $\hat{s}_s$ and $\hat{s}_p$ and magnitudes. Since the pivot is constant, system (1.26) implies that both probe and pump Stokes vectors, $\overrightarrow{s}_s(z,t)$ and $\overrightarrow{s}_p(z,t)$, rotate around the pivot direction $\hat{m}$ by an angle $\phi_{NL}(z) = \frac{8}{9}\gamma m_0 L_{eff}(z)$. Hence the closed-form solutions for $\overrightarrow{s}_s(z,t)$ and

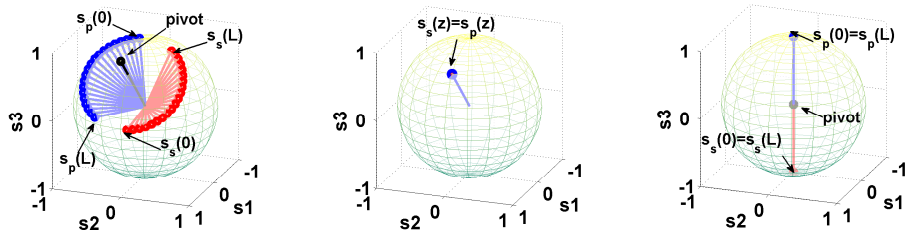

Figure 1.6: Evolution of probe (red) and pump (blue) SOPs, governed by the (Manakov) equations system (1.28), on the Poincaré sphere. (left) Input signals with different polarizations; (center) input signals with same polarization; (right) input signals with orthogonal polarizations. The black vector represents the constant pivot vector.

$\overrightarrow{s}_p(z,t)$ result

$$\begin{cases} \overrightarrow{s}_s(z,t) = e^{\phi_{NL}(z)[\hat{m}\times]}\overrightarrow{s}_s(0,t) \\ \overrightarrow{s}_p(z,t) = e^{\phi_{NL}(z)[\hat{m}\times]}\overrightarrow{s}_p(0,t) \end{cases} \tag{1.28}$$

For system (1.26), there are two cases in which the polarization of both signals does not change. Namely, for probe and pump with the same polarizations $\hat{s}_s = \hat{s}_p$, the cross-product $\overrightarrow{s}_p(z,t) \times \overrightarrow{s}_s(z,t) = \overrightarrow{s}_s(z,t) \times \overrightarrow{s}_p(z,t) = 0$, hence signal SOPs do not change during propagation. On the other hand, for probe and pump with orthogonal polarizations $\hat{s}_s = -\hat{s}_p$, the angle between them is $\chi_{in} = \pi$, hence the pivot magnitude $m_0 = 0$ and signal SOPs do not change during propagation. For all other cases, signal SOPs rotate on the Poincaré sphere, by following a circular trajectory centered on the pivot vector. Fig. 1.6 shows an example of the probe (red) and pump (blue) Stokes vectors evolution, on the Poincaré sphere, for input signals with different polarizations (left), the same polarization (center) and orthogonal polarizations (right). The black vector represents the constant pivot vector, whose length represents its magnitude m_0.

System (1.26) is well known in literature as "*caroussel model*" [60] and its closed-form solution (1.28) is exact when *group velocity dispersion* (GVD) and linear *polarization mode dispersion* (PMD) can safely be neglected in the propagation equations (1.18). Thus, equations (1.28) exactly hold when pump and probe propagate at the same velocities and the mutual position of their SOPs is maintained along the fiber, since pump and probe undergo the same amount of birefringence although they are placed at different wavelengths. While the assumption of negligible PMD is realistic for the modern fibers [61] (characterized by a small PMD coefficient, such as $D_{PMD} = 0.05$ ps/km$^{1/2}$), the assumption of signals propagating at the same speed

is harder (though not impossible) to obtain. Taking into account the different group velocity of each channel, v_s for the probe and v_p for the pump, system (1.26) modifies as follows [34, 45]

$$\begin{cases} \frac{\partial \overrightarrow{s}_s(z,t)}{\partial z} - v_s \frac{\partial \overrightarrow{s}_s(z,t)}{\partial t} = & \frac{8}{9}\gamma e^{-\alpha z}\left[\overrightarrow{s}_p(z,t) \times \overrightarrow{s}_s(z,t)\right] \\ \frac{\partial \overrightarrow{s}_p(z,t)}{\partial z} - v_p \frac{\partial \overrightarrow{s}_p(z,t)}{\partial t} = & \frac{8}{9}\gamma e^{-\alpha z}\left[\overrightarrow{s}_s(z,t) \times \overrightarrow{s}_p(z,t)\right] \end{cases}. \tag{1.29}$$

Since probe and pump propagate at different velocities ($v_s \neq v_p$) within the fiber, the pivot $\overrightarrow{m}$ is no more an invariant quantity for system (1.29), hence it does not remain constant along the fiber, but it moves (on the Poincaré sphere) during signals propagation. Thus, a closed-form solution for the equations of motion in (1.29) does not exists, hence system (1.29) must be solved numerically. In such a case, it is useful to define the *walk-off* parameter, hence a parameter that accounts for the difference between the signals velocities, so that $v_{wo}^{-1} \triangleq v_s^{-1} - v_p^{-1}$ is the inverse of the walk-off parameter. By considering the new time-frame $\tau \triangleq t - z/v_{ref}$, that moves at the reference speed $v_{ref}^{-1} \triangleq \left(v_s^{-1} + v_p^{-1}\right)/2$ (hence, that moves with speed equal to the average between the signals velocities), system (1.29) can be expressed by explicating the walk-off parameter as [34, 45]

$$\begin{cases} \frac{\partial \overrightarrow{s}_s(z,\tau)}{\partial z} + \frac{1}{2v_{wo}} \frac{\partial \overrightarrow{s}_s(z,\tau)}{\partial \tau} = & \frac{8}{9}\gamma e^{-\alpha z}\left[\overrightarrow{s}_p(z,\tau) \times \overrightarrow{s}_s(z,\tau)\right] \\ \frac{\partial \overrightarrow{s}_p(z,\tau)}{\partial z} - \frac{1}{2v_{wo}} \frac{\partial \overrightarrow{s}_p(z,\tau)}{\partial \tau} = & \frac{8}{9}\gamma e^{-\alpha z}\left[\overrightarrow{s}_s(z,\tau) \times \overrightarrow{s}_p(z,\tau)\right] \end{cases}. \tag{1.30}$$

System (1.30) highlights how the evolution of the signals Stokes vectors, hence of the signal SOPs, depends both on the difference between the signals velocities, i.e., on the walk-off v_{wo}, and on the Kerr-induced polarization interactions $\left(\overrightarrow{s}_i \times \overrightarrow{s}_j\right)$. In the following chapter, I will detail the dynamics of the signal SOPs evolution, highlighting when the joint effect of the walk-off and of the Kerr nonlinearity induces the lossless polarization attraction phenomenon. Moreover, note that system (1.30) holds for both co- and counter-propagating signals [38]; in the two cases, system (1.30) differs only for the amount of the walk-off v_{wo}, that becomes relativistic, i.e., in the order of the speed of light, for counter-propagating signals.

Moving on the VNLSE framework, starting from equation (1.24) and considering the related propagation equation for the pump, the complete system of equations for probe and pump Stokes vectors (propagating at the same velocity) results

$$\begin{cases} \frac{\partial \overrightarrow{s}_s(z,t)}{\partial z} = & \frac{2}{3}\gamma e^{-\alpha z}\left[2\overrightarrow{\overrightarrow{s}_p} - s_{3s}\hat{s}_3\right] \times \overrightarrow{s}_s \\ \frac{\partial \overrightarrow{s}_p(z,t)}{\partial z} = & \frac{2}{3}\gamma e^{-\alpha z}\left[2\overrightarrow{\overrightarrow{s}_s} - s_{3p}\hat{s}_3\right] \times \overrightarrow{s}_p \end{cases}. \tag{1.31}$$

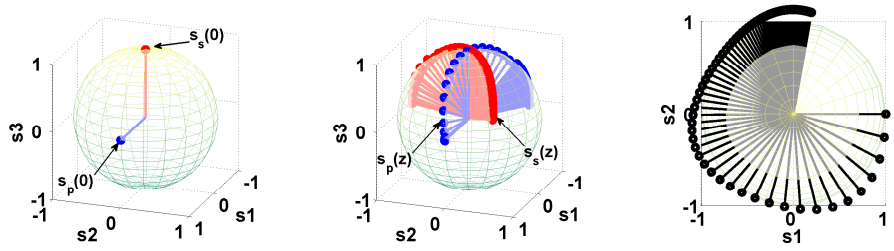

Figure 1.7: Evolution of probe (red) and pump (blue) SOPs, governed by (VNLSE) equations system (1.31), on the Poincaré sphere. (left) Input signal SOPs; (center) signal SOPs evolution along the fiber; (right) pivot vector evolution along the fiber.

It is easy to demonstrate that in the VNLSE framework, the pivot vector $\overrightarrow{m}$ is no longer an invariant quantity even in the case of signals propagating at the same velocity, hence a closed-form solution for system (1.31) does not exist. However, by tacking the sum of equations in (1.31), it is easy to demonstrate that the third component m_3 of the pivot vector $\overrightarrow{m}$ is an invariant quantity for the system. Moreover, it can be demonstrated, by evaluating $\frac{\partial m_0^2}{\partial z}$, that the pivot vector does not preserve its magnitude, except in some particular cases. Thus, in the VNLSE framework, during propagation the pivot rotates around the third Stokes axis $\hat{s}_3$, maintaining its third component m_3 constant but changing its magnitude. In other words, the pivot $\overrightarrow{m}$ moves on a "horizontal" plane (i.e., parallel to the $(\hat{s}_1, \hat{s}_2)$ plane), on the Poincaré sphere. Fig. 1.7 shows an example of the probe (red) and pump (blue) Stokes vectors evolution (center), on the Poincaré sphere, when the input probe is right-circular polarized while the input pump is linear-horizontal polarized (left). The pivot evolution is shown in Fig. 1.7(right).

By considering system (1.31) when the signals propagate at the different velocities, the evolution of the pivot vector, hence of the signals SOPs, complicate evenmore. Anyway, since in my thesis I will always refer to signals propagating within a randomly birefringent fiber (where the Manakov-PMD holds), except in Sec. 2.2.1 of chapter 2, I shall not dedicate more discussion on the VNLSE equation in a two-channel scenario.

Despite the system of motion equations, (1.31) or (1.30), capture all the Kerr-induced polarization effects that produce polarization attraction, in the Stokes domain all the nonlinear scalar effect (SPM and XPM) are not visible. In order to provide exhaustive numerical simulations, the results presented in the following chapter are obtained

by solving the propagation equations in Jones domain, VNLSE or Manakov-PMD, where all scalar effect are included. In particular, signals propagation has been solved by resorting to *Optilux* [62], the open source optical simulator, based on the Split Step Fourier Method (SSFM), developed at the University of Parma.

1.3 How to measure the effectiveness of polarization attraction

In order to measure the performance of a NLP device, I need to evaluate the similarity between the polarization of two optical fields, with time-varying amplitude, phase and polarization. Let the real Stokes vectors $\overrightarrow{s}_p(t) = s_{0p}(t)\hat{s}_p(t)$ and $\overrightarrow{s}_s(t) = s_{0s}(t)\hat{s}_s(t)$ represent the optical fields of pump and signal, respectively, where the scalar quantities $s_{0p}(t)$ and $s_{0s}(t)$ are the instantaneous field intensities, while the unit magnitude Stokes vectors $\hat{s}_p(t)$ and $\hat{s}_s(t)$ represent the instantaneous field SOPs. I have defined, during my Ph.D., the *degree of attraction* (DOA) as the maximum of the normalized cross-correlation between the Stokes vectors of the two interacting signals [42, 46]:

$$\mathrm{DOA} \triangleq \max_{\tau} \left\{ \frac{\left\langle \overrightarrow{s}_p(t+\tau) \cdot \overrightarrow{s}_s(t) \right\rangle}{\langle s_{0p}(t+\tau) s_{0s}(t) \rangle} \right\}, \tag{1.32}$$

where the dot stands for scalar product and the angular brackets denote time-averaging, i.e., $\langle \cdot \rangle = (1/T) \int_T \cdot dt$, extended over the whole signal duration T. Since τ is a time offset between pump and signal, accounting for their mutual delay, I assume in the following, without loss of generality, that the optimal $\tau = 0$. The DOA is a ratio of time-averages, hence T simplifies in (1.32) and $\langle s_0(t) \rangle$ can be seen as the energy of a signal with instantaneous intensity $s_0(t)$ (collected over T). Factoring out the Stokes vectors magnitudes, DOA can be written as

$$\mathrm{DOA} = \left\langle \frac{s_{0p}(t) s_{0s}(t)}{\langle s_{0p}(t) s_{0s}(t) \rangle} \hat{s}_p(t) \cdot \hat{s}_s(t) \right\rangle = \langle w(t) \cos(\varphi(t)) \rangle, \tag{1.33}$$

where I defined $\varphi(t) = \arccos(\hat{s}_p(t) \cdot \hat{s}_s(t))$ as the angle between pump and signal SOPs, while $w(t) = s_{0p}(t) s_{0s}(t) / \langle s_{0p}(t) s_{0s}(t) \rangle$ is a positive and normalized ($\langle w(t) \rangle = 1$) "weight function", representing the time distribution of the joint signal intensities. Thus, the DOA physically represents the time-average of the angle $\varphi(t)$ between the instantaneous signal SOPs, weighted by their joint intensity. By definition, $\mathrm{DOA} \in [-1; +1]$ and the extrema correspond to constantly orthogonal ($\hat{s}_s(t) = -\hat{s}_p(t)$) or

constantly parallel ($\hat{s}_s(t) = \hat{s}_p(t)$) signal SOPs. The latter condition yields DOA $= 1$ and identifies the case of an ideal polarization attraction.

The above definition of DOA, first introduced in [42, 46], stems from classical communication theory. In other works, the effectiveness of polarization attraction is quantified in different ways: the fraction of signal energy co-polarized with the attracting pump is measured in [6], while the DOP is adopted in [34, 45, 47]. All these quantities are closely related to each other, as I show next.

1.3.1 Completely polarized CW pump

Due to the transient behavior of LPA [41], the SOP and intensity of the attracting pump should be stable in time. Indeed, all the literature on LPA assumes a completely polarized CW pump, so that the Stokes vector of the pump is time-independent, $\overrightarrow{s}_p(t) = s_{0p}\hat{s}_p$, and (1.33) consequently simplifies:

$$\mathrm{DOA} = \frac{\left\langle \overrightarrow{s}_s(t) \right\rangle}{\langle s_{0s}(t) \rangle} \cdot \hat{s}_p = \mathrm{DOP_S MSA}. \tag{1.34}$$

In (1.34), I used the standard definition [55] of the time-averaged degree of polarization of the signal (as pointed out by the subscript), $\mathrm{DOP_S} = \left\| \left\langle \overrightarrow{s}_s(t) \right\rangle \right\| / \left\langle \left\| \overrightarrow{s}_s(t) \right\| \right\rangle$ (as defined in (1.10)), and introduced the *mean SOP attraction*

$$\mathrm{MSA} = \frac{\left\langle \overrightarrow{s}_s(t) \right\rangle}{\left\| \left\langle \overrightarrow{s}_s(t) \right\rangle \right\|} \cdot \hat{s}_p = \hat{m}_s \cdot \hat{s}_p = \cos(\chi). \tag{1.35}$$

The MSA has a simple geometrical meaning: since $\left\langle \overrightarrow{s}_s(t) \right\rangle$ is the mean signal Stokes vector, χ is the angular distance between the attracting (constant) pump SOP $\hat{s}_p$ and the mean (power-averaged) signal SOP $\hat{m}_s$. Note that, although I used here the same notation χ as in Sec. 1.1, where $\chi \triangleq \arctan\left(\frac{|A_y|}{|A_x|}\right)$, the two angles are not related to each other. To avoid confusion, I specify that throughout the rest of my thesis, angle χ always refers to the angular distance between $\hat{s}_p$ and $\hat{m}_s$. The factorization in (1.34) is a conceptually remarkable result, since it highlights the trade-off inherent in the LPA process, where an originally completely polarized signal becomes depolarized (i.e., its $\mathrm{DOP_S}$ decreases) as its average SOP $\hat{m}_s$ moves closer to the pump SOP $\hat{s}_p$ [41, 44]. Hence, an effective attraction occurs only if the increase in MSA is larger than the $\mathrm{DOP_S}$ decrease. Supposing that the input signal is completely polarized, i.e., $\overrightarrow{s}_s(t) = s_{0s}(t)\hat{s}_s$, the initial DOA, evaluated before LPA takes place, from (1.34) is $\mathrm{DOA_{in}} = \hat{s}_s \cdot \hat{s}_p = \cos(\chi_{in})$, where χ_{in} is the angle between the input signal and pump SOPs, in Stokes space.

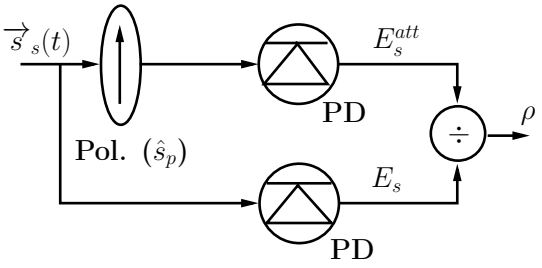

Figure 1.8: Experimental setup to measure the fraction of signal energy attracted towards the pump SOP $\rho = \frac{1}{2}(1 + \mathrm{DOA})$.

Besides its geometrical interpretation, the DOA also has a precise physical meaning. Suppose to filter the signal through an ideal polarizer, aligned with the pump SOP, as shown in Fig. 1.8. The energy output from such a filter E_s^{att} can be expressed, in terms of Stokes vectors, as $E_s^{att} = \frac{1}{2}T\langle s_{0s}(t) + \vec{s}_s(t)\cdot\hat{s}_p\rangle$ (again, T is the averaging period) [55], compared with the input signal energy $E_s = T\langle s_{0s}(t)\rangle$. Hence, from (1.34), the ratio of signal energies $\rho \triangleq E_s^{att}/E_s$ detected after and before filtering is

$$\rho = \frac{1}{2}(1 + \mathrm{DOA}). \tag{1.36}$$

Since the quantity ρ can be measured (it was used in [6] to experimentally quantify the amount of LPA), the **DOA is a geometrically meaningful quantity, that is physically measurable through the simple conceptual setup in Fig.** 1.8**, resorting to a photodiode and an ideal polarizing filter**.

1.3.2 Input signals with random SOP

Referring to a practical application of the NLP, while the pump SOP at the input of the device can be controlled freely, the hypothesis of an input signal with a deterministic SOP is unrealistic, e.g., due to the polarization impairments brought about by the optical link where the signal propagates. Consequently, the SOP of the signal at the NLP input, hence its angular distance χ_{in} from the input pump SOP, and the corresponding DOA value at the NLP output, are random variables. Thus, I consider a random input signal SOP (uniformly distributed on the Poincaré sphere), and evaluate the NLP performance by (statistically) averaging the DOA with respect to the

signal SOP realizations:

$$\overline{\mathrm{DOA}} = E\left[\frac{\left\langle \overrightarrow{s}_s(t)\right\rangle}{\langle s_{0s}(t)\rangle}\cdot\hat{s}_p\right] = \frac{E\left[\left\langle \overrightarrow{s}_s(t)\right\rangle\right]}{\langle s_{0s}(t)\rangle}\cdot\hat{s}_p, \tag{1.37}$$

where $E[\cdot]$ represents statistical-averaging, while $\langle s_{0s}(t)\rangle$ and $\hat{s}_p$ are independent of the input signal SOP.

From (1.37), multiplying and dividing by the quantity $\left\|E\left[\left\langle \overrightarrow{s}_s(t)\right\rangle\right]\right\|$, I obtain

$$\begin{aligned}\overline{\mathrm{DOA}} &= \frac{\left\|E\left[\left\langle \overrightarrow{s}_s(t)\right\rangle\right]\right\|}{\langle s_{0s}(t)\rangle}\frac{E\left[\left\langle \overrightarrow{s}_s(t)\right\rangle\right]}{\left\|E\left[\left\langle \overrightarrow{s}_s(t)\right\rangle\right]\right\|}\cdot\hat{s}_p \\ &= \mathrm{DOP}\cos(\psi)\end{aligned} \tag{1.38}$$

where I recognize the (time- and statistically-averaged) definition of the DOP, as applied to non-ergodic signals $\mathrm{DOP} = \left\|E\left[\left\langle \overrightarrow{s}_s(t)\right\rangle\right]\right\| / \langle s_{0s}(t)\rangle$. In (1.38), ψ quantifies the angular distance between the attracting pump SOP $\hat{s}_p$ and the unit magnitude vector $\frac{E\left[\left\langle \overrightarrow{s}_s(t)\right\rangle\right]}{\left\|E\left[\left\langle \overrightarrow{s}_s(t)\right\rangle\right]\right\|}$, which represents the SOP towards which the signal SOPs are attracted, on average. In other word, while the DOP measures the "spread" of the ensamble-averaged signal SOPs, the $\overline{\mathrm{DOA}}$ measures the alignment between the "center of mass" of the ensamble-averaged signal SOPs and the pump SOP $\hat{s}_p$. When the angle $\psi = 0$, hence when the signal SOPs are attracted, on average, towards the input pump SOP $\hat{s}_p$, equation (1.38) yields $\overline{\mathrm{DOA}} = \mathrm{DOP}$, otherwise it is always $\overline{\mathrm{DOA}} \leq \mathrm{DOP}$. In particular, in chapter 3 I show that $\overline{\mathrm{DOA}}$ and DOP coincide when LPA occurs within a fiber with a small PMD coefficient, such as, e.g., $\mathrm{D_{PMD}} = 0.05$ ps/km$^{1/2}$ (a value typical of modern fibers) [45]. In this case, it is thus $\overline{\mathrm{DOA}} \in [0;1]$, although negative values are allowed for the unaveraged $\mathrm{DOA} \in [-1;+1]$. The subtle difference between $\overline{\mathrm{DOA}}$ and DOP and its relation to the fiber birefringence shall be further discussed in the context of polarization attraction within fibers with PMD, providing results both in cases where $\overline{\mathrm{DOA}} = \mathrm{DOP}$ (small PMD) and in case where the two quantities differ (large PMD).

Chapter 2

Counter-propagating Nonlinear Lossless Polarizer

In this chapter, I summarize numerical results regarding a counter-propagating nonlinear lossless polarizer. To solve numerically the counter-propagation of optical signals, I introduce a fast and simple iterative algorithm, named SCAOS (simple counter-propagation algorithm for optical signals), based on the split-step Fourier method, that has been conceived during my Ph.D. Resorting to the SCAOS algorithm, I characterize the performance of a counter-propagating NLP, thus providing the design guidelines to realize such a device.

2.1 Simulating counter-propagating signals

2.1.1 The general problem

Simulating lossless polarization attraction (LPA) requires the joint integration of the two vectorial nonlinear propagation equations (VNLSE, vectorial nonlinear Schroedinger equations, or simplified Manakov-PMD equations) of the pump and probe fields. Since in a counter-propagating nonlinear lossless polarizer (NLP) the fields' initial values are supplied at opposite fiber ends, the problem at hand is a Boundary Value Problem (BVP) [63].

In the literature, many numerical methods exist to solve BVPs, as, for example, the relaxation method, the shooting method, the finite difference integration method and many others. All of these methods approximate the exact solution of partial differential equations, whose boundary values are given, iterating a finite difference in-

tegration, applied to a grid of space/time points. As I will show below, applying these methods to the study of LPA requires large amounts of memory and long computation times. In fact, they have been used only to study LPA occurring within a short fiber (2 m) (i.e., with a small number of space points) [6], or with continuous wave signals (i.e., with a small number of time points) [38].

In my specific case, I wanted to study the performance of a NLP acting on modulated signals, hence on time-varying signals, counter-propagating in kilometers long fibers. Thus, in numerical simulations (where signals are time-descrete), I have to deal with vectors of spatially-varying functions, either time-vectors or frequency-vectors. Using the Fast Fourier Transform (FFT) representation of signals, at each coordinate of the space grid there are K values for the two fields (probe and pump), corresponding to the K frequency components. Moreover, the frequency components of the fields are complex, further doubling the number of free variables. Hence, from a practical standpoint, there are typically thousands of variables, i.e., field components (e.g., 16384, 32768, 65536 etc., considering power of 2). Thus, as stated, traditional finite difference integration would require large amounts of memory and long computation times, and it is therefore not suitable for my purpose.

For these reason, I tried alternative methods to simulate counter-propagating optical signals, even within kilometers long fibers. With the availability of the *Optilux* tool [62] to simulate co-propagating signals, I choose to exploit its full potential even in the counter-propagating case. As stated in chapter 1, Optilux solves signal propagation by using the SSFM, which is however designed for signals that travel in the same direction, hence it cannot be used to solve BVPs. To overcome this limitation, I developed an home-made iterative algorithm, named SCAOS (Simple Counter-propagation Algorithm for Optical Signals), which, embedded in Optilux, allows to solve the counter-propagation of optical signals, by exploiting the efficiency of the SSFM. Being a SSFM-based algorithm, SCAOS is suitable for simulating counter-propagation of modulated signals even in (kms) long fibers, with limited time/memory requirements. Moreover, as I will show in the following sections, SCAOS allows to monitor propagating fields at any fiber coordinate, helping to study the dynamics of LPA. Finally, although I implement SCAOS within Optilux, the proposed algorithm can be implemented within any traditional optical simulator, based on the SSFM.

2.1.2 The SCAOS algorithm

I wish to simulate the counter-propagation of a probe $\mathbf{e}^+(z,t)$ and a pump $\mathbf{e}^-(z,t)$ signal, traveling within a fiber of length L, whose initial values $\mathbf{e}^+(0,t)$ and $\mathbf{e}^-(L,t)$ are

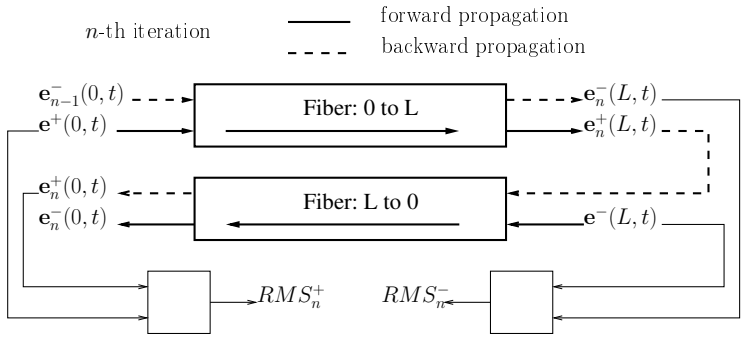

Figure 2.1: Schematic description of the iterative SCAOS algorithm.

given. Signal superscripts $\pm$ identify the propagation direction, so that $\mathbf{e}^+(t)$ propagates from $z = 0$ to $z = L$, and vice-versa for $\mathbf{e}^-(t)$. Hence, the final result is to calculate the outcoming probe $\mathbf{e}^+(L,t)$ and pump $\mathbf{e}^-(0,t)$.

The basic idea behind the proposed algorithm is to let $\mathbf{e}^+$ and $\mathbf{e}^-$ iteratively propagate from $z = 0$ to $z = L$ and vice-versa (i.e., in the "reverse fiber", as seen from $z = L$ to $z = 0$). In each propagation, one of the fields forward-propagates, starting from its (true) initial value, towards its output fiber end, while the other backward-propagates, i.e., travels according to an inverse-Schroedinger equation, starting from its (estimated) output value, towards its input fiber end. Backward-propagation is an option that can be easily implemented in the SSFM; I did so, while implementing the whole SCAOS algorithm, within Optilux [62].

Fig. 2.1 sketches the $n-th$ algorithmic iteration, which consists of two fiber propagations. In the first propagation, from 0 to L, the true input probe $\mathbf{e}^+(0,t)$ forward-propagates (solid arrow, in Fig. 2.1), together with the $(n-1)-th$ estimate of the output pump $\mathbf{e}^-_{n-1}(0,t)$, which backward-propagates (dashed arrow, in Fig. 2.1). In the second propagation, from L to 0, the true input pump $\mathbf{e}^-(L,t)$ forward-propagates, together with the $n-th$ estimate of the output probe $\mathbf{e}^+_n(L,t)$, which backward-propagates.

To allow the algorithm to start, before the first iteration the initial pump estimate $\mathbf{e}^-_0(0,t)$ is found, by letting the pump initial condition $\mathbf{e}^-(L,t)$ forward-propagate (from L to 0) as a single field, i.e., without suffering any cross-channel impairment by the probe field $\mathbf{e}^+$. It should be noted that the choice to start the algorithm by getting the initial pump estimate $\mathbf{e}^-_0(0,t)$ was arbitrary. In fact, SCAOS algorithm could also be implemented by finding the initial probe estimate $\mathbf{e}^+_0(L,t)$ first, provided one reverses the order of the two propagations in the algorithmic iteration, i.e., by

implementing first the propagation from L to 0, and then the propagation from 0 to L. I chose to initialize SCAOS by finding $\mathbf{e}_0^-(0,t)$ in order to let the algorithmic iterations start with the propagation from 0 to L.

After each half-iteration, the backward-propagating signal completes a round-trip towards its input fiber end, yielding a new $n-th$ estimate for the input field ($\mathbf{e}_n^-(L,t)$, at $z=L$, or $\mathbf{e}_n^+(0,t)$, at $z=0$). A normalized root mean square (rms) error is calculated, between such an estimate and its true initial value, as

$$RMS_n^{\pm}(z) = \sqrt{\frac{\int \left\|\mathbf{e}_n^{\pm}(z,t) - \mathbf{e}^{\pm}(z,t)\right\|^2 dt}{\int \left\|\mathbf{e}^{\pm}(z,t)\right\|^2 dt}}, \tag{2.1}$$

where $RMS_n^+(z)$ is evaluated at $z=0$, while $RMS_n^-(z)$ is evaluated at $z=L$. At the same time, the given initial (boundary) value is substituted to the estimate ($\mathbf{e}^+(0,t)$ replaces $\mathbf{e}_n^+(0,t)$ or $\mathbf{e}^-(L,t)$ replaces $\mathbf{e}_n^-(L,t)$), so that the outcoming forward-propagating field ($\mathbf{e}_{n+1}^+(L,t)$ or $\mathbf{e}_{n+1}^-(0,t)$, which are the sought quantities) is refined, at the next iteration.

In the trivial case that only (linear and nonlinear) single-channel impairments affect the propagation, the input field ($\mathbf{e}^+(0,t)$ or $\mathbf{e}^-(L,t)$) can be exactly reconstructed, starting from its estimated output value ($\mathbf{e}_n^+(L,t)$ or $\mathbf{e}_n^-(0,t)$), generating a null error ($RMS_n^{\pm}=0$), at every iteration. This is no longer true in the presence of cross-channel interactions (XPM and XpolM) between fields, since the estimated input value ($\mathbf{e}_n^+(0,t)$ or $\mathbf{e}_n^-(L,t)$) depends not only on the corresponding estimated output field ($\mathbf{e}_n^+(L,t)$ or $\mathbf{e}_n^-(0,t)$), but also on its interaction with the other channel within the fiber, thus generating a non-zero rms error.

The rms errors $RMS_n^{\pm}$, evaluated for the pump and probe at $n-th$ iteration, drive the stop criterion: the algorithm stops when both $RMS_n^{\pm}$ are below a certain threshold, meaning that the round-trip field estimates are sufficiently close to their true initial values ($\mathbf{e}_n^+(0,t) \cong \mathbf{e}^+(0,t)$ and $\mathbf{e}_n^-(L,t) \cong \mathbf{e}^-(L,t)$). As a result, also the estimated output probe $\mathbf{e}_n^+(L,t)$ and pump $\mathbf{e}_n^-(0,t)$ fields could be considered sufficiently close to their true values $\mathbf{e}^+(L,t)$ and $\mathbf{e}^-(0,t)$ (which represents our goal).

In applying the SCAOS algorithm, as described above, to the study of LPA, I found that, when the fiber is long (kilometers) and/or the signals undergo strong nonlinear distortions, the convergence of the algorithm can be hard, sometimes impossible, to reach. To overcome this problem, I enriched the algorithm with a "store/recall" technique. In particular, I introduced N (equidistant) *checkpoints* along the fiber, marked by coordinates z_i (with $i=1,...,N$ and $0<z_i<L$), in correspondence of which, at each propagation, the forward-propagating field is stored. At the same

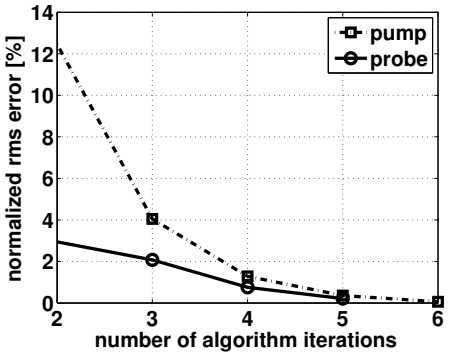

Figure 2.2: Residual normalized rms error during SCAOS iterations.

time, the backward-propagating field is replaced by its own replica, that was stored at the corresponding checkpoint z_i during the previous propagation, when it was the forward-propagating field. In other words, the stored fields provide a snapshot of the signal along the fiber, at z_i, thus representing a sort of "state variable" for the algorithm.

Fig. 2.2 shows a typical behavior of the normalized rms errors $RMS_n^{\pm}$ generated by SCAOS algorithm, where the errors become negligible (below 0.1 %) in a few iterations. Despite rms error in Fig. 2.2 refers to the polarization attraction setup and parameter values of Sec. 2.2.1, the trend of $RMS_n^{\pm}$ is representative of all polarization attraction setups analyzed in this chapter.

Of course, the store/recall technique introduced here represents an heuristic choice. The rationale behind the implemented strategy is that the field stored at z_i during its forward-propagation is guessed to be more accurate than the backward-propagating field at the same z_i, being the first evaluated from its true initial value. Furthermore, by evaluating rms errors $RMS_n^{\pm}(z)$ at the checkpoints z_i, the store/recall strategy allows to monitor pump and probe field profiles not only at the corresponding fiber output (i.e., at $z = 0$ or $z = L$), but also at each position z_i along the fiber, ensuring that the whole evolution of the fields along the fiber has reached a steady configuration. Clearly, the choice of N depends on the fiber parameters (primarily, nonlinear coefficient and length) and on the signals power, which together determine the strength of the nonlinear interaction. No a-priori rule is given here to determine the N value, that was empirically chosen for each tested configuration of the NLP device. Anyway, it is clear that the choice of N is dictated by a compromise between the accuracy of the results (increasing with N) and the amount of memory/time demanded by the

numerical simulation (still increasing with N). To my experience, a maximum of a few tens of checkpoints were sufficient to obtain accurate results within a reasonable time-frame, even for the most unfavorable NLP configurations (e.g., for fiber length in the order of kilometers and signals power in the order of few watts).

As a further consideration, I discuss briefly on the possibility to enhance the algorithm by gradually increasing the nonlinear fiber coefficient γ. To this aim, it would be necessary to build an outer loop, where the nonlinear coefficient starts from a small value γ_0 and, after the iterative convergence of pump and probe fields, its value increases, to reach the final true γ value of the fiber under test, in a few steps. The rationale behind this approach is that, in the limit of $\gamma \to 0$, one iteration is sufficient to ensure convergence of the solutions, since the signals would not affect each other during the propagation, as already noted above. I tested the enhancement just described, finding that the increase in accuracy it yields is not appreciable, compared with the increase in computation time. In other words, I observed a quick convergence when employing directly the true γ value of the fiber, even for strongly nonlinear fibers. Hence, in the results that follow, I did not implement the outer loop to increase γ, whose computational cost would be linear in the number of $\gamma-$ steps.

I tested the SCAOS algorithm with many system configurations (not necessarily related to the NLP) so as to verify its robustness. In my thesis, I report only the tests performed by applying SCAOS to replicate numerical and experimental results presented in [6] and [2], where the first demonstration of LPA has been provided, occurring either within a short isotropic fiber or within a long standard telecom fiber, respectively.

2.1.3 Pattern length in simulations

In this section, I address the problem of properly selecting the length of the signal patterns, i.e., the number of symbols to be transmitted, in numerical simulation of counter-propagating signals. In particular, I show that the pattern length must be matched to the fiber length, to avoid numerical artifacts affecting simulation results.

The problem under consideration is related to the use of the SSFM to handle the (nonlinear) propagation of signals, where signals are represented by their FFT samples; this approach implicitly assumes periodic boundary conditions, due to the circular property of the FFT. Thus, the pattern length dimensioning problem is not due to counter-propagation itself, but it occurs whenever signals propagation is solved through the SSFM, hence also in the co-propagating case.

With co-propagating signals, the minimum number of symbols to be transmitted is simply related to the overall walk-off accumulated along the optical fiber by

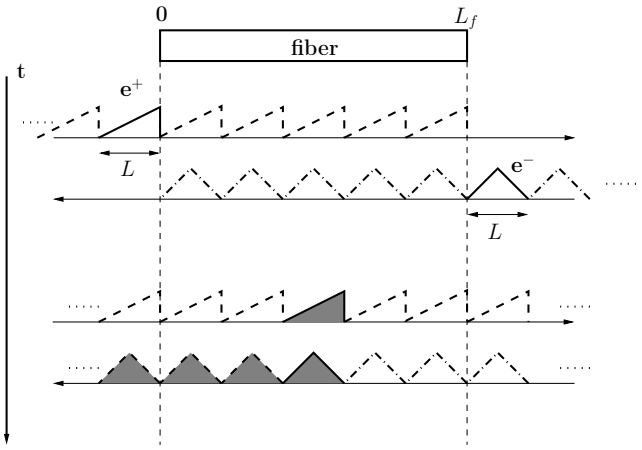

Figure 2.3: The use of FFT for representing signals (triangles with solid line) involves periodic repetitions (triangles with dashed line).

the interacting signals, normalized to the symbol period. When the pattern length is greater than the overall walk-off, it is guaranteed that each symbol of each signal interacts with any other symbols of the other signal only once along the fiber, as actually happens in reality. Otherwise, it may happen that a symbol interferes with the same symbol of the other signal repeatedly (due to the circularity of the FFT), hence an artificial correlation is introduced in the nonlinear signals interaction, that corrupts results.

With counter-propagating signals, since the interacting fields travel one towards the other, the pattern length dimensioning problem becomes critical. Below, I explain why it is so critical and expose the rule for properly setting the pattern length. The counter-propagating probe $\mathbf{e}^+(z,t)$ and pump $\mathbf{e}^-(z,t)$ signals travel in opposite direction at equal group velocity $v_g = c/n$, where $n = 1.5$ is the fiber refractive index and c is the speed of light in vacuum. Without loss of generality, I assume, for the moment, that probe and pump signals have the same limited duration T, so that the space occupied by both signals inside the fiber results $L = v_g T$. Due to the circularity of the FFT, it is as if the fields $\mathbf{e}^{\pm}(z,t+nT) = \mathbf{e}^{\pm}(z,t)$ are periodically repeated outside their duration interval $[0;T]$, hence, if the fiber length $L_f > L$, many signal replicas are present simultaneously within the fiber, as shown in Fig. 2.3. Here, the triangles with solid line represent the (real) input probe and pump fields, while triangles with dashed line represent the replicas generated by the FFT.

Focusing only on the real signals (solid triangles), in a real experiment they would

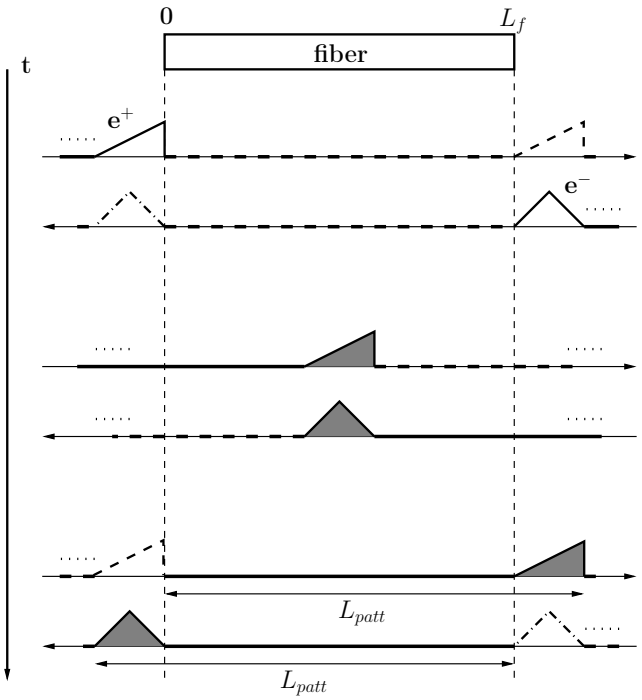

Figure 2.4: Signals duration with zero-padding, to avoid numerical artifacts.

interact at the middle of the fiber, and then move on towards their respective fiber ends. Given the frame of Fig. 2.3, this is no longer true in numerical simulation, where the real probe interacts not only with the real pump, but also with its replicas, highlighted by shading, in Fig. 2.3. The same happens to the real pump, that interacts with the probe replicas; hence, instead of interacting only once, signals nonlinearly interact more times, generating numerical artifacts. Thus, it is clear, from Fig. 2.3, that in order to avoid this problem, both probe and pump signals have to be extended with a zero-padding technique, so that there is only one replica at a time within the fiber for each signal, as shown in Fig. 2.4. Hence, a null portion of signal with length equal to L_f is added to both signals, so that a total pattern length $L_{patt} \geq L + L_f$ is enough to ensure that no numerical artifacts result. In fact, for signals longer than L_{patt}, the shaded probe (pump) exits the fiber before the next pump (probe) replica enters in it. Note that, if probe and pump have different lengths, L_s and L_p, respectively, the pattern length has to be chosen based on the longer signal, hence $L_{patt} \geq \max(L_s, L_p) + L_f$.

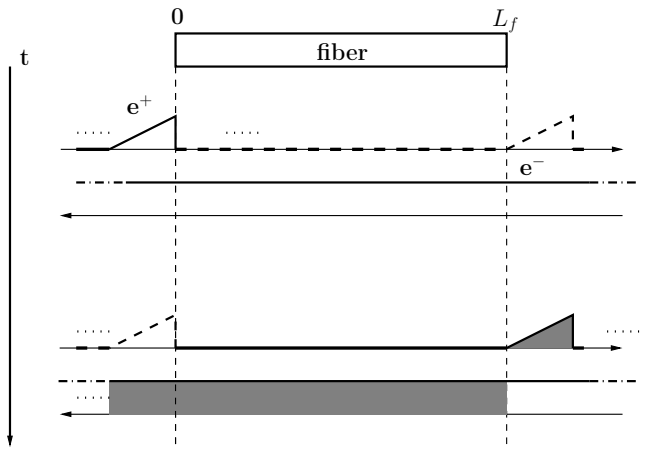

Figure 2.5: Signals duration, in the case of CW pump.

Since the pump signal is usually CW in LPA, I address now the problem of dimensioning the pattern length when the probe, with limited duration T, interacts with a CW pump. In this case, I cannot use the zero-padding on the pump, since it is assumed always on, hence it continuously fills the fiber, as shown in Fig. 2.5. This issue must be considered, when dimensioning the zero-padding on the probe, in order to let all the distorted pump (i.e., the pump portion that has already interacted with the probe) exit the fiber, before the next probe replica enters in it. I assume, for the moment, that the probe signal is extended through a zero-padding with length L_f, as above, so that only one probe replica is in the fiber at a time. In this case, when the second replica of the probe arrives at the fiber input, there is still a distorted pump portion into the fiber (highlighted by shading in Fig. 2.5), hence the zero-padding must be further increased. Since the distorted pump portion has length L_f, the probe needs a further zero-padding portion with length L_f, so that the total pattern length becomes $L_{patt} \geq L + 2L_f$. **In other words, in the case of a CW pump, the probe needs a zero-padding portion, with length L_f, to start simulation with an empty fiber, and a supplementary zero-padding portion, with length L_f, to let the distorted pump portion exit the fiber.**

Having determined the minimum pattern length L_{patt} that guarantees the correctness of the numerical results, the corresponding minimum pattern duration to be used in simulation is $T_{patt} = L_{patt}/v_g$. This condition could be prohibitively strict, in practical problems, unless the fiber to simulate is very short. For instance, considering LPA between a probe, with duration T, and a CW pump, occurring in a fiber with length

$L_f = 10$ km, the zero-padding duration needed is $2L_f/v_g = 2 \cdot 10^4[\text{m}]/2 \cdot 10^8[\frac{\text{m}}{\text{s}}] = 10^{-4}[\text{s}]$ (or half, if also the pump has limited duration); thus, if the probe is modulated at a typical bitrate $R = 10$ Gb/s, i.e., the bit period is 100 ps, the zero-padding needs 10^6 bit periods. Since typical bit-packets are made of a number of bits in the order of 10^4, the complete zero-padded pattern should be composed of almost 10^{10} bit periods. While the (pseudo-random) bit sequences transmitted by laboratory instruments can be as long as $2^{31} \simeq 10^9$, transmitting a packet of millions of bits in simulations is not feasible. Since each optical pulse is represented by several (e.g., 16, 32, 64) samples, to account for the bandwidth expansion due to nonlinear distortions, hence SSFM would require performing FFT on sample vectors with billions of elements.

To overcome this problem, in simulation results that follow, I replaced the whole bit-packet with a single pulse, with the same duration and average power as the bit-packet, so that the number of samples to be transmitted becomes of the order of few hundreds. Moreover, in Sec. 2.3.7, I demonstrate the equivalence between results obtained with the single pulse and those obtained with a modulated bit-packet.

2.2 SCAOS application to polarization attraction

In this section, I apply the SCAOS algorithm, that has just been described, first to replicate results published in [6], where both numerical and experimental proofs of polarization attraction occurring within a short isotropic fiber were given. The matching between my results and the results in [6] demonstrate the effectiveness of the proposed algorithm. Furthermore, I also apply SCAOS to simulate polarization attraction occurring within a (kilometers) long randomly birefringent fiber, usually hard to study numerically. Finally, I highlight the differences between the dynamics of polarization attraction occurring within a short isotropic or a long birefringent fiber, showing that, for practical purposes, only long fibers are suitable to realize a lossless polarizer device.

2.2.1 LPA within a short isotropic fiber

As a first application of the SCAOS algorithm, I simulate the system setup described in [6] and used for the first experimental demonstration of LPA occurring between signals propagating at telecom wavelengths. The counter-propagating pump and probe beams, both consisting of a completely polarized 10 ns intensity-modulated light pulse, are transmitted on a highly nonlinear single mode fiber, with length $L = 2$ m. Despite the short fiber length, the large Kerr coefficient ($\gamma = 22$ W^{-1}Km^{-1}) and

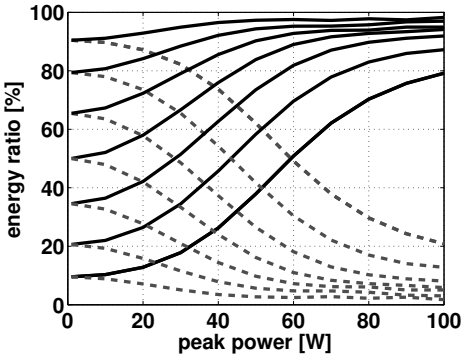

Figure 2.6: Fraction of probe energy that is attracted towards (solid line) a right-circular pump SOP, in a short lossless attractor. The residual fraction of probe energy, i.e., the energy of the probe component that is orthogonal to the attracting pump SOP, is plotted with dashed lines. The 7 plots correspond to probe SOPs with increasing ellipticity (the azimuth is random).

pulse intensities (up to 45 W) used in the experiments allowed a significant nonlinear interaction. Since the typical residual birefringence in such a short fiber is negligible, it can be considered isotropic, hence PMD/birefringence can be neglected in the simulation. Thus, the propagation is governed by the VNLSE (1.11), where circular polarizations play a special role, as shown in chapter 1. Hence, a right circular polarization is chosen for the input pump SOP ($\hat{s}_3$, in Stokes space).

After simulating the propagation of 7 different input probe SOPs with increasing ellipticity and random azimuth, Fig. 2.6 shows the fraction of output probe energy (ρ, as defined in equation (1.36), in chapter 1) that is aligned with (solid line) or orthogonal to (dashed line) the input pump SOP, as a function of the equal pump and probe peak powers injected into the fiber. Results coincide exactly with those reported in [6] (obtained with finite difference integration), demonstrating the effectiveness of the SCAOS algorithm. Moreover, Fig. 2.6 shows how, as power increases, each input probe SOP is attracted towards the right circular polarization imposed by the pump, with the percentage of attraction depending only on the probe ellipticity, i.e., on the angular distance χ_{in} between the input pump and probe Stokes vectors. In fact, the 7 curves are ordered, bottom to top, according to the increasing probe ellipticity, while changing the random azimuth (which is different for each curve) does not change results, as verified numerically.

To gain further insight into the polarization attraction process, Fig. 2.7 reports

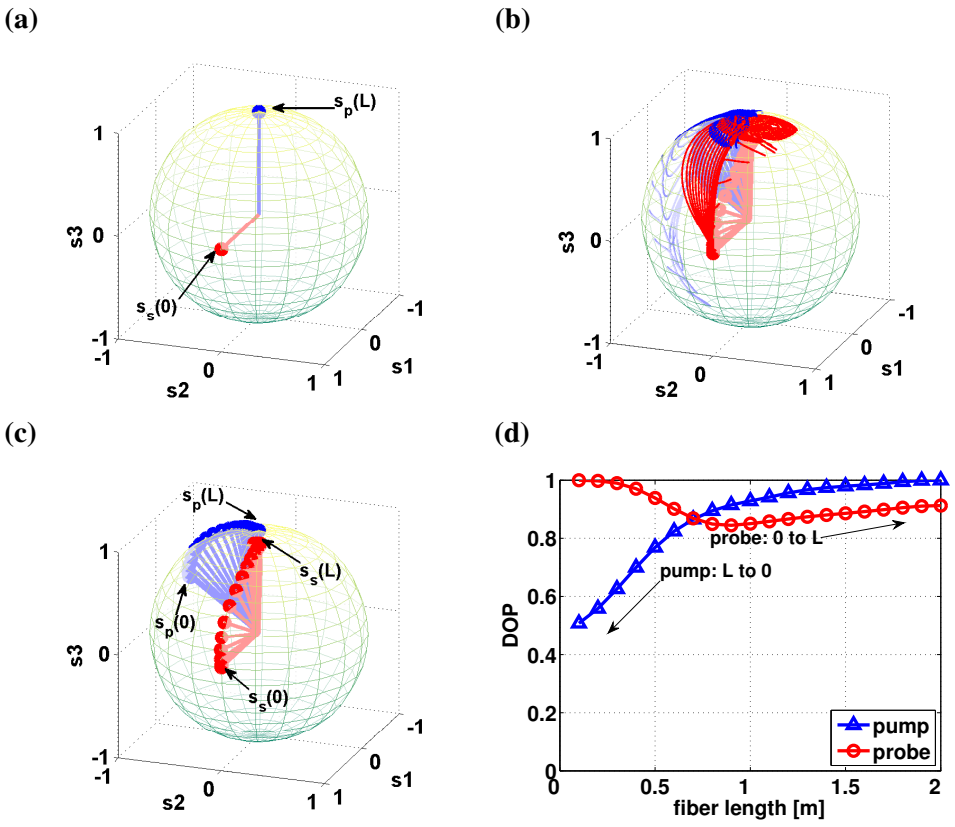

Figure 2.7: Lossless polarization attraction (LPA) between pulses in a short (2 m) highly nonlinear fiber: (a) input signals SOPs ($\chi_{in} = 90°$) (red: probe, blue: pump); (b) SOP traces along z; (c) motion of the average attracted SOP; (d) resulting DOP, along z.

details about the polarization states of the pump and probe along the fiber. Here, the input probe has linear horizontal SOP ($\hat{s}_1$), so that the angular distance $\chi_{in} = 90°$, as reported in Fig. 2.7(a). The degree of polarization (DOP) of the launched pump and probe pulses has unit value, hence each time sample is represented by the same point on the Poincaré sphere (Fig. 2.7(a)). This is no longer true when the two signal beams start interacting: Fig. 2.7(b) shows the depolarization traces, for the probe (red) and pump (blue), on the Poincaré sphere. Each trace represents the time evolution of the pulse's SOP, at a given position $z \in [0, L]$ along the fiber; the Stokes vector of each time sample is normalized to its power, so that the depolarization traces lie on the Poincarè sphere. The inner vectors in Fig. 2.7(b) represent the power-averaged SOP of each depolarization trace, whose direction thus represents $\hat{m}_s$, while the magnitude represents the DOP of that trace (i.e., $\mathrm{DOP_S}$). For the sake of clarity, Figs. 2.7(c,d) report the trajectory followed by the average signal SOPs and the signals DOP evolution along the fiber, respectively. To stress polarization attraction, in Fig. 2.7 pump and probe input powers were fixed to 100 W, hence we operate in the right edge of Fig. 2.6. The probe average SOP (red) is attracted towards the input pump SOP ($\hat{s}_3$), with a relatively small depolarization, so that its degree of attraction is $\mathrm{DOA} = 0.88$. On the contrary, the pump (blue) is much more depolarized and ends away from the input probe ($\hat{s}_1$), so that its DOA towards the input probe is $\mathrm{DOA} = -0.01$. Full results, as in Fig. 2.7(a-d), are obtained with the SCAOS algorithm in 8 min. computation time, on an ordinary PC.

In order to give a more general picture, Fig. 2.8 shows results similar to those reported in Fig. 2.7, in the case of an elliptically polarized input probe SOP, which is closer to (2.8(a,b)) or more distant from (2.8(c,d)) the input pump SOP. Despite the DOP swing results smaller (larger), compared with that reported in Fig. 2.7(d), for closer (further) probe SOP, Fig. 2.8 confirms that the probe SOP is always attracted (on average) towards the input pump SOP, while the pump SOP is never attracted towards the input probe SOP. Moreover, a noteworthy result common to all tested input probe SOPs, is that the probe DOP, after an initial fiber section in which it decreases, starts to increase again, meaning that the probe starts to repolarize around the input pump SOP. More details about such a dynamic will be explained in Sec. 2.3. Note that the trajectories followed by the average probe SOP along the fiber were reported also in [6], obtained by employing finite difference integration. However, by exploiting SCAOS, I am able to provide additional information about the signals DOP along the fiber (such an information lacks in [6]).

Summarizing, different choices for the input probe SOP yield similar results: Fig. 2.9(b) shows the resulting average output probe SOPs (marked by red vectors), when

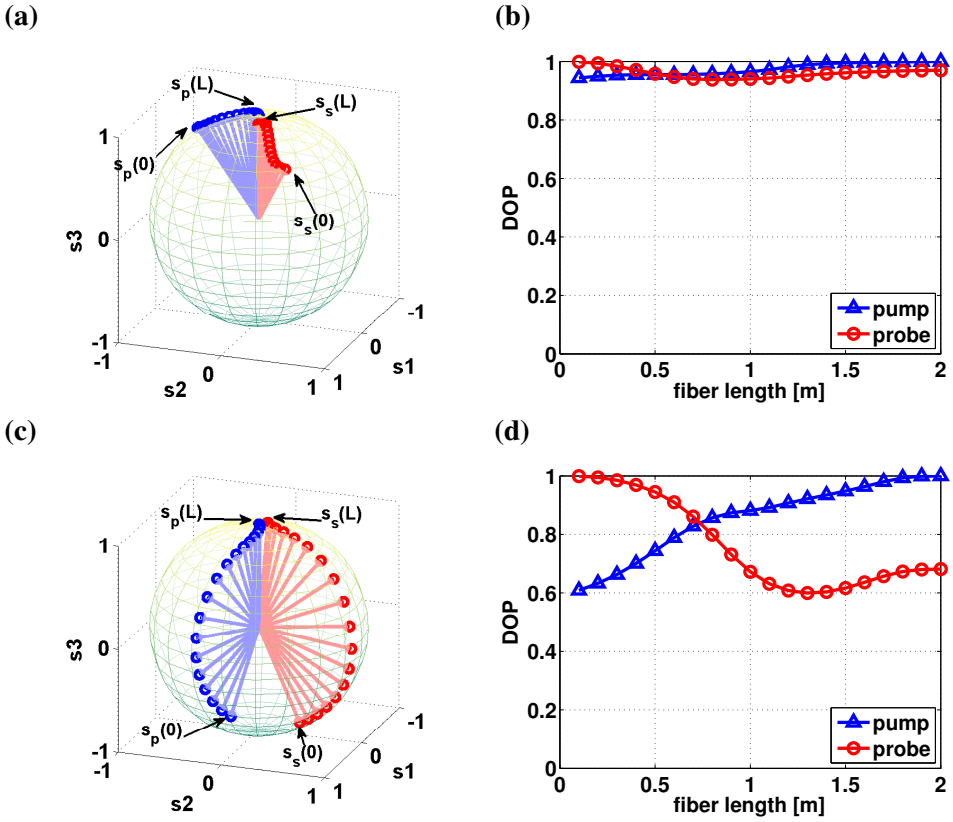

Figure 2.8: Lossless polarization attraction (LPA) between pulses in a short (2 m) highly nonlinear fiber: motion of the average attracted SOP (left) and resulting DOP, along z, (right), for input signal SOPs with $\chi_{in} = 30°$ (top) or $\chi_{in} = 150°$ (bottom).

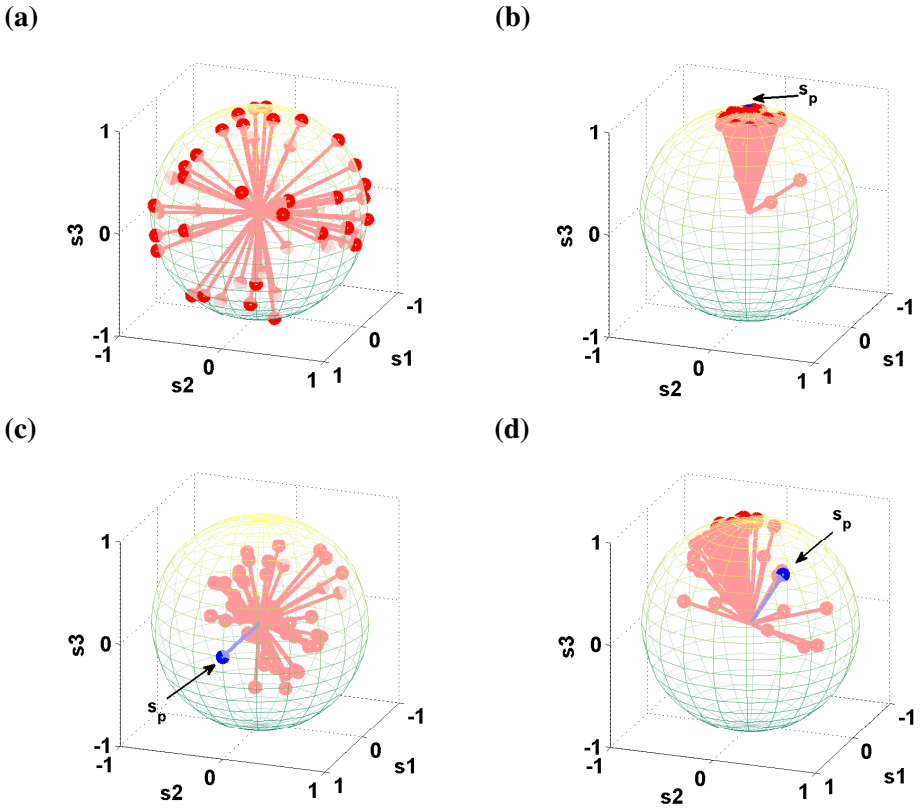

Figure 2.9: Average probe SOPs (red), at the output of a short (2 m) lossless polarization attractor (DOP=magnitude). Plots obtained for 50 random input SOPs (a), in the case of a circular (b), linear (c), and elliptical (d) pump SOP (blue).

the attracting pump SOP (marked by a blue vector) is right circular ($\hat{s}_3$). Results were obtained by launching 50 random input probe SOPs (Fig. 2.9(a)), with uniform distribution over the Poincaré sphere. As usual, polarization attraction entails a certain amount of depolarization: the DOP_S of the resulting output pulses is represented by the (red) vectors' magnitude. Fig. 2.9(b) shows an effective polarization attraction towards the right-circular pump SOP. I verified that the worst performance occurs for those probe SOPs that were initially almost orthogonal to the pump: as demonstrated above, those are the input SOPs that are less attracted, on average, and whose output DOP_S is the lowest (see Fig. 2.8(d)). On the contrary, polarization attraction is not equally effective, in this setup, if the pump is not circularly polarized, as can be verified in Fig. 2.9(c,d), obtained for a linear horizontal (c) or elliptically polarized (d) input pump SOP. The time- and ensamble-averaged DOP (see chapter 1), corresponding to the circularly, linearly and elliptically polarized input pump SOPs, are 0.81, 0.25 and 0.60, respectively. These values quantify the dispersion of the average output probe SOPs that is visible in Fig. 2.9(b-d). The result obtained for a left-circular pump ($-\hat{s}_3$), not reported in figures, was the same as that for the right-circular pump case in Fig. 2.9(b). Hence, an effective polarization attraction occurs only in the case of a circularly polarized pump, while in the tested linear and elliptical pump cases (c-d) the attraction is much weaker.

As a further comment on the results in Fig. 2.9(c-d), the detailed studies in [36,37, 40] pointed out that, in fibers where the VNLSE holds, polarization attraction occurs towards a SOP that has the same ellipticity as the pump but an azimuth rotated by 180°, with respect to the pump[1]. In [36, 37, 40], attraction is studied as an asymptotic condition, for CW signals and in the limit of an infinitely long fiber. However, our results evidence that, for a fiber with finite length, as the one that I employed in the tested setup, the attraction condition is approached to a different extent, depending on the pump SOP, and is way more effective when a circularly polarized pump is injected. Moreover, with a circularly polarized pump (Fig. 2.9(b)) the DOP coincides with $\overline{\text{DOA}}$ (see equation (1.38) in chapter 1), while this coincidence does not hold in the cases of any other pump SOP (2.9(c,d)), since the "attracting" SOP differs from the input pump SOP, hence $\text{DOP} > \overline{\text{DOA}}$.

[1] Of course, the azimuth is undetermined when the pump SOP is circular ($\hat{s}_3$), hence the circular pump case appears to follow the same "rule".

2.2.2 LPA within a long randomly birefringent fiber

As demonstrated in [2], polarization attraction can happen even at moderate power levels, provided that the nonlinear polarization interaction occurs in a long randomly birefringent fiber. However, the authors in [2] only performed experiments, since the numerical simulation of LPA occurring within a kilometers long fiber is computationally too expensive, as stated in Sec. 2.1. Applying the SCAOS algorithm, I have simulated LPA occurring within a long fiber, obtaining results in a reasonable time. Moreover, I show here how dynamics of polarization attraction change, when it occurs within a randomly birefringent fiber, compared with LPA occurring within an isotropic fiber (Sec. 2.2.1).

Thus, I apply the SCAOS algorithm to a system setup similar to the one used for the experiments in [2]. An intensity-modulated probe signal, with peak power 1.2 W, undergoes Kerr interaction with a counter-propagating fully-polarized CW pump, with the same power as the probe, on an ordinary telecom fiber. Such a fiber, with attenuation $\alpha = 0.2$ dB/Km and Kerr coefficient $\gamma = 1.99$ W^{-1}Km^{-1}, is $L =$ 10 km long. In [2], authors transmitted a 10 Gb/s $-$ OOK probe, with a bit pattern consisting of a $2^{31}-1$ PRBS. As stated in Sec 2.1, such a long bit stream would not be feasible in simulation; thus, I replaced the OOK-modulated signal with a single pulse, whose duration $T_s = 3\,\mu$s is sufficiently long to overcome the transient time of LPA [41] (Sec. 2.1.3). In Sec. 2.3.7, I demonstrate that such a pulse represents an OOK-modulated bit packet (e.g., $3*10^4$ bits @10 Gb/s), with the same average power and energy. Thanks to the random birefringence of the fiber ($D_{PMD} = 0.05$ ps/km$^{1/2}$, as typical for modern fibers [61]), propagation is governed by the Manakov equation (1.18) [38,41], where the Kerr effect is isotropic, on the Poincaré sphere. Hence, any pump SOP is expected to attract the probe SOP in the same way [44].

I thus chose, without loss of generality, a linear horizontal pump SOP ($\hat{s}_1$), and obtained the simulation results shown in Fig. 2.10, plotted in the same framework as those reported in Fig. 2.7. Results refer to a right-circular input probe SOP ($\hat{s}_3$) (Fig. 2.10(a)), here chosen as an example, that yields the depolarization traces reported in Fig. 2.10(b) (10 traces, plotted every km of propagation). The probe average SOPs, plotted on a finer scale in Fig. 2.10(c), show that attraction occurs towards the pump SOP, along a spiral trajectory, that tends to collapse onto the input pump SOP. The probe depolarization is visible in the DOP_S curve in Fig. 2.10(d), while the pump depolarization is negligible here, being the pump much longer than the probe duration. Full results, as in Fig. 2.10(a-d), are obtained with the SCAOS algorithm in 54 min. computation time, on an ordinary PC. More details on the dynamics of LPA, occurring within a long randomly birefringent fiber, are provided in Sec. 2.3.4.

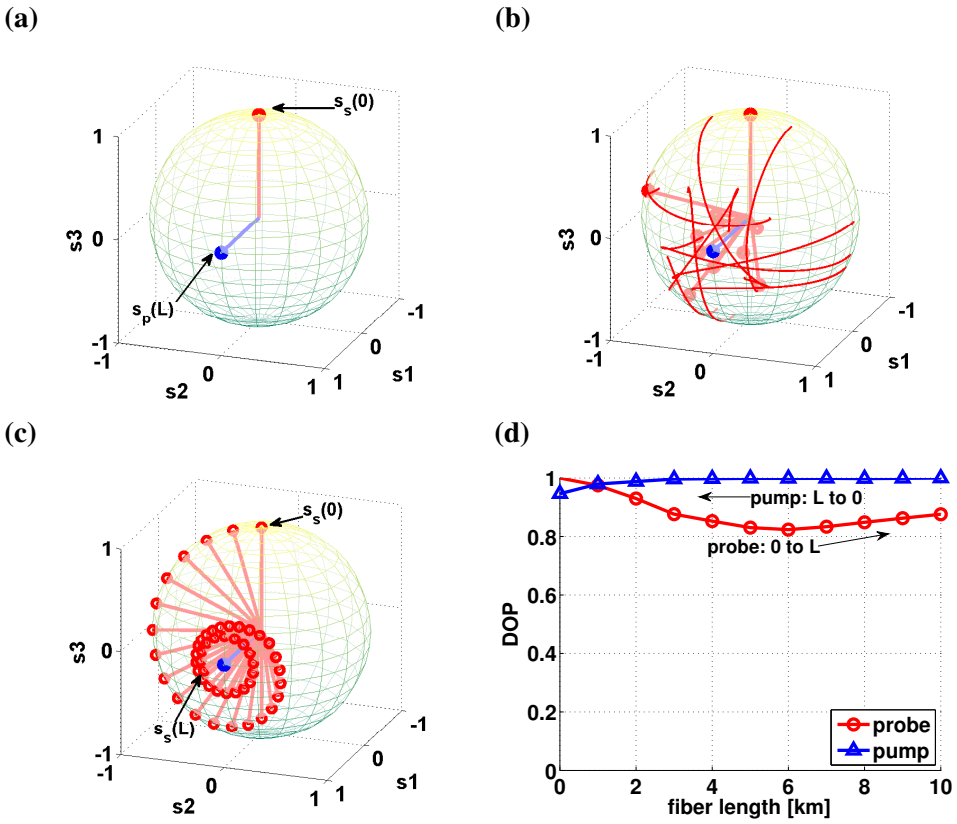

Figure 2.10: Lossless polarization attraction (LPA) of a probe pulse towards a (linear horizontal) CW pump, in a long (10 km) fiber. (a) input signals SOPs ($\chi_{in} = 90°$) (red: probe, blue: pump); (b) probe SOP traces along z; (c) motion of the average probe SOP (red) along z, showing the attraction towards the (blue) pump SOP; (d) resulting DOP, along z.

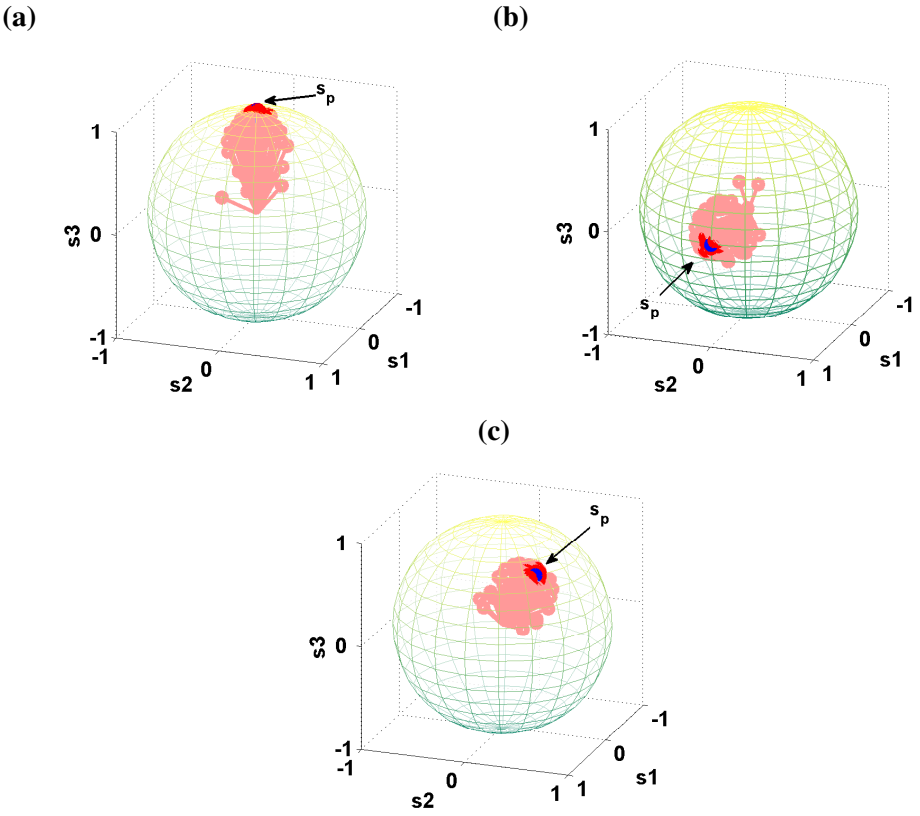

Figure 2.11: Average probe SOP (red), at the output of a long (10 km) lossless polarization attractor (DOP=magnitude). Plots obtained for 50 random input SOPs, in the case of a circular (a), linear (b), and elliptical (c) pump SOP (blue).

Repeating the experiment for 50 random input probe SOPs (the same as in Fig. 2.9(a)), yields similar results, as visible in figure 2.11(b), reporting the corresponding average output probe SOPs. Polarization attraction is testified by the 50 vectors surrounding the attracting pump SOP ($\hat{s}_1$), and the output $\mathrm{DOP_S}$ are reported as the vectors' magnitude. Figs. 2.11(a,c) complete the picture, by verifying numerically that a different choice of the pump SOP does not change the attractor's performance, at the output. Thanks to the isotropy of the Kerr effect, in the context of the Manakov equation (and contrary to the case of a short highly-nonlinear fiber discussed in Sec. 2.2.1), all pump polarizations are equally effective in attracting the input probe SOPs. The overall performance, as quantified by the time- and ensamble-averaged DOP is equal 0.80, 0.76, and 0.78, respectively, for the tested right-circular, linear horizontal, and elliptical pump SOPs, reported in Fig. 2.11(a-c). Since the probe SOPs are always attracted onto the input pump SOP, for every input pump SOP, it is always $\mathrm{DOP} = \overline{\mathrm{DOA}}$.

2.3 Design guidelines for a Counter-propagating NLP

In Sec. 2.2, I show how LPA can be generated either in short isotropic or in long randomly birefringent fibers. While LPA occurring within a short isotropic fiber require a circular pump SOP and very large signal powers (tens of watts) to be effectively generated, LPA occurring within a long telecom fiber happens towards every pump SOP and requires moderate signal powers (few watts/hundred of milliwatts). As a logical consequence, most of the research about the counter-propagating NLP has concentrated the attention on devices designed with a long telecom fiber [38–41, 45–47]; so did I, leaving aside the study of LPA occurring within a short fiber.

Since the transient time of LPA is in the microsecond scale [41], complete attraction within a counter-propagating NLP is only an asymptotic condition, hence the attraction of the mean signal SOP occurs at the expense of its DOP, which degrades partially [41, 44, 46]. Thus, a counter-propagating NLP is effective only on signals whose duration and polarization coherence time are larger than such a transient time, hence on "long", i.e., in the μs scale, signals with slowly-varying SOP. Thinking of a real practical application of the NLP, this can be a problem in a packet switched scenario (e.g., the Ethernet), where the duration of signals (bit-packets) can hardly reach the microsecond scale, i.e., the same order of magnitude as the transient time of LPA. In fact, typical packets size in a packet-switched optical network ranges from 8 to 1452 bytes, hence considering a bitrate $R = 10$ Gb/s, it ranges from a few nanoseconds to about a microsecond.

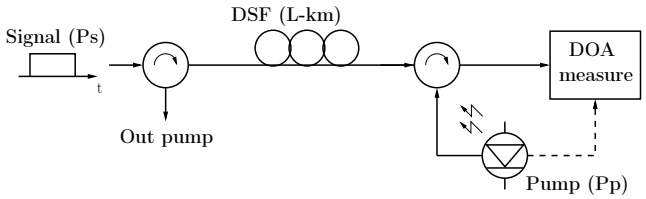

Figure 2.12: System setup of the nonlinear lossless polarizer (NLP). The NLP is composed by the fiber along with the (fully-polarized) pump laser, with power P_p, and the optical circulators.

In the following, I analyze the performance of a counter-propagating NLP in controlling the SOP of an amplitude modulated optical signal characterized by a slowly-varying SOP, i.e., whose polarization is constant over the entire packet (I will call such a scenario packetwise polarized signal). Since the relative propagation speed between pump and signal is fixed and relativistic (i.e., equal to the speed of light), the main design parameters for the counter-propagating NLP are just the injected pump and signal power and the nonlinear fiber length. Thus, considering a representative packet with duration comparable to the NLP transient time, I characterize the LPA phenomenon as a function of both power and fiber length, providing the design guidelines to select their values, so that the NLP achieves the desired performance. Moreover, I quantify the performance degradation when the packet duration falls below the NLP transient time.

2.3.1 System setup

I simulated a counter-propagating NLP similar to that described in Sec. 2.2.2. The NLP is composed by a nonlinear, dispersion-shifted fiber (DSF), with Kerr coefficient $\gamma = 1.99\,\mathrm{W}^{-1}\mathrm{km}^{-1}$ and attenuation $\alpha = 0.2$ dB/km, and a fully-polarized (CW) pump laser, with power $P_p = s_{0p}$, as shown in Fig. 2.12. The randomly birefringent fiber, with length L km, has a PMD coefficient $\mathrm{D_{PMD}} = 0.05$ ps/km$^{1/2}$, so that propagation is governed by the Manakov equation [38, 57]. Hence, the Kerr effect is isotropic on the Poincaré sphere and polarization attraction occurs towards any fixed pump SOP (as shown in Sec. 2.2.2), here chosen as linear horizontal ($\hat{s}_p = \hat{s}_1$). I assumed that the input signal consists of a single intensity-modulated pulse, with duration to $T_s = 1\ \mu$s and power $P_s = s_{0s}$, placed at the fiber zero-dispersion wavelength. Indeed, such a pulse represents an OOK-modulated bit packet (e.g., 10^4 OOK bits at 10 Gbit/s), as demonstrated in Sec. 2.3.6.

To avoid packet-to-packet nonlinear interactions mediated by the pump, I assume, for the moment, that only one packet travels into the NLP at a time, so that it interacts with a "fresh" pump portion which had not interacted with any other packet before. In Sec. 2.3.6, the case of more packets traveling together along the NLP is analyzed and commented.

As highlighted by the box in Fig. 2.12, the DOA was measured, according to equation (1.34) (as introduced in chapter 1), based on the output signal and on the input pump SOP $\hat{s}_p$ (dashed line in Fig. 2.12). I assumed that the changes in signal polarization are either due to a switch of the input bit-packet (pulse) or they are brought about by the birefringence and PMD of the preceding optical link, hence are slowly varying, on a time scale longer than the pulse period. Thus, I injected into the fiber a completely-polarized input signal (i.e., a packetwise polarized signal), $\overrightarrow{s}_s^{in}(t) = s_{0s}^{in}(t)\hat{s}_s^{in}$, where $\hat{s}_s^{in}$ is constant over the whole duration T_s, and lies at an angular distance χ_{in} (on the Poincaré sphere) from the input pump SOP.

2.3.2 The role of fiber length

Being LPA driven by the nonlinear XpolM induced by the pump, one can expect that its effect is proportional to the *nonlinear phase rotation* (NPR) $\phi_{NL} = \gamma P L_{eff}$, where P is the power and $L_{eff} = (1-\exp(-\alpha L))/\alpha$ is the *effective fiber length*. The NPR ϕ_{NL} is a physical parameter that quantifies the strength of the nonlinear Kerr interaction; it is thus natural to analyze how the effectiveness of LPA depends on power and fiber length.

Fig. 2.13 shows the contour plots of the DOA (Fig. 2.13(a)) and of its factors, defined in equation (1.34) (as discussed in chapter 1), $\mathrm{DOP_S}$ and MSA (Figs. 2.13(b,c)), as a function of both power and effective length. Results were obtained by launching the same power for pump and signal ($P_p = P_s = P$), while the maximum value $L_{eff} = 13$ km, in the figures, corresponds to a physical fiber length $L = 20$ km, beyond which the nonlinear effects have decayed significantly. As explained in chapter 1, results depend on the launched signal polarization, and in particular on the angular distance χ_{in} between pump and signal SOPs. Here, I chose the linear horizontal and vertical polarization components of the input signal $\overrightarrow{s}_s^{in}(t)$ with equal power and with a random phase offset, which determines an angle $\chi_{in} = 90^\circ$ between $\hat{s}_s^{in}$ and the linear horizontal pump polarization $\hat{s}_p$ (χ_{in} does not depend on the phase offset). The equilateral hyperbola plotted onto the DOA contours in Fig. 2.13(a) with a solid (magenta) line highlights the locus of points with constant ϕ_{NL}. I see that DOA is not directly proportional to ϕ_{NL}, thus denying the intuitive hypothesis formulated above. For a fixed ϕ_{NL}, LPA is more effective when powerful signals propagate

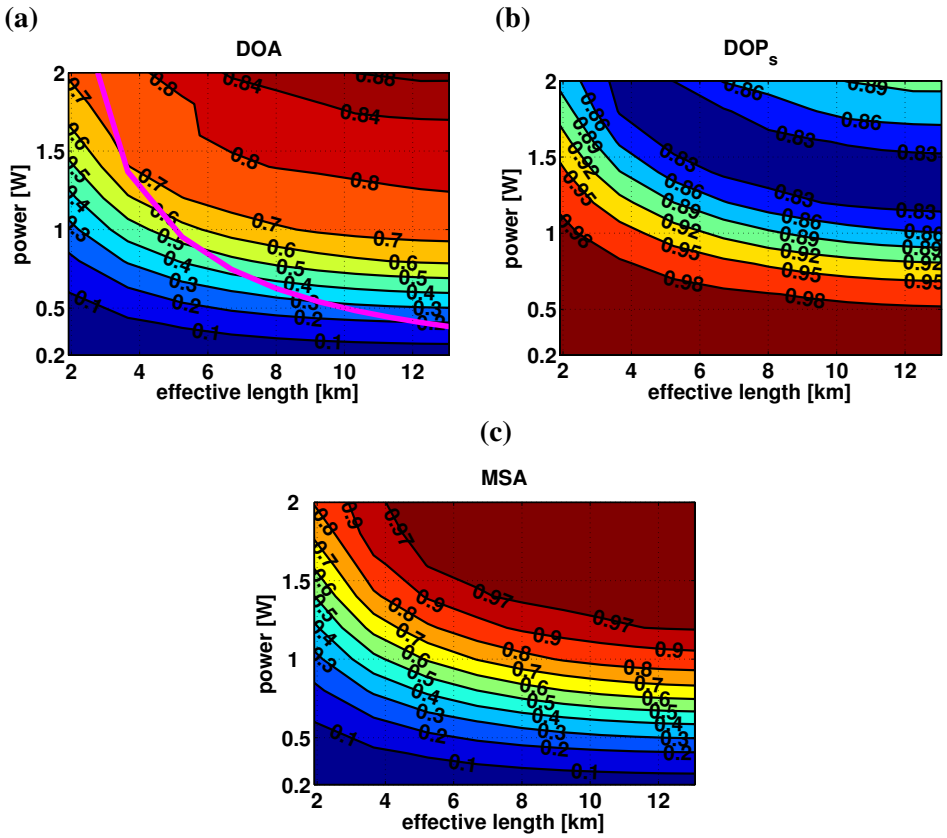

Figure 2.13: LPA effectiveness as a function of equal pump and signal power (P) and of effective fiber length (L_{eff}): (a) degree of attraction (DOA); (b) degree of polarization of the signal (DOP_S); (c) mean SOP attraction (MSA). The angular distance between the input signal and pump SOPs is $\chi_{in} = 90^\circ$ (on the Poincaré sphere).

in a short fiber. Geometrically, the DOA contours tend to "flatten", as a function of the effective length, meaning that the DOA increases little, by further lengthening the fiber. Note however that, for the signal SOP launched here, the initial value is $\mathrm{DOA_{in}} = \cos(\chi_{in}) = 0$, thus, from a null value, the DOA in Fig. 2.13(a) increases monotonically with the strength of the nonlinear interaction. Such a result is considerable, since the DOA in (1.34) is affected by an unavoidable $\mathrm{DOP_S}$ degradation, entailed in the dynamics of LPA [41, 44], as shown in Fig. 2.13(b), at intermediate values of the nonlinear phase ϕ_{NL}. Anyway, Figs. 2.13(b,c) show that the $\mathrm{DOP_S}$ decrease is more than compensated by the growth of MSA, so that their product (DOA) is increasing monotonically.

So far, only signal SOPs with an intermediate angular distance from the pump, $\chi_{in} = 90^\circ$, have been considered. To enlarge the picture, Fig. 2.14 shows the DOA (Fig. 2.14(a)), and its factors (Fig. 2.14(b,c)), obtained for different input signal SOPs: curves, with different symbols (and colors), correspond to (top to bottom) an increasing angular distance χ_{in} from the input pump SOP $\hat{s}_p = \hat{s}_1$, ranging from 0° to 180° in 30° steps. For the moment, I analyze only the dependence on L_{eff}, deferring the dependence on power to the next section. In Fig. 2.14, the curves were obtained with equal signal and pump power $P = 2$ W, a large value chosen to stress polarization attraction. The extreme χ_{in} values, plotted with symbols $\triangledown$ (dark green) and $\triangle$ (magenta), refer to a signal SOP equal or orthogonal to the input pump SOP, i.e., $\hat{s}_s^{in} = \pm\hat{s}_p$. In this case, signals propagate without any change in polarization, since their nonlinear interaction is of a *scalar* type, reducing to a simple *cross-phase modulation* (XPM). Hence, the DOA remains constant and equal to its input value. For every other input signal SOP, the DOA increases with increasing effective length, along with the amount of nonlinear interaction. In the right side of each curve in Fig. 2.14(a), DOA values tend to "saturate", for effective lengths above 8 km. The DOA value at which saturation occurs is smaller for input signal SOPs that are further away from the input pump SOP. Note that such a saturation phenomenon is due solely to the depolarization of the signal. In fact, while the MSA values in Fig. 2.14(c) are all close to 1 (except for orthogonal input SOPs), the depolarization of the signal, in Fig. 2.14(b), is larger for input signal SOPs further away from the pump. Anyway, even for such large χ_{in} values, results show that the DOA increases most within the first $L_{eff} = 8$ km (i.e., $L = 10$ km), a length after which the performance of the LPA process does not significantly improve.

The interest in using short fibers is due to PMD, since, in a randomly birefringent fiber, a large PMD coefficient can spoil polarization attraction, if the fiber is too long, due to the incoherent polarization evolution of pump and signal, located at different

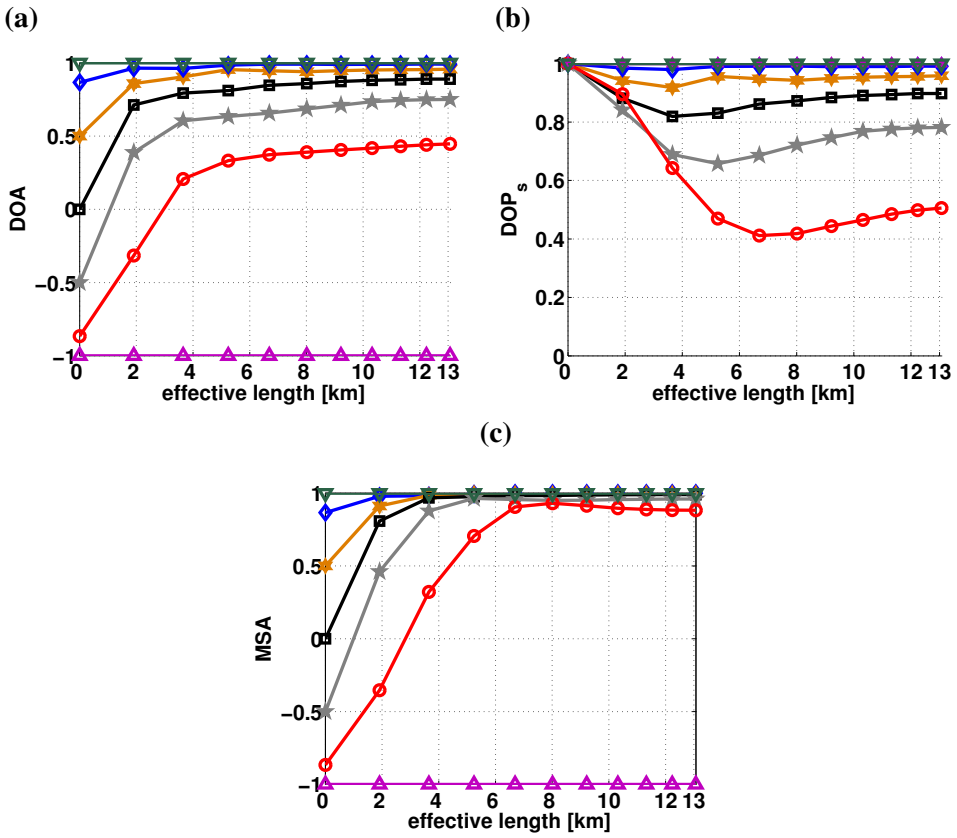

Figure 2.14: LPA effectiveness as a function of the effective fiber length (L_{eff}), with equal signal and pump power $P = 2$ W: (a) DOA; (b) $\mathrm{DOP_S}$; (c) MSA. Lines refer to an angular distance between the input signal and pump SOPs that varies (top to bottom) from $\chi_{in} = 0°$ to $\chi_{in} = 180°$, in 30° steps.

wavelengths [45]. I thus conclude that $L = 10$ km is a good compromise, to maximize LPA performance when the impairments due to PMD are not severe. In the remainder of this section, the fiber length is consequently fixed at $L = 10$ km, while I concentrate on the impact of optical power on the LPA effectiveness.

2.3.3 LPA dependence on signal and pump power

To characterize the effectiveness of LPA as a function of power, Fig. 2.15 shows the contour plots of the DOA and of its factors, $\mathrm{DOP_S}$ and MSA, in the case of a fiber with length $L = 10$ km, obtained by independently varying the pump and probe input power, P_p and P_s, in a range of practical interest, between 0.2 and 2.2 W. Here, as in Fig. 2.13, the input signal SOP $\hat{s}_s^{in}$ lies at an angular distance $\chi_{in} = 90^\circ$ from the input pump SOP ($\hat{s}_p = \hat{s}_1$).

Again, the DOA (Fig. 2.15(a)) increases monotonically with powers, despite the initial decrease of $\mathrm{DOP_S}$ (Fig. 2.15(b)), at low powers, which is more than compensated by the MSA increase (Fig. 2.15(c)).

The noteworthy result revealed by Fig. 2.15 is that all contour plots overlap with equilateral hyperbolae, as can be seen in Fig. 2.15(a), where three hyperbolae with solid thick lines (red, blue, green) are superimposed on the DOA contour plots. Consequently, in the tested range of power, the DOA, the $\mathrm{DOP_S}$ and the MSA all depend on the pump-signal power product. I verified numerically that this is true for any launched signal SOP, hence a plot of the DOA (and of its factors) as a function of $P = (P_s P_p)^{1/2}$ (defined as the geometric mean of pump and signal power) contains all the necessary information. As a practical implication, even the polarization of a weak signal can be effectively attracted towards the pump polarization, provided that the pump is powerful enough. On the other hand, assuming, for instance, to fix a value for the overall power ($P_s + P_p$) injected into the NLP (the locus of such points is represented in Fig. 2.15(a) by a straight lines with negative unitary slope), the best LPA effectiveness occurs when the total power is equally distributed between the two interacting signals, i.e., for equal signals power. In other words, the NLP works more efficiently when the instantaneous nonlinear interactions between probe and pump, due to the Kerr effect, are symmetric, i.e., when the pump acts on the probe in the same way in which the probe acts on the pump. Note that the dependence of DOA on the signals power product is not at all intuitive, since no such term appears in the pump and probe propagation equations (see chapter 1, Sec. 1.2.3). Moreover, pump and probe play different roles in the setup in Fig. 2.12, the pump being a CW signal (with infinite energy) and the probe being a single pulse with finite duration. Finally, the dependence on the pump-signal power product P^2 of the DOA, could suggest that

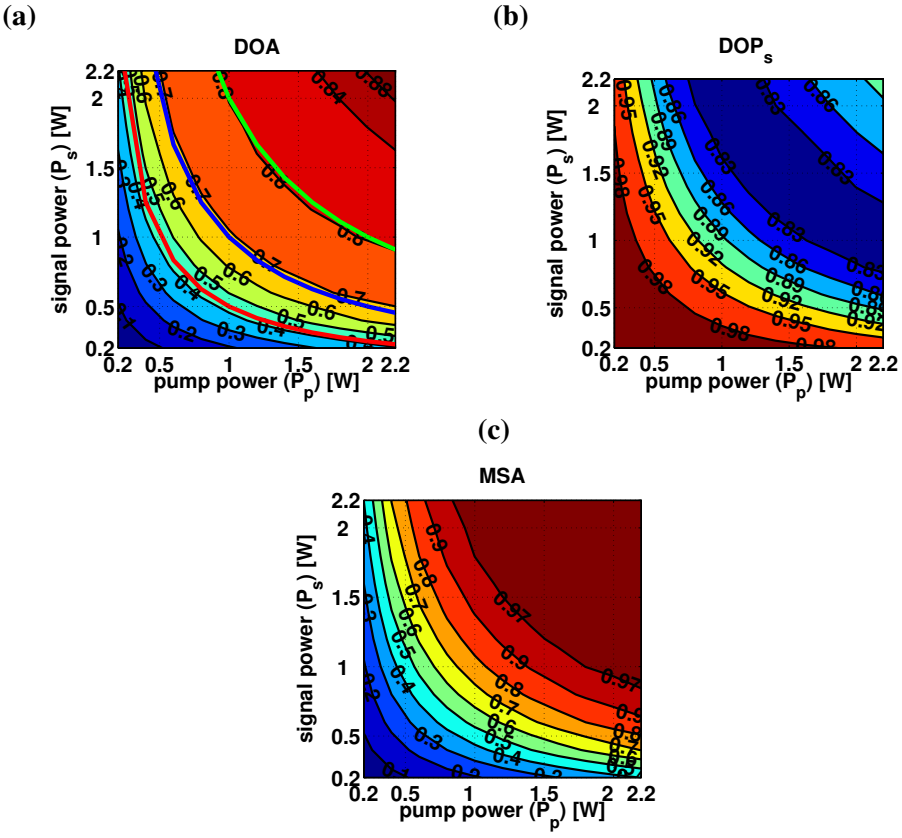

Figure 2.15: LPA effectiveness as a function of signal and pump power: (a) degree of attraction (DOA); (b) degree of polarization of the signal (DOP_S); (c) mean SOP attraction (MSA). The angular distance between the input signal and pump SOPs is $\chi_{in} = 90^\circ$ (on the Poincaré sphere).

it could be proportional to the quantity $P^2 L_{eff}$. I verified that this is not the case, by superimposing a curve, with constant $P^2 L_{eff} = c$, to the contour plots in Fig. 2.13(a) (not reported in figure).

Relying on such a noteworthy result, Fig. 2.16 shows the dependence of the DOA, the $\mathrm{DOP_S}$ and the MSA on the geometric mean power P, for a launched signal SOP with an increasing angular distance χ_{in} from the input pump SOP, ranging from 0° to 180° in 30° steps.

From Fig. 2.16, three different *"regimes of operation"* can be identified for the NLP device. At low power ($P \leq 0.5$ W), signals propagate in a *quasi-linear regime*, where the input signal SOP is almost unchanged and, from (1.34), the DOA is close to its initial value $\mathrm{DOA_{in}} = \cos(\chi_{in})$. At intermediate power ($0.5\ \mathrm{W} < P < 1.5\ \mathrm{W}$), signals propagate in a *nonlinear regime*, where the output signal SOP tends to align, on average, to the input pump SOP (see the increase in MSA, in Fig. 2.16(c)), at the expense of its degree of polarization ($\mathrm{DOP_S}$ decreases, in Fig. 2.16(b)), as was already pointed out. In this region, the DOA versus power curves, in Fig. 2.16(a), show the largest slope, hence the Kerr effect, and in particular the XPolM, is maximally effective in terms of polarization attraction. At large power ($P > 1.5$ W), signals propagate in a *strongly nonlinear regime*, where the average output signal SOP has become aligned with the pump SOP (MSA $\backsimeq 1$), regardless of input signal polarization (except in the case of an almost orthogonally polarized input signal, $\chi_{in} \simeq 180^\circ$), and its $\mathrm{DOP_S}$ start to increase slowly. This is due to a repolarization of the signal around its average SOP, i.e., around the pump SOP, as already stated in Sec. 2.2. However, the dynamics of such a repolarization are slow, hence the lowest $\mathrm{DOP_S}$ that the signal reaches sets a practical limit to the attainable DOA values.

As stated, the DOA is strongly linked to the angular distance χ_{in} between the input signals Stokes vectors, since it takes values in the range $\cos(\chi_{in}) < \mathrm{DOA} < 1$, as shown in Fig. 2.16(a). Thus, it is difficult to directly compare the NLP effectiveness obtained for different polarizations of the input signal. To overcome this problem, I normalized the DOA with respect to its initial condition, i.e., with respect to $\cos(\chi_{in})$, by defining a *rescaled* version for the DOA, named $\mathrm{DOA_r}$, as

$$\mathrm{DOA_r} \triangleq \frac{\mathrm{DOA} - \cos(\chi_{in})}{1 - \cos(\chi_{in})}. \tag{2.2}$$

The $\mathrm{DOA_r}$, that corresponds to a shifted (by $\cos(\chi_{in})$) and rescaled (by $[1-\cos(\chi_{in})]^{-1}$) version of the DOA, takes value ranging from 0 to 1, regardless of the input probe polarization. Despite the $\mathrm{DOA_r}$ theoretically allows to directly compare the effectiveness of the NLP in attracting signals with different polarizations, I found that it

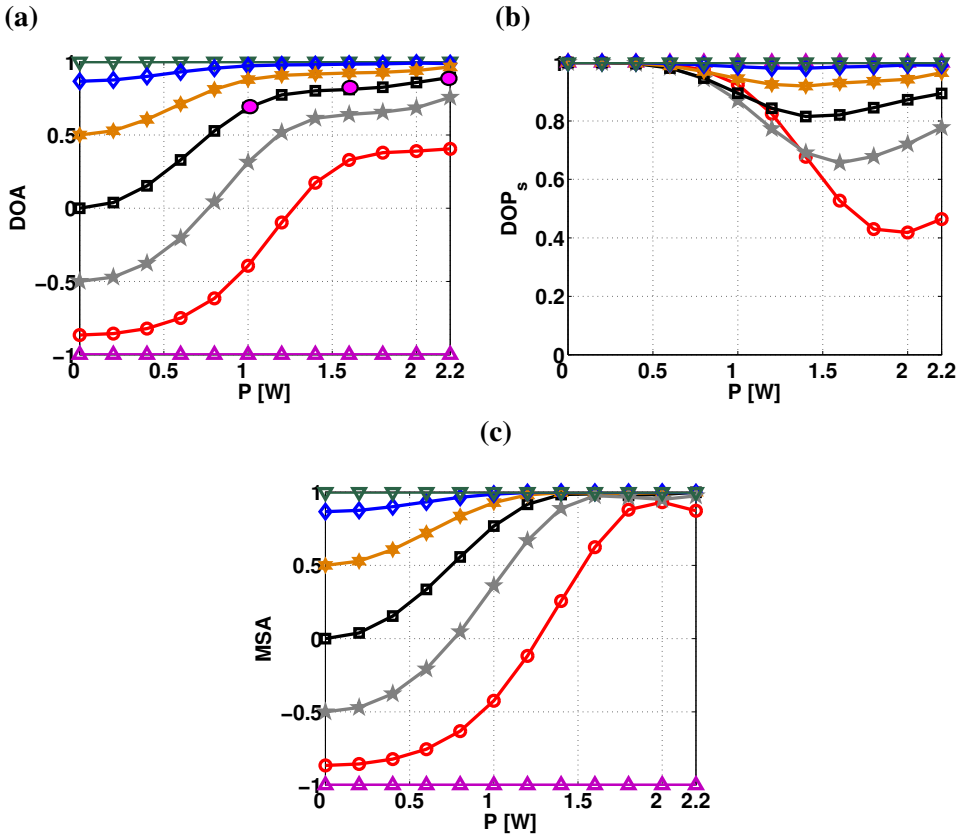

Figure 2.16: LPA effectiveness as a function of the geometric mean power $P = (P_s P_p)^{1/2}$: (a) DOA; (b) $\mathrm{DOP_S}$; (c) MSA. Lines refer to an angular distance between the input signal and pump SOPs that varies (top to bottom) from $\chi_{in} = 0^\circ$ to $\chi_{in} = 180^\circ$, in 30° steps.

is affected by numerical instability. In fact, the closer the input signal SOP to the input pump SOP, the closer the value of $\cos(\chi_{in})$ to 1, hence the closer the denominator in equation (2.2) to 0. For this reason, I quantify the performance of the NLP through the DOA leaving aside the $\mathrm{DOA_r}$. I shall not report numerical results that are meaningless for $\mathrm{DOA_r}$.

2.3.4 The dynamics of LPA

To better clarify the dynamics of LPA described in the previous section, it is helpful to visualize the quantities defined so far, i.e., DOA, MSA and $\mathrm{DOP_S}$ on the Poincaré sphere. Fig. 2.17 shows the signal SOP, on the left, along with the pulse power profile, on the right, at the fiber output. The *depolarization traces* (red), visible in Figs. 2.17(left), represent the time evolution of the signal pulse's SOP, $\hat{s}_s(t) = \overrightarrow{s}_s(t)/s_{0s}(t)$. The Stokes vector of each time sample is normalized to its power, so that the depolarization traces lie on the Poincaré sphere. The inner (red) vector represents the power-averaged signal SOP $\left\langle \overrightarrow{s}_s(t) \right\rangle / \left\langle s_{0s}(t) \right\rangle$ that appears in the definition of DOA (1.34), which is clearly related to the depolarization trace (although it is not equal to its mean value). Its magnitude is equal to the the $\mathrm{DOP_S}$, as per (1.34), while its direction is the unit magnitude vector $\hat{m}_s$, appearing in (1.35), hence χ is the angle that it forms with the input pump SOP, represented by the unit magnitude (blue) vector aligned with $\hat{s}_1$. The time evolution of the signal pulse's power $P_s(t) = \left\| \overrightarrow{A}_s(t) \right\|^2 = |A_{xs}(t)|^2 + |A_{ys}(t)|^2$, corresponding to the depolarization trace, is visible in Fig. 2.17(right), where the pulse power aligned with $(|A_{xs}(t)|^2$, solid line) and orthogonal to $(|A_{ys}(t)|^2$, dashed line) the input pump polarization are plotted, separately. In Fig. 2.17, the angle between the input signal and pump SOPs is $\chi_{in} = 90^\circ$, hence the input pulse power is equally distributed between the two orthogonal polarizations (x and y). Referring to the different propagation regimes, described in the previous section, such a power, equal to the pump power, is set in the *nonlinear regime* (1 W , in Fig. 2.17(a)), and at the onset (1.6 W , in Fig. 2.17(b)), or deeply in the *strongly nonlinear regime* (2.2 W , in Fig. 2.17(c)). These three system configurations are marked by circles, on the (black) line with □ symbols, in Fig. 2.16(a).

As stated repeatedly, LPA is a dynamic phenomenon where the signal SOP is attracted on average towards the input pump SOP, moving along a spiral trajectory (see Fig. 2.10(c) in Sec. 2.2.2). Anyway, the attraction process does not apply to every time sample of the signal in the same way, as evident in Fig. 2.17.

Focusing on the leading edge of the probe pulse (highlighted in Fig. 2.17-right), I describe now its trajectory along the fiber. Due to the counter-propagation sce-

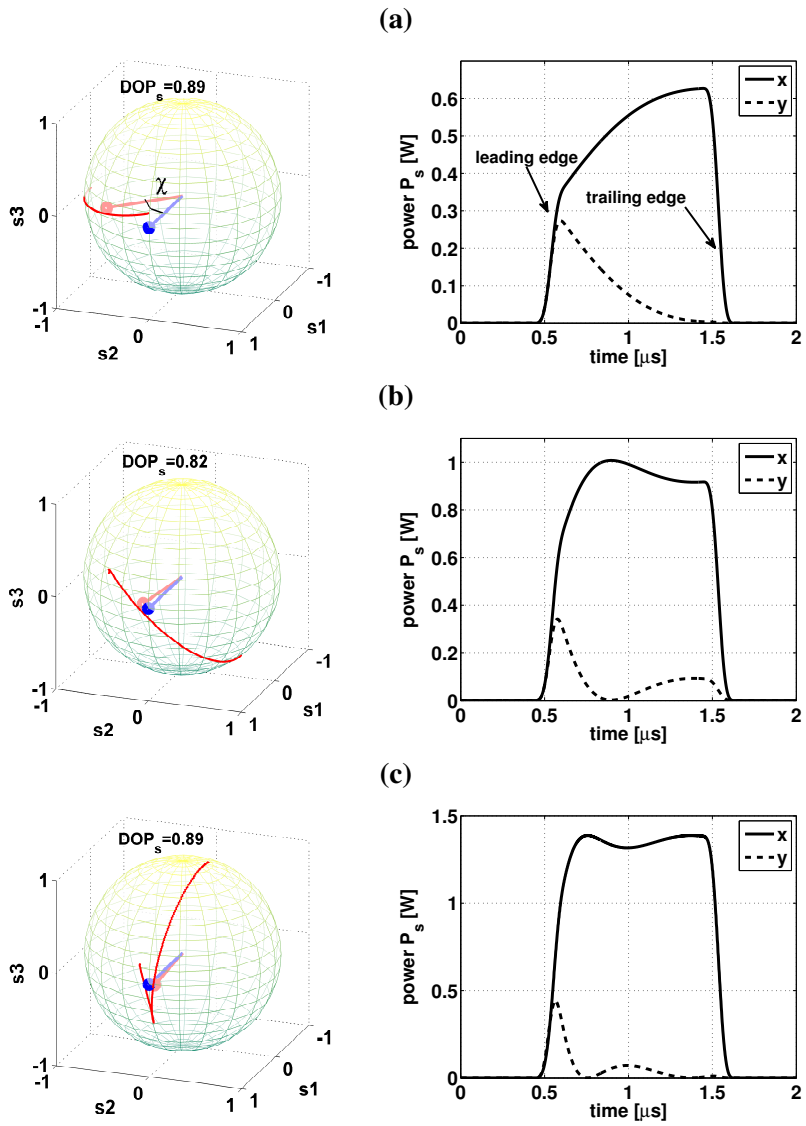

Figure 2.17: State of polarization (SOP) of the signal at the output of the NLP (left) and pulse power profile (right), for an equal signal and pump power of: 1 W (a), 1.6 W (b), and 2.2 W (c). The angular distance between the input signal and pump SOPs is $\chi_{in} = 90°$. The angle between the average output signal SOP (red) and input pump SOP $\hat{s}_1$ (blue) is $\chi = 40°$ (a), $\chi = 8°$ (b) and $\chi = 4°$ (c), while the output signal DOP_S is 0.89 (a), 0.82 (b) and 0.89 (c).

nario, the probe leading edge always interacts with a "fresh" pump portion, that moves against it, having the initial SOP ($\hat{s}_3$, in my case). Thus, due to equation (1.30), the probe leading edge always rotates around the input pump SOP, hence it is never attracted towards it, since its angular distance χ from the input pump SOP never changes along the fiber. As a consequence, all the depolarization traces in Figs. 2.17(left) start on the $(\hat{s}_2, \hat{s}_3)$ circle.

Instead, the following portions of the probe pulse interact with time samples of the pump that have already interacted with the probe, hence whose SOP has been modified. Such an interaction gives rise to the depolarization trace, which demonstrates how the pulse SOP moves towards the pump SOP. The stronger the signal power, the larger the time extension of that trailing part of the signal pulse attracted towards the pump SOP. As explained therein, the leading time-slice of the probe interacts with the leading time-slice of the pump, so as to move them "in favor" of the following time-slices of the probe, which are dynamically attracted towards the pump SOP, at the expense of a depolarization of the leading time-slice. In the strongly nonlinear regime of Fig. 2.17(c), where the average signal SOP is already very close to the pump SOP, the increased power implies that the signal repolarizes around the input pump SOP, hence that $\mathrm{DOP_S}$ increases, as can be seen by comparing the (identical) $\mathrm{DOP_S}$ values related to Figs. 2.17(a) and (c). In Fig. 2.17(a), much of the pulse has a SOP close to that of its leading edge (i.e., with equal power on A_{xs} and A_{ys}), while in Fig. 2.17(c), most of the pulse has a polarization close to that of the attracting pump SOP (i.e., with power on A_{xs} only). The description of these dynamics well explains why the LPA phenomenon is the joint product of Kerr-induced nonlinear polarization rotation and the walk-off between the signals. In chapter 3, I will show how the effectiveness of LPA strongly depends on the balance between the amount of the nonlinear interaction and of the walk-off.

The discussion above leads to an important conclusion concerning the maximum value obtainable for the DOA (theoretically equal to 1). I can have $\mathrm{DOA} = 1$ only when both MSA and $\mathrm{DOP_S}$ are both equal to 1, i.e., when the output signal pulse is fully polarized, with the same polarization as the input pump. Since the leading edge (hence, for physical continuity, the initial portion) of the signal pulse will never be attracted towards the pump SOP, neither the MSA nor the $\mathrm{DOP_S}$ can reach their theoretical limit, unless the input signal already has the same SOP as the pump, i.e., in the trivial case $\chi_{in} = 0^\circ$. Consequently, $\mathrm{DOA} = 1$ only represents an asymptotic value for any signal polarization (except the one coinciding with the pump SOP $\hat{s}_p$), as can be seen in Fig. 2.16(a). Of course, for longer pulses, the portion closer to the leading pulse edge has less influence on the overall evaluation of $\mathrm{DOP_S}$, as demonstrated in

Sec 2.3.6.

The analysis of LPA dynamics clarifies the reason for which there exists a transient in LPA and short (picoseconds) pulses are not effectively attracted in a NLP in the counter-propagating configuration [41], so that a co-propagating configuration is required [34, 45] (which however poses other constraints, as described in Chapter 3).

2.3.5 Average performance of the NLP

The analysis performed so far assumes an input signal SOP that is deterministic, at least with respect to the angular distance from the attracting pump SOP, equal to a given χ_{in}. As discussed in Sec. 1.3.2 of chapter 1, the performance of LPA should instead be assessed with no prior knowledge on the input SOP, hence resorting to the ensemble-averaged DOA introduced in (1.3.2). Thus, I performed a statistical study of the DOA and of its factors (DOP_S and MSA), as a function of the (geometric) mean power P, defined above, in order to evaluate the average performance of LPA.

Figs. 2.18(a-c) show the dependence of the ensemble average of DOA, DOP_S and MSA versus P, while Figs. 2.18(d-f) report the standard deviation of the same quantities. The two expected values, mean and std. dev. (first and second order moments), were computed numerically from the "deterministic" curves in Fig. 2.16, that were averaged over the unknown angle χ_{in}, i.e., weighted by the distribution of χ_{in}. For an input signal SOP uniformly distributed over the Poincaré sphere, the probability density function (pdf) of the angular pump-probe distance is $f(\chi_{in}) = \frac{1}{2}\sin(\chi_{in})$ $(0 \leq \chi_{in} \leq 180^\circ)$ [64], hence $\chi_{in} = 90^\circ$ is its mean value. The curve reported in Fig. 2.18(a) is the most important result concerning the counter-propagating NLP characterization, at least from a practical viewpoint, since it yields the rule for setting the power levels, once the desired average-performance for the device is given.

As already noted in Sec. 1.3.2 (chapter 1), Fig. 2.18(a) shows that $\overline{\mathrm{DOA}} = E[\mathrm{DOA}] \in [0;1]$, which can be easily demonstrated as follows. When power tends to zero, the optical fields propagate in a linear regime, no polarization attraction occurs, and DOA coincides with its input value, $\mathrm{DOA_{in}} \simeq \cos(\chi_{in})$, with $0 \leq \chi_{in} \leq 180^\circ$. Hence, its average value can be calculated analytically as follows

$$\overline{\mathrm{DOA}}_{\mathrm{in}} \quad = \quad E[\cos(\chi_{in})] = \int_0^{\pi} \cos(\chi_{in}) \frac{\sin(\chi_{in})}{2} d\chi_{in} = 0.$$

When power increases, the DOA curves in Fig. 2.16 increase monotonically, towards the asymptotic value 1 (for all but the orthogonal input SOP case, for which DOA is always null), hence $\overline{\mathrm{DOA}}$ values cannot become negative.

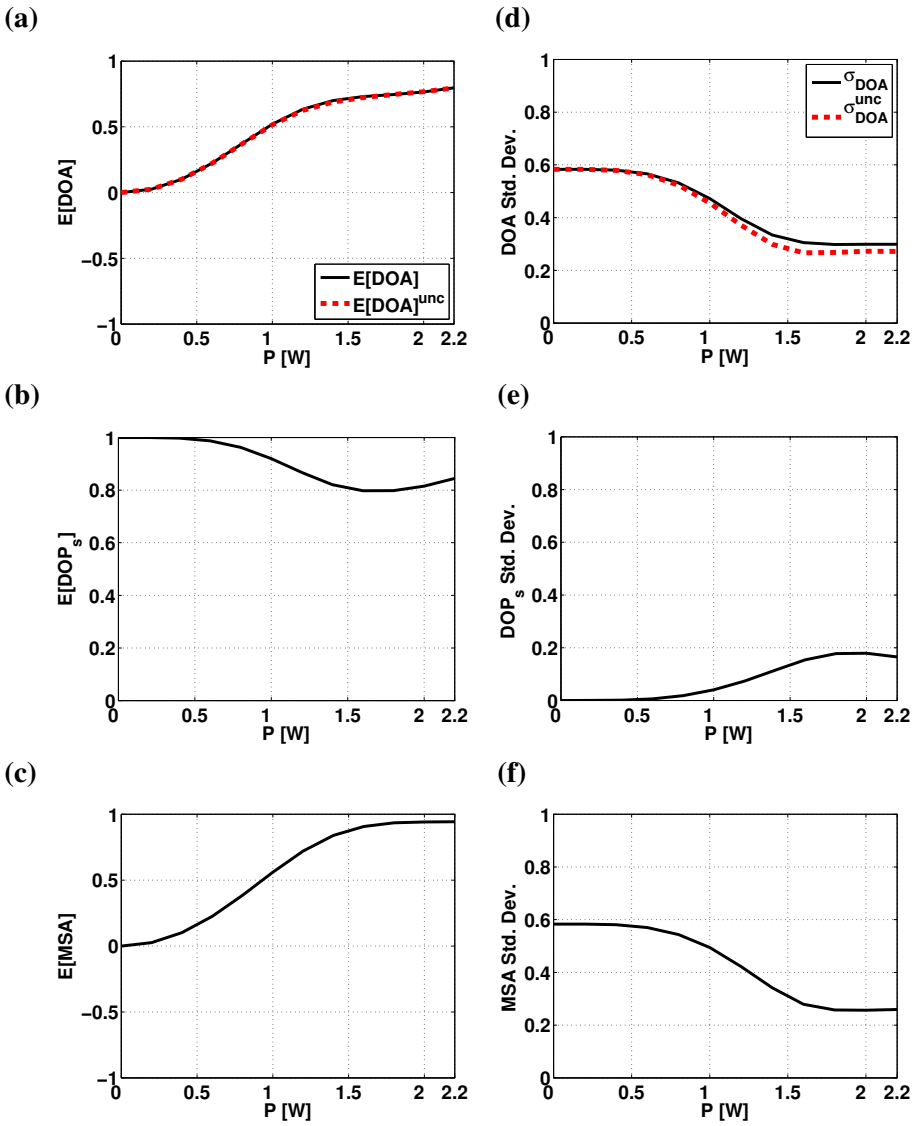

Figure 2.18: First and second order moments of the quantities used to characterize the performance of a NLP, as a function of (geometric) mean power: (a-d) degree of attraction (DOA); (b-e) degree of polarization of the signal (DOP_S); (c-f) mean SOP attraction (MSA). In (a,d), thick dashed lines report the first and second order statistics evaluated by assuming that DOP_S and MSA are uncorrelated random variables.

Regarding the DOA standard deviation in Fig. 2.18(d), it is decreasing monotonically with power and its maximum value, obtained when power tends to zero, can be again calculated analytically, from the DOA variance at the input, $\sigma^2_{\mathrm{DOA_{in}}} \triangleq E\left[\left(\mathrm{DOA_{in}}\right)^2\right] - \left(\overline{\mathrm{DOA}}_{\mathrm{in}}\right)^2$, as follows

$$\sigma^2_{\mathrm{DOA_{in}}} = E\left[\cos^2\left(\chi_{in}\right)\right] = \int_0^{\pi} \cos^2\left(\chi_{in}\right) \frac{\sin\left(\chi_{in}\right)}{2} d\chi_{in} = \frac{1}{3},$$

from which the maximum DOA standard deviation results, $\sigma_{\mathrm{DOA_{in}}} = (1/3)^{1/2} \simeq 0.577$. The same values are obtained for the first and second order statistics of the MSA (Figs. 2.18(c) and (f)) when power tends to zero, since I assumed a fully polarized input signal, for which $\mathrm{DOP}_{\mathrm{S}}^{\mathrm{in}} = 1$ always (see Figs. 2.18(b) and (e)), hence MSA = DOA, in this limit.

Even the curves in Fig. 2.18 seem to suggest the existence of three different operating regimes for LPA. In particular, in the strongly nonlinear propagation regime, $\overline{\mathrm{DOA}}$ and its standard deviation remains almost constant, meaning that a further increase of power would not lead to an appreciable enhancement of the performance of a NLP.

Since the DOA is the product between the MSA and the $\mathrm{DOP_S}$, its average is $\overline{\mathrm{DOA}} = E\left[\mathrm{MSA}\,\mathrm{DOP_S}\right]$ and its variance is $\sigma^2_{\mathrm{DOA}} = E\left[\mathrm{MSA}^2\,\mathrm{DOP}_{\mathrm{S}}^2\right] - \overline{\mathrm{DOA}}^2$. Assuming, for the moment, that the MSA and the $\mathrm{DOP_S}$ are statistically uncorrelated random variables, I evaluated the average $\overline{\mathrm{DOA}}^{\mathrm{unc}} = E\left[\mathrm{MSA}\right] E\left[\mathrm{DOP_S}\right]$ and the standard deviation $\sigma^{\mathrm{unc}}_{\mathrm{DOA}}$ accordingly, and plotted these quantities in Figs. 2.18(a)-(d), with thick dashed (red) lines. In particular, the dashed curve in Fig. 2.18(a) is the product of the two curves in Figs. 2.18(b,c). The dashed curves match very well with the moments of DOA (solid black lines), suggesting that MSA and $\mathrm{DOP_S}$ are indeed almost statistically uncorrelated. This would be a weird—though not impossible—fact, since the only random parameter in the system is the angle χ_{in}, from which both MSA and $\mathrm{DOP_S}$ deterministically stem from the propagation equation, thus being a transformation of the same random variable. Hence, although the statistical correlation between MSA and $\mathrm{DOP_S}$ is close to zero, the two variables cannot be statistically independent.

To give another, more immediate, representation of the average performance of a NLP, Fig. 2.19 shows the average output signal SOPs $\hat{m}_s$ (red, circles) obtained for the 100 random input SOPs in Fig. 2.19(a) (with uniform distribution on the Poincaré sphere), in the case of a (geometric) average power P equal to: 0.6 W (b),

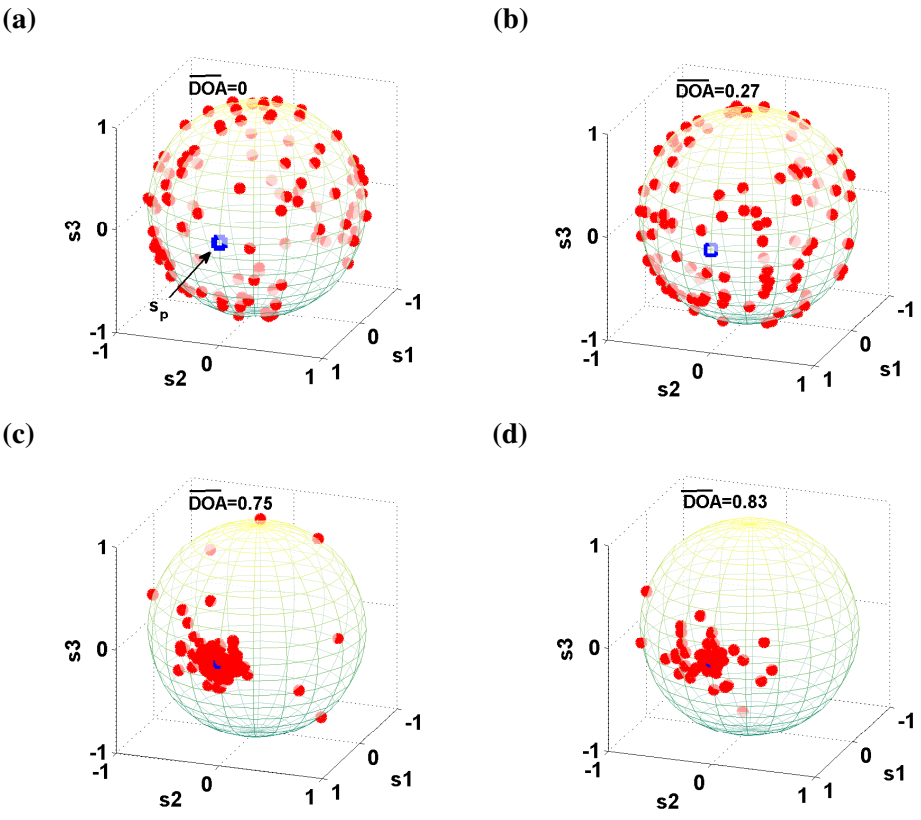

Figure 2.19: A graphical picture of lossless polarization attraction (LPA) towards the input pump SOP $\hat{s}_1$ (blue), for 100 random input signal SOPs (a). Average output signal SOPs (red) are plotted for increasing transmitted power: (b) 600 mW; (c) 1.6 W; (d) 2.2 W.

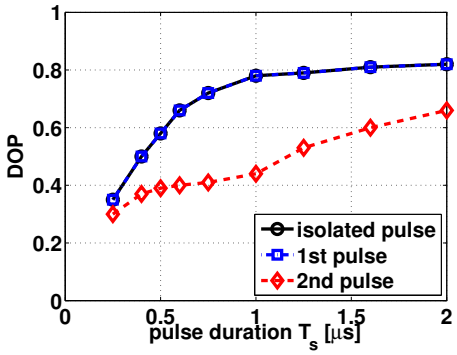

Figure 2.20: Performance of a counter-propagating NLP, obtained for completely polarized pulses with different durations. Different curves are obtained by injecting into the NLP an isolated pulse (solid with circles) or two consecutive pulses (dot-dashed with squares and dashed with diamonds).

1.6 W (c), and 2.2 W (d). The $\overline{\text{DOA}}$, evaluated by using Monte Carlo simulation over the 100 realizations of the input signal SOP, results: $\overline{\text{DOA}} = 0.27$, $\overline{\text{DOA}} = 0.75$, and $\overline{\text{DOA}} = 0.83$, for the tested power levels, respectively.

Although I use a small number of input signal SOPs in order to evaluate the (weighted-) average performance of the NLP reported in Fig. 2.18, this method provides results very close to those obtained with Monte Carlo averaging over 100 SOPs, reported in Fig. 2.19: namely, the two methods yield results that differ at most by 0.03.

2.3.6 The impact of packet-to-packet interaction

As already stated, the effectiveness of the counter-propagating NLP does not extend to signals with polarization coherence times much shorter than a microsecond, because of the longer transient time of the LPA process [41]. A degradation of the NLP performance for shorter signals can be observed in Fig. 2.20, reporting the DOP $= \overline{\text{DOA}}$ obtained at the NLP output, for signal pulses whose duration ranges from $T_s = 250$ ns to $T_s = 2$ μs, i.e., typical packets size for a packet-switched optical network operating at @10 Gb/s. In particular, the solid (black) line with circles, obtained by injecting isolated pulses into the NLP, shows how the DOP rapidly decreases by decreasing T_s, due to a signal duration shorter than the NLP transient time, while for longer pulses the DOP seems to saturate, around DOP $= 0.8$, confirming

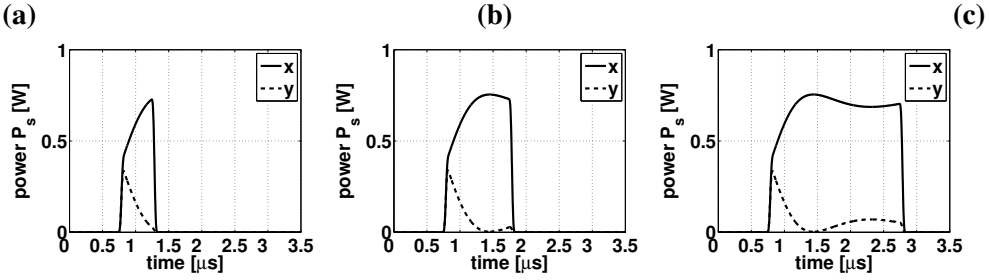

Figure 2.21: Time evolution of the probe pulse's power, at the NLP output, for different pulse durations $T_s = 0.5$ μs (a), $T_s = 1$ μs (b) and $T_s = 2$ μs (c). The power of the probe component aligned with (x, solid line) or orthogonal to (y, dashed line) the input pump are plotted separately.

that the transient time of a counter-propagating NLP is about 1 μs, in agreement with [41]. Indeed, the DOP grows continuously, although with a small slope, since for longer pulses, the pulse portion closer to the leading edge (which is not attracted) has less influence on the overall evaluation of the DOA, as stated in Sec. 2.3.4. In order to demonstrate this fact, Fig. 2.21 reports the time evolution of the probe pulse's power, when pulse duration is set at $T_s = 0.5$ μs (a), $T_s = 1$ μs (b) and $T_s = 2$ μs (c), for an angular distance between the input SOPs $\chi_{in} = 90°$. In Fig. 2.21, the power of the probe components aligned with (x, solid line) or orthogonal to (y, dashed line) the input pump are plotted separately. Moreover, in Fig. 2.21, as in Fig. 2.20, the input signals power is $P = 1.2$ W. Note that, due to the counter-propagation geometry, the first part of the pulse suffers the same fate. In fact, the first 0.5 μs in all three plots coincide exactly (and so do the first μs in Figs. 2.21(b) and (c)). The corresponding DOA values for the three pulse durations are DOA $= 0.58$ (Fig. 2.21(a)), DOA $= 0.77$ (Fig. 2.21(b)) and DOA $= 0.81$ (Fig. 2.21(c)).

Isolated pulses, always interact with an undistorted pump, while, in a realistic scenario, pulses propagate in sequence through the NLP. The dot-dashed (blue) line with squares and the dashed (red) line with diamonds in Fig. 2.20, show the DOP obtained at the NLP output by injecting two consecutive (polarized) pulses, with the same duration but with independent polarization. The DOP obtained for the first pulse (dot-dashed blue line) exactly coincides with that obtained for an isolated pulse (solid black line). This occurs because, thanks to the counter-propagating geometry of the NLP, the first pulse interacts with the pump in the same way as for an isolated pulse. This is no longer true for the following pulse (dashed red line), whose

DOP degrades significantly. This is due to its interaction with a pump portion that was previously distorted by the nonlinear polarization rotation occurred with the preceding pulse. Hence, the pump SOP is changed, with respect to its input SOP, and so are the polarization interactions between the pump and the second pulse. Despite the moderate increase of DOP versus pulse duration, the polarization attraction of the second pulse (dashed line in Fig. 2.20) is impaired and, if a third pulse propagated in sequence through the NLP, its resulting output DOP would be further degraded, as I numerically verified.

It is thus clear that pulse-to-pulse nonlinear interactions mediated by the pump are detrimental for the NLP operation. **Indeed, within LPA, the pump represents a resource that "is consumed" by the signal pulses.** To guarantee a "refreshing" of the consumed pump, and to avoid the consequent performance degradations, a guard interval is needed, between two consecutive pulses injected into the NLP, enabling the distorted portion of the pump to exit the NLP.

2.3.7 LPA with an OOK-modulated signal

In this section, I prove that amplitude modulation of the probe signal is not a detrimental issue for the attraction of its polarization towards the input pump polarization (as already shown experimentally in [2]). Moreover, I show that the performance of the counter-propagating NLP acting on a (fully polarized) modulated bit-packet, is the same as that obtained by the NLP acting on a single pulse, provided that the average power and energy are the same. Thus, all results shown in this chapter, obtained for a single pulse, extend to modulated bit-packets.

To pursue this aim, I numerically simulated the system setup in Fig. 2.12, where, instead of a single pulse, the probe input signal consists of an OOK-modulated bit packet, with non-return to zero (NRZ) pulses (with ideal extinction ratio), duration $T_s = 1\ \mu$s and average power P_s (hence, with peak power $2P_s$). To avoid packet-to-packet nonlinear interactions mediated by the pump, I assumed that the guard interval between two consecutive packets is guaranteed.

As stated in Sec. 2.1.3, the numerical simulation of a counter-propagating NLP acting on a signal modulated with a bitrate $R = 10$ Gb/s is unworkable, at least for long fibers, since too many symbols should be sent, due to the zero padding, to guarantee the reliability of results. Thus, I gradually increased the bitrate R of the probe, starting from $R = 1$ Mb/s, up to $R = 40$ Mb/s, which is enough to pursue my goal within a limited timeframe. Since the packet duration T_s is fixed, increasing R means increasing the number of bit within the packet.

Fig. 2.22 shows the DOA, as obtained with different bitrates, as a function of

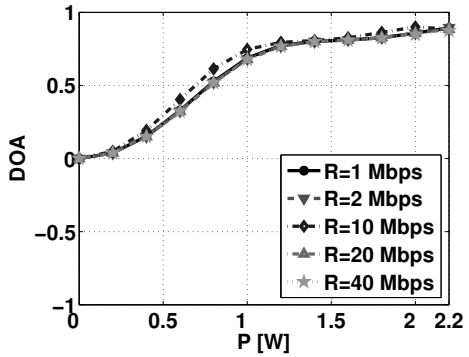

Figure 2.22: Degree of attraction (DOA) of an OOK-modulated bit-packet, with fixed duration $T_s = 1\ \mu s$ and different bitrate R. The angular distance between the input signal SOPs is $\chi_{in} = 90°$.

the probe-pump power $P = (P_s P_p)^{1/2}$, when the angular distance between the input signals SOPs is $\chi_{in} = 90°$ (the pump is linearly horizontal polarized). In Fig. 2.22, the DOA values are almost the same for all the tested bitrates, since the average power and energy[2] were kept constant. To ensure this, when $R = 1$ Mb/s or $R = 2$ Mb/s, the pattern was fixed "a priori", so that it takes value "1" or "10", respectively. On the other hand, when $R = 10$ Mb/s, $R = 20$ Mb/s or $R = 40$ Mb/s, the pattern was randomly generated, with independent and identically distributed (iid) bits. In the case of $R = 1$ Mb/s, the transmitted probe is exactly the single pulse used until now, hence the solid black line with dots in Fig. 2.22 coincides with the black line with squares in Fig. 2.16(a); thus, it represents a reference for the other bitrates. When $R = 10$ Mb/s (hence the packet is composed by ten bits), the whole DOA curve lies above the reference curve, since, in that particular realization, the number of "ones" is larger than the number of "zeros", hence the packet has larger energy, compared with the single pulse, as I verified. On the other hand, if the number of "ones" were smaller than the number of "zeros", the whole DOA curve would lie below the reference curve. As the modulation bitrate increases, the "low of large number" is such that the number of "ones" is almost coincident with the number of "zeros", hence the modulated packet has the same energy as the single pulse, as demonstrated in Fig. 2.22, by the superposition between the DOA curves for $R = 20$ Mb/s or $R = 40$ Mb/s and the reference DOA. Similar results were obtained for all the input probe SOPs

[2]Signal energy is defined,as usual, as $E_s = \int_{T_s} P_s(t)dt$.

used to obtain Fig. 2.16, confirming that what matters in LPA process, as far as the probe is concerned, are its average power and energy.

The fact that the nonlinear cross-interactions between probe and pump depend on the average probe power P_s and not on its peak power, is due to the large walk-off (in the order of the speed of light) imposed by the counter-propagation geometry. Such a result can be explained resorting to the analysis of the nonlinear cross-interactions between probe and pump, discussed in [65], in terms of a "low-pass walk-off filter". Here, the authors have proven that the cross-interactions generated by a modulated probe on a CW pump can be described as a low-pass filter, whose bandwidth is inversely proportional to the walk-off between the interacting signals. Hence, in counter-propagating regime, such a filter is so narrow as to let pass only the central frequency of the modulated probe, i.e., its DC component. In other words, the probe slides so fast with respect to the pump, that the pump cannot follow the intensity variations of the probe, but it can see only the average probe power.

Chapter 3

Co-propagating Nonlinear Lossless Polarizer

In memory of V. V. Kozlov.
We had many fruitful discussion on LPA.

As discussed in chapter 2, the original counter-propagating configuration of the nonlinear lossless polarizer (NLP) requires long (microseconds) transient time and large signals power (watts), due to the relative propagation velocity between signal and pump imposed by the geometry, that is fixed and relativistic (i.e., equal to the speed of light). As a consequence, a counter-propagating NLP can repolarize only powerful signals with a slowly-varying polarization, i.e., it is effective only on packetwise polarized signals.

In order to exploit the additional degree of freedom given by the relative propagation velocity between signal and pump, the NLP must be designed in co-propagating configuration [34, 45]. In fact, when signal and pump co-propagate, their relative propagation velocity can in turn be optimized (for given power levels), as a function of the symbol period [34]. As a consequence, a co-propagating NLP can repolarize signals with a fast-varying polarization, and can employ lower power levels.

In this chapter, I summarize numerical results regarding the design of a co-propagating NLP. First, I characterize the performance of the device as a function of the relative propagation velocity, i.e., the walk-off, between signal and pump. At the same time, I shall cast new light on the central role of walk-off in the dynamics of lossless polarization attraction, by showing that there exists an interval of walk-off values, in order to reach the *polarization attraction regime*. Moreover, I show how

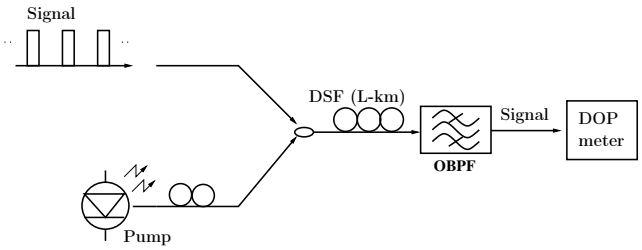

Figure 3.1: System setup of the nonlinear lossless polarizer (NLP). The NLP is composed by the fiber along with the (fully-polarized) pump laser, with power P_p, coupled with the signal at the NLP input. Signal is isolated from the pump by the optical band-pass filter (OBPF), at the NLP output.

the NLP performance degrades when the device is realized by employing an optical fiber with a large polarization mode dispersion. Finally, I introduce, for the first time to my knowledge, some early results regarding the NLP realized with two (or more) (co-polarized) pump lasers.

3.1 System setup and simulation parameters

Fig. 3.1 shows the simulated co-propagating NLP, composed by a dispersion-shifted fiber (DSF), where a fully-polarized CW pump laser, with power $P_p = s_{0p}$, is coupled with the signal, at the fiber input. The pump channel is then suppressed from the signal bandwidth by the optical band-pass filter (OBPF), at the fiber output. The fiber, with length L in the order of kilometers, is characterized by Kerr coefficient $\gamma = 1.99\,\mathrm{W^{-1}km^{-1}}$, attenuation $\alpha = 0.2$ dB/km and group velocity dispersion (GVD) parameter D = 4 ps/nm/km.

The random birefringence of the fiber was rigorously taken into account by its polarization mode dispersion (PMD) coefficient $\mathrm{D_{PMD}}$. I have considered different randomly birefringent fibers characterized by either a "small" PMD coefficient, $\mathrm{D_{PMD}} = 0.05\ \mathrm{ps/km^{1/2}}$, or a "large" PMD coefficient, $\mathrm{D_{PMD}} = 0.2\ \mathrm{ps/km^{1/2}}$, respectively. The first value is typical of low-PMD fibers manufactured in recent years, after 1999 [61], while the second values is typical of legacy fibers, i.e., of fibers installed in the mid-1990s [61]. In both cases, the system parameters are such that the nonlinear propagation of signal and pump is governed by the Manakov-PMD equation (1.18) [45]. Hence, the Kerr effect is isotropic on the Poincaré sphere and polarization attraction occurs towards any fixed pump SOP, here chosen as linear

horizontal (i.e., $\hat{s}_p = \hat{s}_1$), without loss of generality.

I assumed that the input signal consists of a single intensity-modulated pulse, with power $P_s = s_{0s}$ and limited duration T_s. Different from the case of a counter-propagating NLP (chapter 2), where the pulse duration T_s was in the order of microseconds, here I have considered pulse durations T_s in the order of the picoseconds. Moreover, I assumed that the changes in signal polarization, even if faster than those considered for the counter-propagating NLP, are in the time-scale of a few pulses, i.e., tens/hundreds of picoseconds. Thus, I injected into the fiber completely-polarized input pulses, $\overrightarrow{s}_s^{in} = s_{0s}^{in}(t)\hat{s}_s^{in}$, where $\hat{s}_s^{in}$ is constant over the whole duration T_s, and lies at an angular distance χ_{in} (on the Poincaré sphere) from the input pump SOP.

As in chapter 2, to avoid pulse-to-pulse nonlinear interactions mediated by the pump, I assumed that only one pulse travels into the NLP at a time, so that it interacts with a fresh pump portion which had not interacted with any other signal pulse before. As demonstrated in [45], such an assumption is by no way restrictive, in the evaluation of the NLP performance on an ensemble of individual (polarization-scrambled) pulses. In fact, the ensemble of scrambled input pulses takes into account all possible input SOPs and therefore is statistically equivalent to considering a single unpolarized signal beam, whose polarization varies from pulse to pulse, i.e., a *bitwise* polarized signal. To prove that, I verified that the NLP performance measured on an ensemble of input pulses, each propagating separately, exactly coincides with that obtained by propagating the pulses in a time sequence, provided that they are sufficiently spaced to avoid pulse-to-pulse interactions mediated by the pump. Actually, the term “sufficiently" can be quantified more accurately: the temporal separation between pulses in the stream should be not less than the total delay time between the signal and the pump channels cumulated over the total length of the fiber, plus the pulse duration.

The signal was placed at the fiber zero dispersion wavelength (zdw) λ_{zdw}, while the pump laser was placed at wavelength λ_p, so that pump and signal propagate at different velocities. Thus, their total walk-off delay, at the fiber output, is $T_d = \mathrm{D}\Delta\lambda L$, where the dispersion parameter D is evaluated at the pump wavelength, while $\Delta\lambda = |\lambda_p - \lambda_{zdw}|$. In simulations that follow, once fixed the fiber type and length (as well as the signal wavelength λ_{zdw}), the walk-off T_d can be tuned by varying the pump wavelength placement, hence $\Delta\lambda$, still keeping signal and pump within the conventional telecom bandwidth (C-band). During simulation, I also tested the case of zero walk-off. The limit case $T_d = 0$ may be obtained with group-velocity matched signals and pumps (e.g., placed on opposite sides of the fiber zdw) [59]. Besides this configuration, testing walk-off delays close to zero, for any specific fiber type with a given dispersion D, one should let $\Delta\lambda \simeq 0$, which is not a realistic condition, since

pump and signal spectra would overlap. Nevertheless, as far as numerical simulations are concerned, the two approaches are totally equivalent (as I verified numerically). Hence, it is only the amount of total delay T_d that determines the resulting NLP performance.

In simulation results that follow, pump and signal propagate according to their respective (Manakov-PMD) equations, each of which is implicitly expressed with respect to its own carrier frequency (see chapter 1). Thus, the four wave mixing (FWM) frequency components that arise in the outer signals bandwidths, due to nonlinearity, are neglected. As known, the power of FWM sidelobes grows at the expense of the interacting pump and signal powers, and could eventually degrade the effectiveness of the attraction process. In order to check the impact of FWM, and the its possible consequences on NLP performance degradation, I complemented the results presented in the following sections with extra numerical simulations, including the effect of FWM. To this purpose, I resorted to a full propagation model that is as general as possible, accounting for all linear and nonlinear effects relevant to the propagation of intense pulses through telecom fibers. In such a full propagation model, pump and signal are collected in a single multiplexed propagating field, with a bandwidth large enough to include FWM sidelobes. Due to such a large bandwidth, these simulations are computationally costly, hence I only performed them for the most critical values of system parameters that I have used to obtain results that follow. All simulation results confirm that the impact of FWM does not alter DOP values significantly. In order to further check that power depletion due to FWM is negligible in all tested configurations, I directly measured the FWM sidelobes. These are barely visible, in the spectra, with a FWM spectral peak that lies more than 30 dB below the spectral peak of the pump. I can then conclude that, at the power levels that I tested, there is no significant degradation of the NLP effectiveness due to FWM.

According to the discussion in Sec. 1.3.2, I quantified the performance of the NLP device by measuring the (time- and statistically-averaged) degree of polarization (DOP). The average was performed over 100 launched signal polarizations, with uniform distribution over the Poincaré sphere, so that DOP $\simeq 0$ at the NLP input. Moreover, I measured the (ensamble-)averaged degree of attraction ($\overline{\text{DOA}}$) between the output signal SOPs and the input pump polarization $\hat{s}_p$, according to (1.37). By comparing the DOP and the $\overline{\text{DOA}}$, it is possible to evaluate the angular distance between the "center of mass" of the ensamble-averaged signal SOPs and the pump SOP $\hat{s}_p$, at the NLP output. In other words, by comparing the DOP and the $\overline{\text{DOA}}$, it is possible to evaluate the angular distance between the SOP towards which the signal is attracted and the reference pump SOP (towards which the signal should be attracted).

3.2 The role of walk-off in polarization attraction

In this section, I analyze how the amount of the relative propagation velocity between signal and pump, i.e., of the signal-pump walk-off, affects the nonlinear interaction between them, hence how it affects the effectiveness of lossless polarization attraction.

3.2.1 Optimal pump wavelength placement

As a first step, in this section I concentrate my attention in studying the dependence of the NLP performance on the total walk-off delay, T_d, between signal and pump. To this aim, for the moment I have fixed the amount of the nonlinear Kerr interaction between the signals. Thus I have simulated the system setup described in Sec. 3.1, where the NLP is composed by a low-PMD fiber ($D_{PMD} = 0.05$ ps/km$^{1/2}$) with length $L = 20$ km. In such a case, as demonstrated in Sec. 3.5, the linear PMD effects are negligible, hence the signal is attracted towards the input pump polarization, $\hat{s}_p = \hat{s}_1$, and $\overline{DOA} = DOP$, at the NLP output. Moreover, to demonstrate the power efficiency of the co-propagating NLP, I kept the overall optical power at moderate levels, compared with the power needed in a counter-propagating NLP, and chose the same signal and pump peak power $P_s = P_p = 200$ mW. Different values for both fiber length and signals power will be employed in Sec. 3.3.

Fig. 3.2(a) shows the NLP performance, quantified by the output signal DOP, as a function of the total walk-off delay T_d between signal and pump. Here, I varied $\Delta\lambda$ from 0 to 20 nm (by varying the pump wavelength λ_p), so that T_d varies between 0 and 1600 ps. Different plots are obtained for signal pulses with different durations T_s, equal to $T_s = 1000$ ps, $T_s = 400$ ps, $T_s = 100$ ps, and $T_s = 10$ ps. Thus, different plots represents the NLP performance as obtained for signals characterized by a polarization coherence time ranging from a single bit, modulated at a bitrate $R = 100$ Gb/s ($T_s = 10$ ps), to few bits, modulated at a bitrate $R = 10$ Gb/s. For all tested values of T_s, the high DOP reached, close to 0.8, demonstrates how the transient time of the LPA process, stimulated employing a co-propagating pump, can be decreased by many order of magnitude (from μs to ps), with respect to the transient time of the counter-propagating LPA.

In particular, Fig. 3.2(a) shows that an optimal total walk-off delay T_d^*, hence an optimal pump wavelength λ_p^*, exists, that maximizes the performance of the attraction phenomenon, for each tested pulse duration. While such an optimal T_d^* (and the whole plot) depends on the signal pulse duration T_s, it is remarkable that the best DOP value is independent of it, being $DOP^* \cong 0.78$ for all the tested pulses. Moreover,

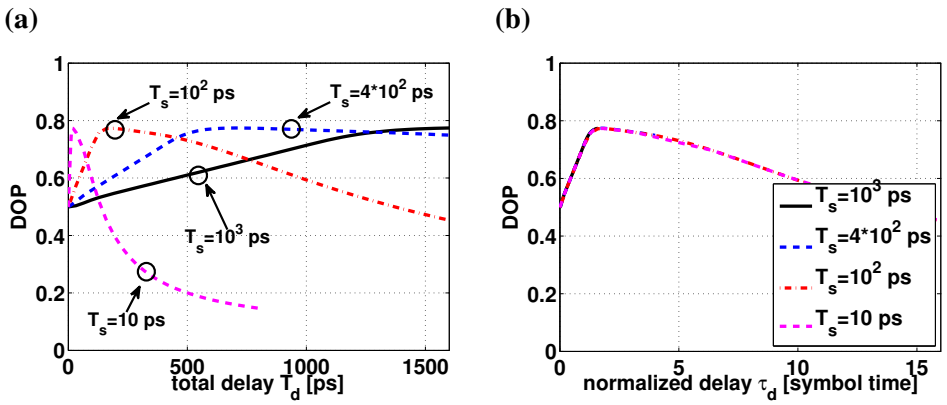

Figure 3.2: Performance of a co-propagating nonlinear lossless polarizer (NLP): output signal degree of polarization (DOP) versus the total pump-signal walk-off delay T_d. Results obtained for different pulse durations T_s (a) obey a scaling law, so that DOP only depends on the normalized delay $\tau_d \triangleq T_d/T_s$ (b).

T_d^* increases with the pulse duration T_s, meaning that the effectiveness of LPA fades away, i.e., DOP drops below DOP*, whenever the walk-off delay T_d is too large or too small, compared with the duration of the pulse to be attracted.

The above results suggest that a scaling rule exists. This is indeed verified in Fig. 3.2(b), where the obtained DOP values are plotted versus the total walk-off delay normalized to the pulse duration, hence $\tau_d \triangleq T_d/T_s$. Thus, each curve in Fig. 3.2(a) can be obtained by rescaling the single curve, visible in Fig. 3.2(b), which summarizes the performance of LPA for any pulse duration, at the chosen power level. Hence, curve in Fig. 3.2(b) represents one of the most important results concerning the co-propagating NLP performance, since it demonstrates that **the transient time of LPA can be adapted to any polarization coherence time of the signal**, and it gives the rule to control the LPA transients by properly selecting the pump wavelength. Moreover, as shown in Sec. 3.3, such a curve reaches larger DOP values, by increasing the amount of the nonlinear Kerr interaction between signal and pump (e.g., by increasing signals power). Note that the value of the optimal normalized walk-off delay is $\tau_d^* \cong 1.75$ and depends on the signals power; for different power levels, τ_d^* changes, as shown in Sec 3.3. Furthermore, note that $\tau_d^* \cong 1.75$ is the value that maximize the DOP, evaluated as the ensamble-average over the pulse SOPs. Considering a single input pulse polarization, for each SOP value, a different value τ_d that optimizes the NLP performance exists. Anyway, It seems that a functional relation describing the

optimal normalized walk-off as a function of the input signal SOP does not exists, since the plot of the optimal τ_d versus signal SOP (not reported here) is apparently chaotic.

The scaling rule, just verified numerically, should not surprise, since it can be obtained analytically. The motion equations system (1.30), reported in chapter (1) and recalled here, is

$$\begin{cases} \frac{\partial \overrightarrow{s}_s(z,t)}{\partial z} + \frac{1}{2v_{wo}} \frac{\partial \overrightarrow{s}_s(z,t)}{\partial t} = & \frac{8}{9}\gamma e^{-\alpha z}\left[\overrightarrow{s}_p(z,t) \times \overrightarrow{s}_s(z,t)\right] \\ \frac{\partial \overrightarrow{s}_p(z,t)}{\partial z} - \frac{1}{2v_{wo}} \frac{\partial \overrightarrow{s}_p(z,t)}{\partial t} = & \frac{8}{9}\gamma e^{-\alpha z}\left[\overrightarrow{s}_s(z,t) \times \overrightarrow{s}_p(z,t)\right] \end{cases}, \tag{3.1}$$

where $\overrightarrow{s}_i$ (for $i = s, p$) represent signal (s) and pump (p) Stokes vectors, while v_{wo} is the walk-off speed (see Sec. 1.2.3, chapter 1). Suppose I make the change of time scale $\tau = t/T$, so that $\overrightarrow{s}'_s(z,\tau) = \overrightarrow{s}_s(z,t/T)$ is a compressed version (if $0 < T < 1$) of the signal pulse. It is easy to show that $\overrightarrow{s}'_s(z,\tau)$ and $\overrightarrow{s}'_p(z,\tau) = \overrightarrow{s}_p(z,t/T)$ obey a set of equations identical to (3.1), provided that the walk-off speed v_{wo} is changed into $v'_{wo} = T \cdot v_{wo}$. Hence, in the new reference time-frame, τ, system (3.1) becomes

$$\begin{cases} \frac{\partial \overrightarrow{s}'_s(z,\tau)}{\partial z} + \frac{1}{2v'_{wo}} \frac{\partial \overrightarrow{s}'_s(z,\tau)}{\partial \tau} = & \frac{8}{9}\gamma e^{-\alpha z}\left[\overrightarrow{s}'_p(z,\tau) \times \overrightarrow{s}'_s(z,\tau)\right] \\ \frac{\partial \overrightarrow{s}'_p(z,\tau)}{\partial z} - \frac{1}{2v'_{wo}} \frac{\partial \overrightarrow{s}'_p(z,\tau)}{\partial \tau} = & \frac{8}{9}\gamma e^{-\alpha z}\left[\overrightarrow{s}'_s(z,\tau) \times \overrightarrow{s}'_p(z,\tau)\right] \end{cases}, \tag{3.2}$$

implying that the signals evolution is the same as that got by solving (3.1), for a rescaled walk-off speed v'_{wo}, hence for a rescaled delay $\tau'_d = L/v'_{wo} = T_d/T$. As a consequence, if I choose the time-scaling factor equal to the pulse duration, i.e., $T = T_s$, all the curves in Fig. 3.2(a) coincide, as demonstrated in Fig. 3.2(b).

The practical implication of the obtained result is that, given the NLP parameters and the pulse duration, the optimal $T_d^* \cong 1.75 \cdot T_s$ can be reached by placing the pump at an optimal wavelength distance $\Delta\lambda^* = T_d^*/(\mathrm{D} \cdot L)$ from the signal. On the contrary, for a given pump wavelength, hence a fixed $\Delta\lambda$ (and T_d), an optimal pulse duration $T_s^* \cong T_d/1.75$ exists, for which the effectiveness of the NLP device is maximized. In any case, polarization attraction effectively occurs only for a limited range of walk-off delays; e.g., in the present case of system parameters, results in Fig. 3.2(b) show that $T_s < T_d < 6T_s$ is required, in order to get DOP > 0.7. Such a range, represents a sort of "polarization attraction interval", within which LPA could be considered effective.

3.2.2 Polarization rotation and polarization attraction regimes

As a matter of fact, polarization attraction is the joint effect of the Kerr nonlinearity and the relative propagation speed, both occurring between pump and signal, in

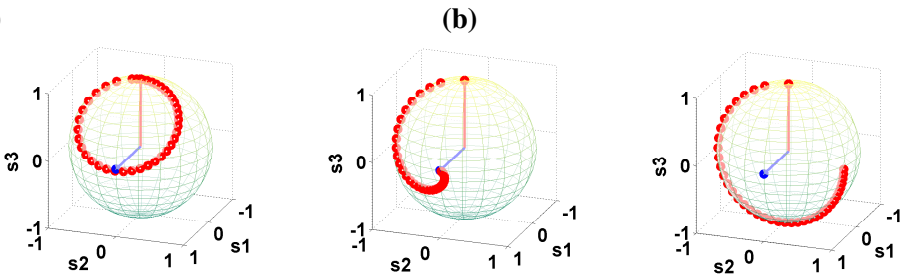

Figure 3.3: Evolution of the average signal SOP along the NLP. Here, the input signal and pump SOPs are right-circular ($\hat{s}_3$) and linear-horizontal ($\hat{s}_1$), respectively (as remarked by the red and blue vectors in figure). A too small (a, $T_d = 0$) or too large (c, $T_d = 32 \cdot T_s$) walk-off induces polarization rotation, while polarization attraction is effective for intermediate values (b, $T_d = 5 \cdot T_s$).

carefully balanced amounts. Fig. 3.3, obtained with the same system parameters used in previous section, shows an exemplification of this assertion. The plots in Fig. 3.3 show the evolution of the signal polarization along the fiber whit which the NLP is realized. Each (red) circle is the time-averaged SOP of the signal pulse, at a given position $0 \leq z \leq L$, i.e., it represents the direction $\hat{m}_s$ of $\left\langle \overrightarrow{s}_s(z,t) \right\rangle$ (see Sec. 1.3.1, chapter 1). As an example, Fig. 3.3 was obtained by injecting into the fiber a right-circular polarized signal and a linear-horizontal polarized pump. Thus, the input signal SOP is $\hat{s}_s = \hat{s}_3$ (red vector in figure), while the input pump SOP is $\hat{s}_p = \hat{s}_1$ (blue vector in figure), so that the angular distance between the input signal Stokes vectors is $\chi_{in} = 90°$ (on the Poincaré sphere). The three plots correspond to different values of the walk-off delay T_d, equal to zero (a), $5 \cdot T_s$ (b), and $32 \cdot T_s$ (c).

As clearly shown in Fig. 3.3, the average signal SOP, starting at $\hat{s}_3$, moves towards the pump SOP $\hat{s}_1$, hence evolves according to a *polarization attraction regime*, only for the intermediate case. On the contrary, the signal SOP keeps rotating in a circle, i.e., undergoes a *polarization rotation regime*, in the other two cases. Such a behavior, that I regularly observed for any input signal SOP, can be simply explained, in the case $T_d = 0$ (Fig. 3.3(a)). In fact, as discussed in Sec. 1.2.3, chapter 1, in the absence of walk-off, both pump and signal SOPs evolve, along the fiber, according to a "carousel model" [60]. Thus, they rotate around a fixed pivot vector ($\overrightarrow{m}$) equal to their vector sum, hence located middle way between $\hat{s}_3$ and $\hat{s}_1$, in the present case of equal pump and signal power. The circle thus described by the average signal SOP (red dots in figure), as seen in Fig. 3.3(a), can even become aligned with the pump

SOP ($\hat{s}_1$), for certain values of the coordinate z and/or power, but still in a *polarization rotation regime*, and not in the *polarization attraction regime*. As I show in Sec. 3.4, where more details about the co-propagating NLP operating in the *polarization rotation regime* (with $T_d = 0$) will be given, the trajectory of the signal SOP is subject to change with length, power and input SOP. The other extreme case of very large walk-off, shown in Fig. 3.3(c), can be equally well explained with the rotation of the average signal SOP around the input pump SOP, as dictated by the equation that governs the signal SOP evolution (3.1). This case differs from the zero walk-off case since, in the limit, it is as if the signal pulse were infinitely short, hence is unable to perturb the pump polarization (through the equation that governs the pump SOP evolution), so that $\overrightarrow{s}_p$ is roughly constant.

Hence, the two *polarization rotation regimes* can be explained theoretically and never result in a stable polarization attraction, since the signal SOP evolves in circles (although an illusory attraction can occur, in the first case, for specific NLP parameters, as shown in Sec. 3.4). An effective *polarization attraction regime* is reached, instead, for intermediate values of the walk-off, close to the optimal T_d, that depends on the duration of the pulse to be attracted. With the input signal SOPs chosen here, as an example, the optimal walk-off is $T_d = 5 \cdot T_s$ (which is different from $T_d^* = 1.75$, as obtained for an ensamble-averaged signal SOPs). In this case, the time-averaged signal SOP follows a spiral trajectory, as in Fig. 3.3(b), leading towards the input pump SOP, at the NLP output. Such a spiral trajectory, already seen for the counter-propagating NLP (Fig. 2.10, in chapter 2), results here closer to the input pump SOP, compared with that obtained with the counter-propagating NLP, due to the optimized balance between the XpolM effect and the walk-off delay.

To give a more intuitive picture of the different behavior of the NLP operating in polarization rotation or polarization attraction regimes, Fig. 3.4 shows the LPA effectiveness as a function of the fiber length L. Since I fixed here the input signal SOPs ($\hat{s}_s = \hat{s}_3$ and $\hat{s}_p = \hat{s}_1$, the same as those used to obtain Fig. 3.3), I quantified LPA effectiveness by measuring the DOA between the output signal SOP and the input pump SOP, according to equation (1.34). To obtain Fig. 3.4, I fixed the wavelength displacement value $\Delta\lambda$ so that the normalized walk-off delay τ_d is either zero (solid line with circles), close to the optimal value τ_d^* (dashed-dot line with squares) or very large compared with the optimal value (dashed line with diamonds), for every fiber length employed. As can be clearly seen in Fig. 3.4, the NLP shows a stable behavior and an appreciable performance (DOA = 0.8) only when it works in the polarization attraction regime, hence for τ_d within the "polarization attraction interval" ($\tau_d \cong \tau_d^*$). In such a regime, once LPA has reached its maximum effectiveness,

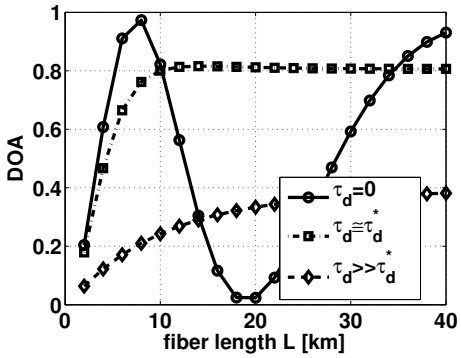

Figure 3.4: Degree of attraction (DOA) versus fiber length. Here, the input signal and pump SOPs are right-circular ($\hat{s}_3$) and linear-horizontal ($\hat{s}_1$), respectively. The NLP shows a stable behavior and appreciable performance only when it works in polarization attraction regimes, hence when $\tau_d \cong \tau_d^*$. Instead, when NLP works in polarization rotation regime, its performance is poor ($\tau_d \gg \tau_d^*$) or unstable ($\tau_d = 0$).

around $L = 10$ km in this example, the DOA remains almost constant by increasing the fiber length, meaning that the output signal SOP remains locked to the attracting pump SOP (which is consistent with the spiral trajectory in Fig. 3.3). For the system parameters used here, the behavior of the NLP seems to be stable also when its works in the polarization rotation regime with $\tau_d \gg \tau_d^*$, even if LPA shows poor effectiveness (DOA < 0.4). This happens here because the walk-off experienced by the signals is not sufficiently large, hence the NLP works on the (right) extrema of the polarization attraction interval, and not in a pure polarization rotation regime. In other words, the SOP trajectory, similar to that in Fig. 3.3(c), is not exactly a circle but rather a "very large spiral", whose points slowly get closer to $\hat{s}_p$, thus showing a small amount of attraction. With larger walk-off, the dashed line with diamonds would appear constant and close to 0 (in the present case where $\chi_{in} = 90^\circ$). On the contrary, when the NLP works in polarization rotation regime with $\tau_d = 0$, it shows an unstable behavior, since the DOA oscillates between 0 and 1 (in the present case where $\chi_{in} = 90^\circ$), due to the circular trajectory followed by the signal SOP (see Fig. 3.3(a)). As already stated, with $\tau_d = 0$ an illusory attraction could be obtained, for some particular parameters of the NLP: in the present example, a fiber with length in between 5 and 10 km or in between 35 and 40 km produces a DOA > 0.8 (with $L = 8$ km, DOA $\cong 1$, indicating an ideal attraction). More details about the design rules of a NLP operating in polarization rotation regime (with $\tau_d = 0$) will be given

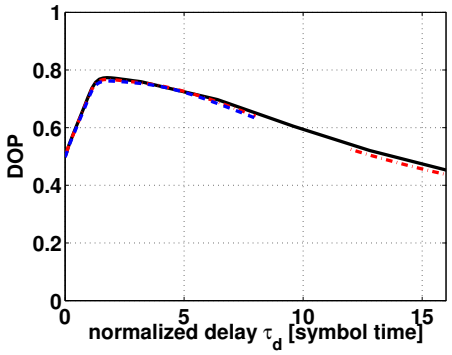

Figure 3.5: Performance of a co-propagating nonlinear lossless polarizer (NLP): output signal degree of polarization (DOP) versus the normalized walk-off delay τ_d. Different curves are obtained for different fiber length and signals power, still keeping the product $P_s L_{eff} = P_p L_{eff}$ constant.

in Sec. 3.4.

3.3 NLP in polarization attraction regime

Until now, I concentrated my attention only on the role of the walk-off in LPA, thus I kept fix the amount of nonlinear interaction between the signals. In this section, I study how the polarization attraction regime changes by changing the strength of the Kerr-induced polarization interaction (XpolM). As for a counter-propagating NLP presented in chapter 2, I quantify the strength of the nonlinear Kerr interaction through the nonlinear phase $\phi_{NL} = \gamma P L_{eff}$, where L_{eff} is the effective fiber length. For a counter-propagating NLP I demonstrated that a direct relationship between LPA performance and ϕ_{NL} does not hold (see Sec 2.3.2, chapter 2). Anyway, I demonstrate here that it is not the case for the co-propagating NLP.

Fig. 3.5, obtained by simulating the co-propagating NLP described in Sec. 3.1, shows the dependence of the output signal DOP on the normalized walk-off delay τ_d, as obtained by keeping fixed the nonlinear phase value ϕ_{NL}. To this aim, I varied both the fiber length (hence the effective length) and the signals power, still keeping constant the value of ϕ_{NL}. As a reference, I have chosen a nonlinear phase value equal to that used to obtain Fig. 3.2(b), where $L = 20$ km and $P_s = P_p = 200$ mW, reported in Fig. 3.5 with the solid (black) line. In particular, the other two curves in Fig. 3.5

were obtained with $L = 10$ km and $P_s = P_p = 325$ mW (dashed blue line), or with $L = 5$ km and $P_s = P_p = 578$ mW (dot-dashed red line). Since all curves in Fig. 3.5 overlap each other, it is demonstrated that, in co-propagating configuration, there is a direct relationship between LPA performance and $\phi_{NL} = \gamma P L_{eff}$, where P represents the signals power $P_s = P_p$. The same relationship holds also for different values of the nonlinear phase, as I numerically verified.

By following the framework used to present the performance of a counter-propagating NLP in chapter 2, I concentrate now on the dependence of LPA effectiveness on the signals power only, to understand if LPA is still a function of the signals power product, hence P could be considered the geometrical mean of signal and pump power $(P_s P_p)^{1/2}$. Fig. 3.6, which shows the contour plot of the DOA as a function of both signal (P_s) and pump (P_p) power, demonstrates that it is not the case for a co-propagating NLP. In particular, in Fig. 3.6 I fixed the fiber length $L = 20$ km and the input signals SOPs as right-circular for the signal ($\hat{s}_s = \hat{s}_3$) and linear-horizontal for the pump ($\hat{s}_p = \hat{s}_1$), so that $\chi_{in} = 90^{\circ}$. The three contour plots correspond to three values of the normalized walk-off τ_d equal to 0, 5 and 10. As evident, for no one of the three plots in Fig. 3.6 the contours overlap with equilateral hyperbolae, meaning that LPA performance, in co-propagating configuration, is not a function of the signals power product, at least for the normalized walk-off values tested here. This is true for any other input signal SOP (hence, for any other χ_{in}), as I numerically verified.

Getting back to Fig. 3.5, results above mean that the curves reported in the figure coincide because it is the products $P_s L_{eff}$ and $P_p L_{eff}$ that are kept constant. In other words, for a co-propagating NLP, the effectiveness of LPA as a function of the normalized walk-off τ_d does not change by maintaining fixed and equal to each other the strength of the nonlinearity acting on the signal, proportional to $P_s L_{eff}$, and on the pump, proportional to $P_p L_{eff}$, at least for the normalized walk-off values tested here.

Together, results reported in this section appear to be in contrast with those reported in chapter 2, for a counter-propagating NLP. In fact, for a counter-propagating NLP, the effectiveness of LPA depends on $P = (P_s P_p)^{1/2}$, while it does not show a direct relation with ϕ_{NL}. Indeed, by increasing the normalized walk-off τ_d, the DOP values obtained for different values of fiber length and signals power, still keeping $P_s L_{eff} = P_p L_{eff}$ constant, are no longer coinciding, as verified in the right edge of Fig. 3.5. Moreover, the contour levels of the DOA, in a plot similar to Fig. 3.6 corresponding to a large τ_d, tend to become equilateral hyperbolae, as I numerically verified (e.g., with $\tau_d = 64$). Thus, there is a physical continuity in the results, further confirming that the counter-propagating configuration is the limit case ($\tau_d \to \infty$) of the co-propagating one: by increasing τ_d in a co-propagating NLP, hence by moving

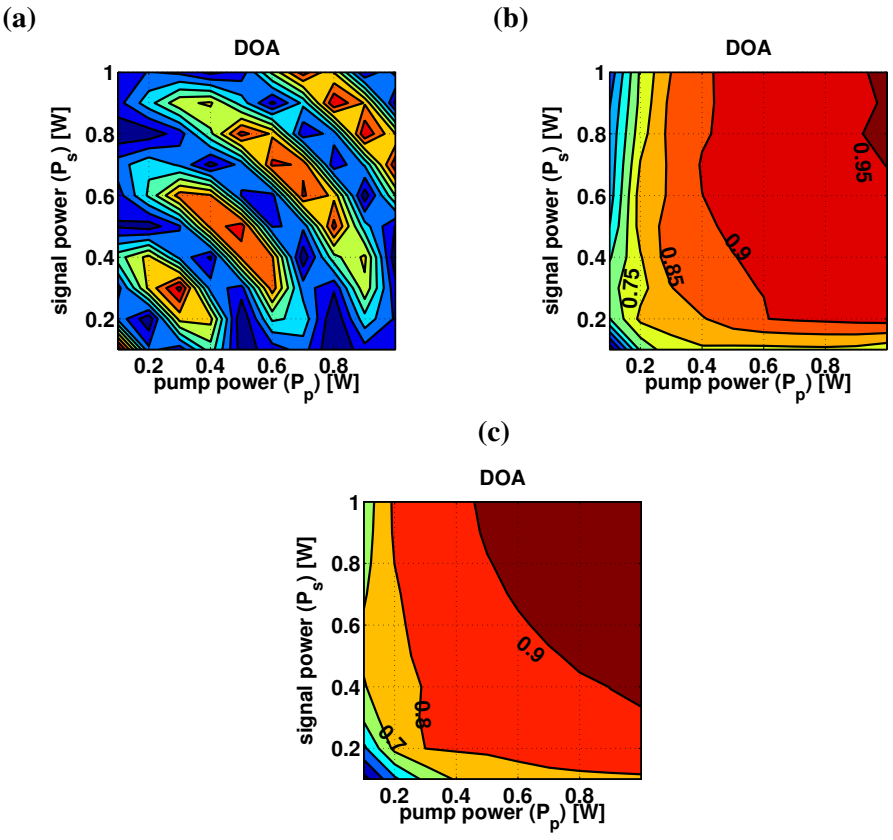

Figure 3.6: Degree of attraction (DOA) as a function of signal and pump powers, for different values of the normalized walk-off τ_d equal to 0 (a), 5 (b) and 10 (c). The fiber length is $L = 20$ km, while the angular distance between the input signals Stokes vector is $\chi_{in} = 90°$ (on the Poincaré sphere).

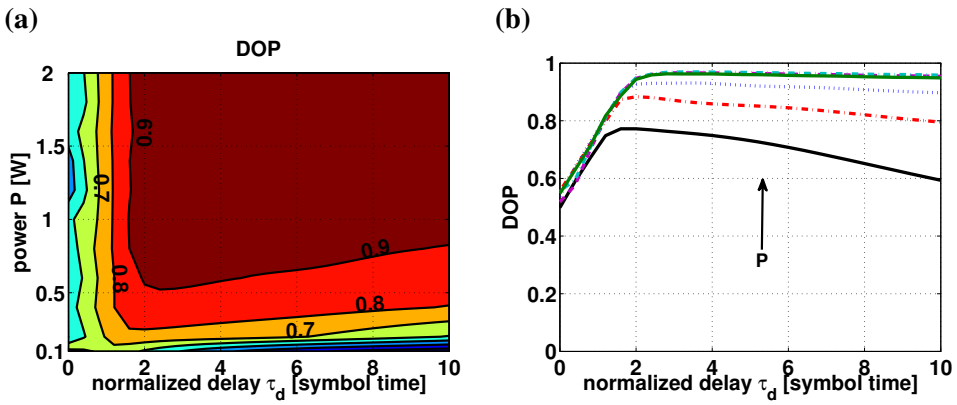

Figure 3.7: Performance of a co-propagating nonlinear lossless polarizer (NLP). (a) Output signal degree of polarization (DOP) versus the signals power ($P_s = P_p$) and the normalized walk-off delay τ_d. (b) DOP versus τ_d for different values of the signals power equal to 0.2, 0.4, 0.8, 1.6, 1.8 and 2 W.

towards a "counter-propagating like" NLP, I found the same behavior I got with a counter-propagating NLP.

Until now, I have considered only one value for the nonlinear phases ϕ_{NL}, used to obtain both Figs. 3.2 and 3.5. In the following, I am going to show what happens to the curve representing the DOP versus τ_d when the strength of the nonlinearity increases. In particular, I am going to show how polarization rotation and polarization attraction regimes change. To this aim, I have fixed the fiber length $L = 20$ km, while I have varied the strength of the nonlinearity by varying the signals power, P_s and P_p, still keeping equal levels $P_s = P_p = P$. Fig. 3.7(a) shows the contour plot of the output signal DOP obtained by varying the normalized walk-off delay τ_d and power P. Fig. 3.7(a) show how, with a co-propagating NLP, a DOP larger than 0.8 could be obtained with power larger than 200 mW, while the DOP increases more than 0.9 for power larger than 500 mW (for an optimized delay). Anyway, by increasing the power, hence the amount of nonlinearity, even more, the optimal walk-off, is always about two times the signal durations T_s, as demonstrated by the contour levels in Fig. 3.7(a), which are vertical straight lines for $1 < \tau_d < 2$. Such a behavior is evident in Fig. 3.7(b), where the curves representing the DOP versus τ_d is plotted for different values of the signals power, equal to 0.2, 0.4, 0.8, 1.6, 1.8 and 2 W. Hence, each curve in Fig. 3.7(b) represents an horizontal section of the contour plot in Fig. 3.7(a). For normalized walk-off smaller than the optimal walk-off τ_d^* (left side

of the plot) all curves appear overlapped, by increasing the signals power. For normalized walk-off larger than τ_d^* (right side of the plot), the performance of the NLP increases, by increasing the signals power, and tends to flatten, as a function of τ_d. Such a behavior indicates that the region of walk-off where the co-propagating NLP works in the polarization attraction regime widens, hence the "polarization attraction interval" increases by increasing the signals power (hence, the Kerr nonlinearity). Despite the values of normalized walk-off tested here, in between 0 and 10, are very small with respect to the walk-off given by the counter-propagating geometry, **such a result explains why a counter-propagating NLP is effective only on long powerful signals**. The high signals power is needed to enlarge the "polarization attraction interval", while the long (microseconds) signal durations are needed to make the walk-off fall within the polarization attraction interval. For signals whose duration is shorter than a microsecond, the counter-propagating NLP works in polarization rotation regime, where the signal Stokes vector rotates around the pump Stokes vector, as depicted in Fig. 3.3(c). Moreover, for powers larger than 1.6 W, the curves in Fig. 3.7(b) almost overlap each other, demonstrating that a further increase of the signals power would not lead to a further enhancement of the NLP performance, in terms of both the reached DOP and "polarization attraction interval". Such a result is in agreement with the results obtained in chapter 2 for a counter-propagating NLP, where the average DOA ($\overline{\text{DOA}}$) seems to saturate for powers $P \geq 1.6$ W (see Fig. 2.18, in chapter 2). Thus, a further increase of the signals power would not lead to a further increase of the "polarization attraction interval", hence the transient time of the counter-propagating NLP cannot be reduced below the microsecond limit.

As a further comment on Fig. 3.7(b), note that each curve can be approximated by two straight lines that cross each other: one approximating the DOP curve in the region $\tau_d < \tau_d^*$, while the other approximating the DOP in the region $\tau_d > \tau_d^*$. The first straight line can be considered independent of the signals power, while the second straight line strongly depends on the power. By increasing signals power the slope of the straight line decreases towards zero, while its level increases towards 1.

Results in Fig. 3.7 were obtained by varying both signal and pump powers, $P_s = P_p$, still keeping them equal to each other. In a practical application, the power of the signal transmitted through an optical network is typically in the order of few tens of milliwatts. Hence, having signals with power larger then few hundred of milliwatts, at the input of the NLP, could be difficult, since this requires a powerful amplifier placed at the device input. On the other hand, the pump power injected into the NLP could be controlled more freely, by appropriately selecting the laser to be employed. Thus, I have performed numerical simulations of the co-propagating NLP, where the signal

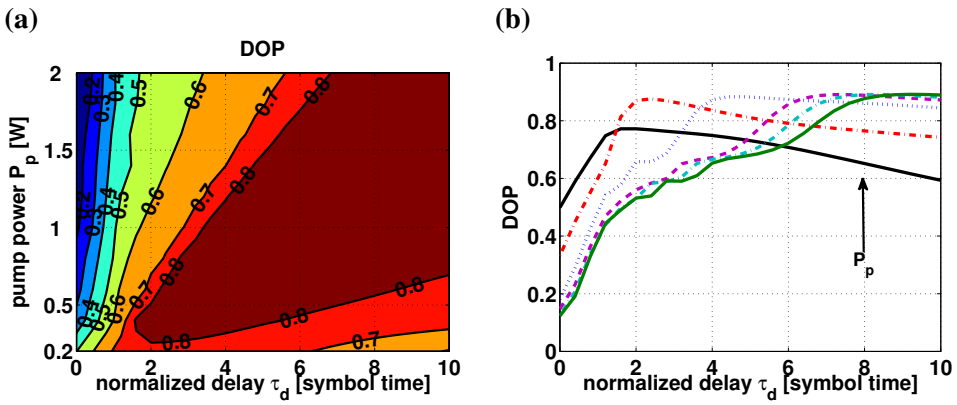

Figure 3.8: Performance of a co-propagating nonlinear lossless polarizer (NLP). (a) Output signal degree of polarization (DOP) versus the pump power (P_p) and the normalized walk-off delay τ_d. (b) DOP versus τ_d for different values of the pump power equal to 0.2, 0.4, 0.8, 1.6, 1.8 and 2 W. The signal power is $P_s = 200$ mW.

power is fixed to $P_s = 200$ mW, while the pump power P_p varies between 200 mW and 2 W. Results are reported in Fig. 3.8, where the DOP of the output signal is plotted as a function of the pump power and of the normalized walk-off (τ_d) between the signals, as a contour plot (a) or parametrized curves (b), for a fiber with length $L = 20$ km. As opposed to the case where both signals powers vary (Fig. 3.7) (where the optimal walk-off remains $\tau_d \cong 2T_s$ despite the increase of signals power), Fig. 3.8 shows how the optimal walk-off increases by increasing the pump power, when the signal power is fixed. Hence, the more powerful pump is employed and the more sliding between signal and pump is needed to optimize the performance of the NLP device. Anyway, both the best output signal DOP and the "polarization attraction interval" increase by increasing the pump power, similar to the results shown in Fig. 3.7. Moreover, Fig. 3.8(b) shows that for the largest tested pump power levels, the best values obtained for the output signal DOP seems to saturate, as happens also in Fig. 3.7.

Such a behavior appears clear in Fig. 3.9, which compares the best value of the output signal DOP as a function of the pump power P_p, when the signal power changes with the pump power ($P_s = P_p$, solid line with squares) or is kept fixed ($P_s = 200$ mW, dashed line with circles). These curves thus report the maxima of each set of curves shown in Fig. 3.7(b) and Fig. 3.8(b), respectively. In Fig. 3.9, each value of the signal DOP was obtained by designing the NLP so that it operates at the

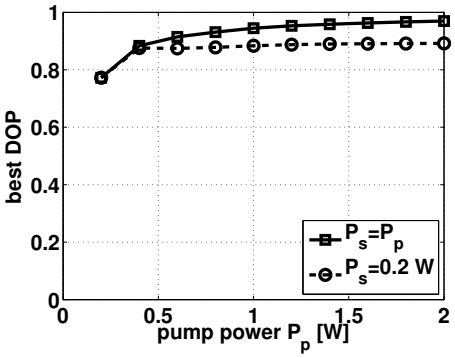

Figure 3.9: Best performance of the NLP as a function of the pump power. Maximum signal DOP obtainable when the signal power changes with the pump power ($P_s = P_p$) or is kept fixed ($P_s = 200$ mW). Each value of the DOP was obtained by designing the NLP so that it operates at the optimal walk-off τ_d^*.

optimal walk-off τ_d^*, for any pump power tested. As stated previously, the best DOP reached at the output of the NLP seems to saturate to a value that is DOP $= 0.9$, when the signal power is fixed, or DOP $= 0.97$ when both signal and pump powers change. Although the overall power ($P_p + P_s$) injected into the NLP in the case of fixed signal power (2.2 W, in the right edge of Fig. 3.9) is much lower than that injected in the case when both powers change (4 W), the best DOP reached in the two cases are close to each other.

3.3.1 Further considerations

Until now, all results presented in this chapter were obtained by assuming that the signal pulses are sufficiently spaced to avoid pulse-to-pulse nonlinear interactions mediated by the pump, which could significantly degrade the performance of the NLP (as shown in chapter 2, Sec. 2.3.6). As stated in Sec. 3.1, the term "sufficiently" means that the temporal separation between signal pulses in the stream should be not less than the total delay time between the signal and the pump channels cumulated over the total fiber length, plus the pulse duration. By referring to a legacy on-off keying (OOK) modulation for the signal, in order to introduce a guard interval between two consecutive pulses a return-to-zero (RZ-OOK) format could be employed. Moreover, as demonstrated in Sec. 3.3, the performance of a co-propagating NLP is maximized when the total walk-off delay T_d between signal and pump is roughly

twice the signal pulse duration T_s (see, e.g., Fig. 3.7). In order to satisfy both conditions above, the duty-cycle of the RZ-OOK should be 33%. In fact, by considering a modulation bit-rate $R = 1/T_b$, where T_b is the bit-period, each bit of the signal would be encoded on a pulse with duration $T_s = 0.33T_b$, and a nearly optimal walk-off $T_d \cong 2T_s = 0.66T_b$ could be reached by properly selecting the pump wavelength. Furthermore, $T_d + T_s \cong 0.99T_b$ would be less then the bit-period T_b, which guarantees the absence of nonlinear pulse-to-pulse interactions mediated by the pump. Considerations above have been used in chapter 4, where I have injected into the NLP a (bitwise polarized) input signal with 33% RZ-OOK. This is no longer true when the duty-cycle of the RZ-OOK modulation increases or the optimal walk-off grows above twice the pulse duration (as, e.g., in Fig. 3.8), since the conditions for the simultaneous achievement of an optimal walk-off and a proper guard interval between adjacent pulses cannot be satisfied.

Regarding the duty-cycle, the limiting case is that of a 100% duty cycle, i.e., of a NRZ-OOK modulated signal: since there is no guard interval between adjacent pulses, the walk-off delay should be zero, hence signal and pump should propagate at the same speed, within the NLP. Under this condition, the co-propagating NLP works in the *polarization rotation regime*, where signal and pump SOPs evolve along circles, on the Poincaré sphere, as opposed to the *polarization attraction regime* where, due to the mutual sliding between pump and signal given by the walk-off, signal SOP follows a spiral trajectory that collapses onto the input pump SOP. Co-propagating NLPs operating in the polarization rotation regime have already been shown to have poor repolarization performance [59], compared with those operating in the polarization attraction regime, i.e., with a proper walk-off. In Sec. 3.4, I propose a design rule for setting the pump power in order to improve the performance of the NLP operating in the polarization rotation regime. Anyway, such a rule requires the optimization of the pump power for each SOP that the signal takes at the input of the device; hence, it could be hard to implement in practice. Let me remark, anyway, that this is an extreme scenario, where NRZ pulses appear in a "bitwise polarized" stream, hence with an abrupt change of their SOP, from one pulse to the next. Thus, if an NRZ signal is to be controlled, that is packetwise polarized and long enough, the counter-propagating NLP, analyzed in chapter 2, would remain the most effective solution.

Regarding the case where the optimal walk-off amounts to several times the pulse duration, as happens in Fig. 3.8, a possible solution to avoid pulse-to-pulse interaction mediated by the pump could be to insert the NLP device in a loop. The NLP could be designed so that the delay between signal and pump channels, cumulated in a single passage, guarantees the absence of pulse-to-pulse interaction. Then, at the

output of the device, the distorted pump is filtered out from the signal bandwidth, while the signal is re-injected at the NLP input, so as to interact with an undistorted pump portion, thus avoiding pulse-to-pulse interaction. If the sum of all the delays between signal and pump cumulated in each loop is equal to the optimal walk-off delay required by the signal, the performance of the NLP is optimized, hence the output signal DOP is maximized. Anyway, I have not investigated, during my Ph.D., on the implementation of a NLP within a loop, that is left to further investigations.

3.4 NLP in polarization rotation regime

In Sec. 3.2.2, I have shown that, depending on the amount of the signal-pump (normalized) walk-off delay, the NLP can operate either in polarization attraction regime or in polarization rotation regime. While polarization attraction regime occurs for a limited range of walk-off values within the "polarization attraction interval", polarization rotation regime occurs either with very large or zero walk-off. As demonstrated in Sec. 3.2.2, an illusory attraction could be obtained, for some particular parameters of the NLP (signals power and fiber length), in polarization rotation regime with zero walk-off. In this section, I concentrate my attention on the NLP operating in the polarization rotation regime (with zero walk-off) and design its parameters so as to obtain an effective repolarization of the signal. The first, and only to my knowledge, results regarding the NLP operating in such a regime have shown poor repolarization performance [59]. Here, I explain why the NLP performance obtained in [59] were poor and introduce a setting rule for the pump power to improve it. Moreover, I give a closed-form solution for the degree of attraction of the signal output from the NLP, valid in the case of zero walk-off delay between signal and pump, and I exploit such a solution to obtain an approximate formula for the optimal pump power value.

3.4.1 Pump power optimization: numerical approach

I considered the system setup in Fig. 3.1, where pump and signal, both assumed to be CW for the moment, (co-)propagate, at the same velocity into the fiber. By neglecting the group velocity dispersion (GVD), the evolution of the signals Stokes vectors (on the Poincaré sphere) is governed by the system of motion equations (1.26), discussed in chapter 1, and recalled here

$$\begin{cases} \frac{\partial \overrightarrow{s}_s(z)}{\partial z} = & \frac{8}{9}\gamma \mathrm{e}^{-\alpha z}\left[\overrightarrow{s}_p(z) \times \overrightarrow{s}_s(z)\right] \\ \frac{\partial \overrightarrow{s}_p(z)}{\partial z} = & \frac{8}{9}\gamma \mathrm{e}^{-\alpha z}\left[\overrightarrow{s}_s(z) \times \overrightarrow{s}_p(z)\right] \end{cases}, \tag{3.3}$$

where $\overrightarrow{s}_i(z) = s_{0i}(z)\hat{s}_i(z)$ $(i = s, p)$, represents the signal (s) or the pump (p).

As discussed in Sec. 1.2.3, system (3.3) describes the Stokes vectors $\overrightarrow{s}_s$ and $\overrightarrow{s}_p$ rotate around the time- and z-independent pivot vector $\overrightarrow{m} = m_o\hat{m} = \overrightarrow{s}_s(0) + \overrightarrow{s}_p(0)$ by an angle $\phi_{NL}(z) = \frac{8}{9}\gamma m_0 L_{eff}(z)$. I recall that the pivot magnitude $m_0 = \sqrt{s_{0s}^2 + s_{0p}^2 + 2s_{0s}s_{0p}\cos\chi_{in}}$ depends on the probe and pump intensity (s_{0i}) and on the angle χ_{in} between the two input signals Stokes vectors, while the pivot direction $\hat{m}$ depends on the input signals polarizations $\hat{s}_s$ and $\hat{s}_p$, for given intensities. The closed form solution for equations (3.3) is reported in Sec. 1.2.3 (equations (1.28)). Concentrating only on the evolution of the signal Stokes vector $\overrightarrow{s}_s(z)$, its value at the fiber output can be written as

$$\overrightarrow{s}_s(L) = \overrightarrow{s}_s(0)\cos\phi_{NL} + \frac{\overrightarrow{m}\cdot\overrightarrow{s}_s(0)}{m_0^2}\overrightarrow{m}\,(1-\cos\phi_{NL}) + \frac{\overrightarrow{m}\times\overrightarrow{s}_s(0)}{m_0}\sin\phi_{NL}, \quad (3.4)$$

where $\cdot$ represents the inner product, while $\times$ represents the cross-product.

By considering, for example, input signals with relative polarization angle χ_{in} and equal power $s_{0s} = s_{0p} = P$, the pivot $\overrightarrow{m}$ is exactly middle-way between the input signal Stokes vectors, while its magnitude is $m_0 = P\left(2\left(1+\cos\chi_{in}\right)\right)^{1/2}$. The trajectory followed by the signals SOPs along the fiber are circles centered on the pivot. Hence, for the special angle χ_{in}, at each coordinate z_i such that $\phi_{NL}(z_i) = (2k+1)\pi$ $(k$ integer), vectors $\overrightarrow{s}_s(z_i)$ and $\overrightarrow{s}_p(z_i)$ switch their places $(\hat{s}_s(z_i) = \hat{s}_p(0)$ and $\hat{s}_p(z_i) = \hat{s}_s(0))$, hence an "ideal (fake) attraction" of the signal SOP onto the pump SOP is obtained[1]. I wish to design the NLP parameters (fiber length and signal powers) in such a way that signals swap their place almost exactly, independently of the angle χ_{in}. Maintaining equal signals power, the goal introduced above is impossible to obtain, since m_0 changes for each angle χ_{in}, hence coordinates z_i change with it. This is the case studied in [59] where, as pointed out by the authors, the performance of the NLP, in terms of DOP, is poor (DOP = 0.73).

Here, I propose to change the pump power according to the input signal SOP, hence according to the angle χ_{in}, to optimize it and to enhance the performance of the NLP operating in polarization rotation regime. To do this, I selected the pump power to maximize the degree of attraction at the output of the NLP for every angle χ_{in}, hence

$$s_{0p}^{opt} \triangleq \max_{s_{0p}} \{\mathrm{DOA}\}. \quad (3.5)$$
$$0 \le s_{0p} \le s_{0p}^{max}$$

[1] For example, in Fig. 3.4 an "ideal (fake) attraction" was obtained with $z_i = 8$ km.

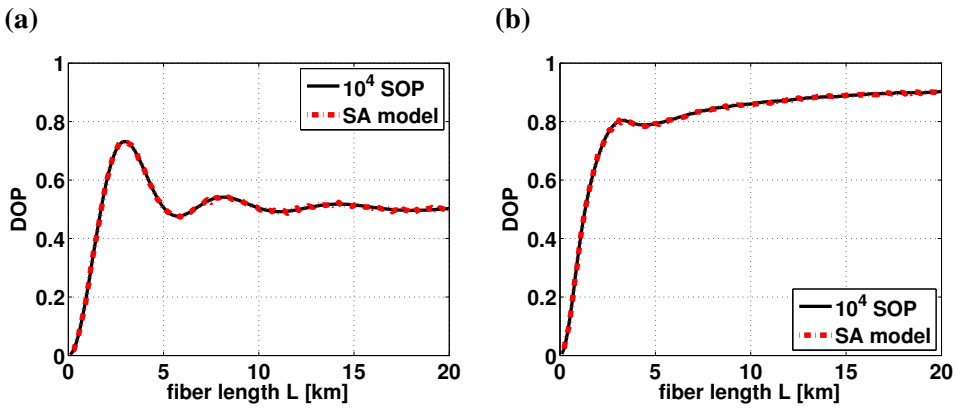

Figure 3.10: Performance of the NLP working in polarization rotation regime: degree of polarization (DOP) as a function of the fiber length. The input signal power is $s_{0s} = 1$ W, while the pump power is fixed $s_{0p} = s_{0s} = 1$ W (a) or optimized (b), according to criterion (3.5).

In (3.5), the DOA is evaluated according to (1.34), between the output signal SOP and the input pump SOP. Moreover, I considered the pump power constrained in the range $0 \leq s_{0p} \leq s_{0p}^{max}$, where s_{0p}^{max} is the maximum pump power available. The application of equation (3.5) to select the pump power implies that also the averaged $\overline{\text{DOA}}$ is maximized; since the output signal SOPs are attracted towards the input pump SOP (see Sec. 3.5), $\overline{\text{DOA}}$ is equal to the degree of polarization evaluated as $\text{DOP} = \left\| E\left[\left\langle \overrightarrow{s}_s(t)\right\rangle\right]\right\| / \left\langle s_{0s}(t)\right\rangle$. Of course, In the case where signals powers are different, the pivot is no longer exactly middle way between the input signals Stokes vectors, hence the trajectory of the signal SOP does not pass exactly through the pump SOP, rather it remains inner (outer) if $s_{0s} > s_{0p}$ ($s_{0s} < s_{0p}$).

Fig. 3.10 shows the DOP (solid, black, line) of the signal output from the NLP as a function of the fiber length, either for a fixed (a) or an optimized (b) pump power value. The output signal Stokes vector, $\overrightarrow{s}_s(L)$, is evaluated by directly solving (3.4). As in [59], the signal power is $s_{0s} = 1$ W (fixed), while the nonlinear Kerr coefficient is $\gamma = 1\ \text{W}^{-1}\text{km}^{-1}$ (as in Sec. 3.5). In Fig. 3.10(a), the pump power is $s_{0p} = s_{0s} = 1$ W, hence the DOP curve exactly coincides with the results published in [59]. On the other hand, in Fig. 3.10(b), the pump power value was optimized according to criterion (3.5), with the pump power constrained in the range $0 \leq s_{0p} \leq 2s_{0s}$ (i.e., $s_{0p}^{max} = 2$ W, in the present case). I verified numerically that, even using $s_{0p}^{max} = 10s_{0s}$, the optimal pump power results $s_{0p}^{opt} \leq 2s_{0s}$ for almost all tested input SOPs and fiber lengths.

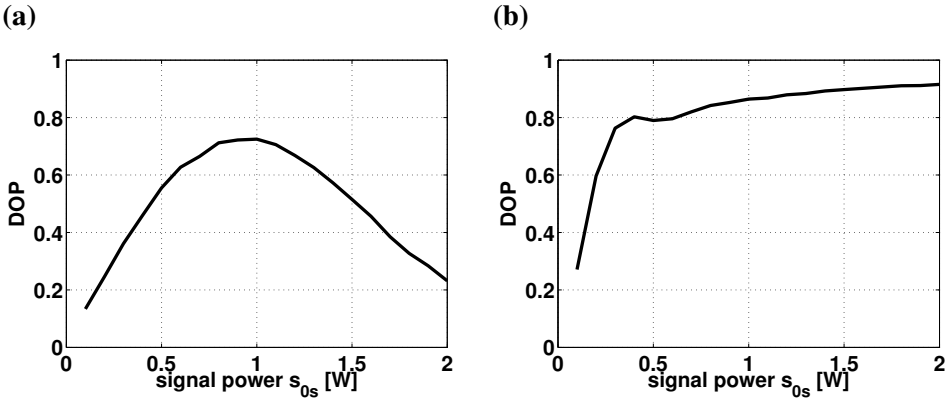

Figure 3.11: Performance of the NLP working in polarization rotation regime: degree of polarization (DOP) as a function of the input signal power s_{0s}. The input pump power is fixed $s_{0p} = 1$ W (a) or optimized (b), according to criterion (3.5). The fiber length is $L = 3$ km (a) or $L = 10$ km (b).

In fact, when $s_{0p} \gg s_{0s}$, the pivot vector $\overrightarrow{m}$ almost coincides with the pump vector $\overrightarrow{s}_p$, hence the signal vector $\overrightarrow{s}_s$ would rotate around the pump SOP and would not be attracted towards it but rather remain at a constant angular distance, close to the initial χ_{in}. The DOP in Fig. 3.10 was (statistically-)averaged over 10^4 input signal SOP ($\overrightarrow{s}_s(0)$) realizations, uniformly distributed on the Poincaré sphere, so that the input DOP is practically zero.

By comparing Fig. 3.10(a), where the pump power is fixed, with Fig. 3.10(b), where the pump power is optimized, we can see that the optimization of the pump power value makes the DOP increase constantly with the fiber length, allowing to obtain a best DOP value (0.9, in Fig. 3.10(b)) larger than that obtained with a fixed pump power (0.73, in Fig. 3.10(a)). When the pump power value is fixed (a), the DOP curve shows an optimal fiber length $L = 3$ km, at which the best DOP is obtained, while with a longer fiber the DOP seems to settle around 0.5. The optimal fiber length strongly depends on the signals power employed, as I numerically verified, hence the fiber length can be evaluated only once the signals powers were selected. On the other hand, if the fiber length is fixed, a change in the signal power makes the DOP of the output signal decrease, as shown in Fig. 3.11(a).

Here, I used the optimal fiber length, hence $L = 3$ km, and plotted the output signal DOP as a function of the input signal power s_{0s} (the input pump power is $s_{0p} = 1$ W). With unbalanced signal and pump power, the DOP decreases with respect

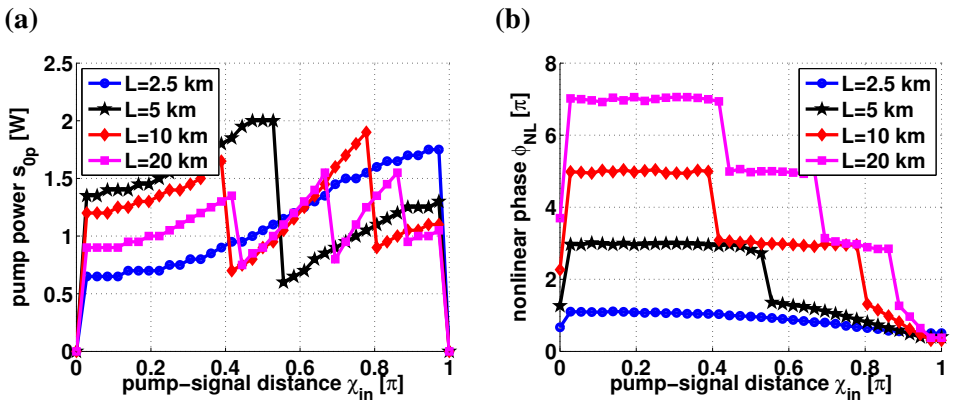

Figure 3.12: Optimal pump power value s_{0p}^{opt} (a) and corresponding nonlinear phase rotation ϕ_{NL} (b), as a function of the angular distance χ_{in} between the input signal Stokes vectors. The input signal power is $s_{0s} = 1$ W, while the input pump power s_{0p}^{opt} is evaluated according to criterion (3.5).

to its maximum value, obtained with equal signals power ($s_{0p} = s_{0s}$). This is no longer true when the pump power value is optimized, according to criterion (3.5), as shown in Fig. 3.11(b), where a fiber length $L = 10$ km was employed. Here, the pump power optimization makes the output signal DOP grow continuously with signal power. The optimized pump power in Fig. 3.11(b) is still in the range $0 \leq s_{0p} \leq 2s_{0s}$, hence its maximum value s_{0p}^{max} changes with s_{0s}.

In Fig. 3.10, the (red) dot-dashed line was obtained by implementing a semi-analitical model. In particular, instead of solving (3.4) for 10^4 random input signal SOPs (solid line), I used 37 input signal SOPs, whose angular distance χ_{in} from the input pump SOP ranges from 0° to 180°, with steps of 5°. I evaluated the DOA at the NLP output for each value of χ_{in}, hence for each input signal SOP. The averaged degree of attraction, $\overline{\text{DOA}}$ (dot-dashed, red, line), was evaluated by weighting the DOA through the distribution of the angle χ_{in}, that is $f(x_{in}) = \frac{1}{2}\sin(x_{in})$ ($0 \leq \chi_{in} \leq 180°$) [64], hence $\overline{\text{DOA}} = \frac{1}{2}\int_0^{\pi} \text{DOA}(\chi_{in})\sin(\chi_{in})\,d\chi_{in}$. Since $\overline{\text{DOA}}$ is equal to the DOP, as stated previously, the (red) dot-dashed line perfectly overlaps the (black) solid line.

The semi-analitical model, in addition to decreasing the numerical simulation time needed to measure the output signal DOP, allows to study the performance of the NLP as a function of the angle χ_{in}, hence of the input signal SOP. Fig. 3.12 shows the dependence of the optimal pump power value (s_{0p}^{opt}) (a) and of the corresponding

nonlinear phase rotation ϕ_{NL} (b), on the angle χ_{in} between the input signals Stokes vectors, for different values of the fiber length (different symbols, colors). In Fig. 3.12, the angle χ_{in} is normalized with respect to π, so that it ranges from 0 (parallel input signal SOPs) to 1 (orthogonal input signal SOPs), while the input signal power is $s_{0s} = 1$ W. As guessed, criterion (3.5) selects the pump power s_{0p}^{opt} (Fig. 3.12(a)) in such a way that the nonlinear phase rotation is roughly equal to an odd multiple of π, hence $\phi_{NL} = (2k+1)\pi$ $(k = 1,2,etc)$, for almost all input signal SOPs (Fig. 3.12(b)). Since the pivot magnitude m_0 decreases by increasing the angle χ_{in}, the pump power has to be increased, to maintain a constant ϕ_{NL} for the input signal SOP further from the pump SOP. When it is no more convenient to increase the pump power more, the curves representing s_{0p}^{opt} show a discontinuity, after which s_{0p}^{opt} starts to increase again from a lower level, corresponding to the cancellation of a complete tour of the signal SOP around the pivot vector, i.e., to a decrease of ϕ_{NL} by 2π, as visible in Fig. 3.12(b). The longer the fiber the larger the number of laps that the signal SOP makes on the Poincaré sphere, hence the larger the number of steps from $\phi_{NL} = n\pi$ to $\phi_{NL} = (n-2)\pi$ (with n odd). The number of laps that the signal SOP makes around the pivot vector decreases by increasing its angular distance χ_{in} from the input pump SOP. For further SOPs, with an angular distance χ_{in} close to π (i.e., for almost orthogonal SOPs), the nonlinear polarization interactions between pump and signal are almost vanished, hence the signal SOP remains almost constant, as demonstrated by the value of $\phi_{NL} \cong 0$ in the right side of Fig. 3.12 for all curves.

Until now, I have analyzed a simplified model, given by the system of motion equations (3.3), which holds for CW signals, co-propagating at the same speed within an optical fiber where the GVD terms can safely be neglected. As stated in Sec. 1.2.3, system (3.3) captures all the Kerr-induced polarization effects that produce polarization rotation, but in the Stokes domain all the nonlinear scalar effect (SPM and XPM) are not taken into account. To prove that results obtained through system (3.3) represent a good approximation of the real behavior of the NLP, Fig. 3.13 shows the DOP versus the fiber length, obtained by solving the complete propagation equation (1.18), in Jones domain, resorting to the *Optilux* tool [62], hence by employing the SSFM.

To quantify the impact of the (amplitude) modulation of the signal and of the fiber dispersion (GVD) on the NLP performance, I compare the DOP obtained by solving (3.4) (solid, black, line) with the DOP obtained for an amplitude modulated input signal (on-off keying, OOK), when the signals propagation, solved by resorting to the SSFM, is unaffected (dashed, red, line) or affected (dot-dashed, blue, line) by the GVD.

Since signals propagate at the same velocity, each time sample of the signal in-

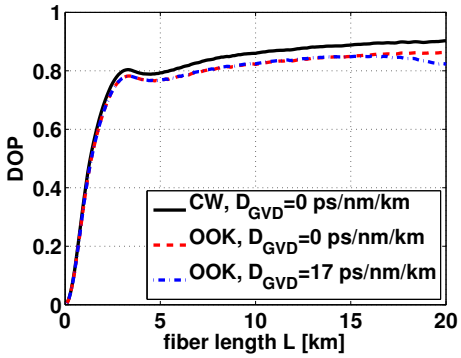

Figure 3.13: Performance of the NLP working in polarization rotation regime: degree of polarization (DOP) as a function of the fiber length. The input signal power is $s_{0s} = 1$ W, while the pump power is optimized according to criterion (3.5). DOP is obtained by solving (3.4) (solid, black, line), or by solving the complete propagation equation (in Jones), by resorting to the SSFM, including (dot-dashed, blue, line) or not (dashed, red, line) the fiber dispersion (GVD).

teracts, for the whole fiber length, with the same time sample of the pump. When the signal power is on (bit 1), model (3.4) applies as if the signal were CW, while when signal power is off, there is no interaction between signal and pump. Anyway, the DOP of a CW signal represents an upper limit for the DOP of an amplitude modulated signal [45], due to the rising/trailing edges of the signal pulses. Fig. 3.13 shows that the discrepancy between the DOP obtained with a CW signal and that obtained with an OOK-modulated signal is less than 0.05. Regarding the impact of the GVD, Fig. 3.13 shows that with a dispersion parameter D = 17 ps/nm/km, the performance of the NLP device is almost unaffected, since the dispersion length is $L_D \gg L$ for almost all the tested fiber lengths (hence, the pulse broadening can be considered negligible). A slight decrease of the DOP appears only for fiber length $L > 16$ km. Since the discrepancy between the DOP obtained by solving (3.4) (solid, black, line) and that obtained by solving the complete propagation equation (1.18) (dot-dashed, blue, line) are negligible and due to the effect of the modulation and of the GVD, I can guess that also the nonlinear scalar effect (SPM and XPM) does not affect the NLP performance, despite the large signals power employed here (few watts).

Note that to further increase the performance of the NLP working in polarization rotation regime, two (or more) devices could be cascaded, as described in [59]. At the input of each NLP, an undistorted pump is injected with the signal into the fiber,

while it is separated from it at the output of the NLP. As a further consideration, by employing an NLP device operating in the polarization rotation regime (with zero walk-off), the repolarization of the signal, i.e., its output DOP, is independent of both its polarization coherence time and duration. In fact, the co-propagation geometry makes the NLP transient time adaptable to any polarization coherence time of the signal, while the zero walk-off makes the nonlinear interaction between the signal and pump independent of their duration.

3.4.2 Analytical solution for the DOA

In this section, I develop a theoretical analysis in order to predict analytically the performance of a NLP device, when it works in polarization rotation regime, with zero walk-off delay between signal and pump. Hence, by considering the signals Stokes vector evolution governed by the system of motion equations (3.3), the closed-form solution for the signal Stokes vector, $\overrightarrow{s}_s(L) = s_{0s}(L)\hat{s}_s(L)$, at the output of the NLP is given by (3.4).

By considering a particular input signal SOP $\hat{s}_s(0)$, which I identify through the angle χ_{in} that it forms with the input pump SOP $\hat{s}_p(0)$, its degree of attraction at the fiber output, evaluated with respect to the input pump SOP (according to (1.34), reported in chapter 1), is $\mathrm{DOA} = \left(\overrightarrow{s}_s(L)/s_{0s}(L)\right) \cdot \hat{s}_p(0) = \hat{s}_s(L) \cdot \hat{s}_p(0)$[2]. By taking the scalar product of both sides of (3.4) with the input pump Stokes vector $\overrightarrow{s}_p(0) = s_{0p}\hat{s}_p(0)$, the closed-form solution for the DOA for the signal at the NLP output can be expressed as

$$\mathrm{DOA} = \mathrm{DOA}_{\mathrm{in}} \cos\phi_{NL} + \frac{\left(s_{0s} + s_{0p}\mathrm{DOA}_{\mathrm{in}}\right)\left(s_{0p} + s_{0s}\mathrm{DOA}_{\mathrm{in}}\right)}{m_0^2}\left(1 - \cos\phi_{NL}\right), \tag{3.6}$$

where $\mathrm{DOA}_{\mathrm{in}} = \cos(\chi_{in})$ is evaluated at the NLP input. In (3.6), the DOA at the NLP output is expressed as a function of the input signal conditions (i.e., signals powers, s_{0s} and s_{0p}, and the relative signals Stokes position on the Poincaré sphere, χ_{in}) and of the fiber parameters (i.e., fiber type, γ, and length, L). Note that the fiber parameters impact the DOA only through the nonlinear phase ϕ_{NL}, which quantifies the angular distance traveled by the signals Stokes vectors on the Poincaré sphere. Equation (3.6) confirms that, with parallel (orthogonal) input signals SOPs, i.e., for $\chi_{in} = 0°$ ($\chi_{in} = 180°$), the DOA remains constant along the NLP and equal to $\mathrm{DOA} = \mathrm{DOA}_{\mathrm{in}} = 1$

[2]The time-averaging of the signal Stokes vector $\overrightarrow{s}_s(L)$, in the DOA definition, disappears here since I am considering a CW input signal.

($\mathrm{DOA} = \mathrm{DOA}_{\mathrm{in}} = -1$). A formula similar to (3.6) was obtained, for the first time, by Turitsyn and Wabnitz in [66], for counter-propagating CW signals.

By manipulating (3.6), it is easy to demonstrate that the DOA can be written as

$$\mathrm{DOA} = \mathrm{DOA}_{\mathrm{in}} + \frac{s_{0s} s_{0p} \left(1 - \mathrm{DOA}_{\mathrm{in}}^2\right)}{m_0^2} \left(1 - \cos \phi_{NL}\right). \tag{3.7}$$

Expression (3.7) gives the DOA of the output signal in a more useful form, since it analytically demonstrated that $\mathrm{DOA} \geq \mathrm{DOA}_{\mathrm{in}}$, being the factor added to the input value, $\mathrm{DOA}_{\mathrm{in}}$, a non negative quantity. In other words, at the output of the NLP device, the signal SOP can be closer to (i.e., $\mathrm{DOA} > \mathrm{DOA}_{\mathrm{in}}$) or stay at the same distance from (i.e., $\mathrm{DOA} = \mathrm{DOA}_{\mathrm{in}}$) the input pump SOP, compared with the signal SOP at the NLP input, but it cannot be moved away from the pump SOP (i.e., $\mathrm{DOA} < \mathrm{DOA}_{\mathrm{in}}$ never occurs). In (3.7), the factor added to $\mathrm{DOA}_{\mathrm{in}}$ can be seen as the product between two (positive) functions of s_{0p}, defined as

$$f\left(s_{0p}\right) \triangleq \frac{s_{0s} s_{0p} \left(1 - \mathrm{DOA}_{\mathrm{in}}^2\right)}{m_0^2}; \qquad g\left(s_{0p}\right) \triangleq \left(1 - \cos \phi_{NL}\right). \tag{3.8}$$

Such a product represents the DOA gain, $G_{\mathrm{DOA}} \triangleq f\left(s_{0p}\right) g\left(s_{0p}\right)$, provided by the NLP device, with respect to the input condition $\mathrm{DOA}_{\mathrm{in}}$. Moreover, (3.7) demonstrates that the signal SOP does not change, hence $G_{\mathrm{DOA}} = 0$, whenever the nonlinear phase takes values $\phi_{NL} = 2n\pi$, with n positive integer, since the signal SOP returns exactly to its initial position on the Poincaré sphere, i.e., $\hat{s}_s(L) = \hat{s}_s(0)$.

The DOA, analytically evaluated as in (3.7), can be adopted to evaluate the optimal pump power s_{0p}^{opt}, according to criterion (3.5), and the average degree of attraction $\overline{\mathrm{DOA}} = \frac{1}{2} \int_0^{\pi} \mathrm{DOA} \sin\left(\chi_{in}\right) d\chi_{in}$. A closed-form solution does not exist, for both quantities s_{0p}^{opt} and $\overline{\mathrm{DOA}}$, hence their values must be calculated numerically. Anyway, in the section that follows I provide an approximate formula to estimate the optimal pump power s_{0p}^{opt}.

3.4.3 Pump power optimization: analytical approach

As already stated in Sec. 3.4.1, the goal is to optimize the pump power value for every input signal SOP, hence for every angle χ_{in}, in order to enhance the performance of the NLP device working in polarization rotation regime. To do this, the pump power has to be selected to maximize the DOA, evaluated between the signal output from the

NLP and the input pump SOP, according to criterion (3.5). By imposing the analytical expression (3.7) of the DOA in the optimization criterion (3.5), it corresponds to maximizing the DOA gain G_{DOA}, since $\mathrm{DOA}_{\mathrm{in}}$ is independent of the pump power, hence

$$\begin{aligned} s_{0p}^{opt} &= \max_{s_{0p}} \left\{ G_{\mathrm{DOA}} \right\} \\ &= \max_{s_{0p}} \left\{ \frac{s_{0s} s_{0p} \left(1 - \mathrm{DOA}_{\mathrm{in}}^2 \right)}{m_0^2} \left(1 - \cos \phi_{NL} \right) \right\}, \end{aligned} \tag{3.9}$$

where the signal power s_{0s}, the input condition $\mathrm{DOA}_{\mathrm{in}}$ and the fiber length L are considered as given constants for the optimization problem. The DOA gain G_{DOA}, seen as a function of the pump power s_{0p}, is a dumped oscillating function, hence characterized by many local maxima. As a consequence, (3.9) must be solved as a global optimization problem, for which several techniques are provided in the literature. The exact solution of the global optimization problem (3.9) is beyond the scope of this section, since an example of such a solution has already been found (numerically) and shown in Fig. 3.12(a). Anyway, here I make some considerations on problem (3.9), which allow me to obtain an approximate closed-form solution for the optimal pump power s_{0p}^{opt}. In particular, in the sections that follows I assume to optimize the function $f(s_{0p})$ and $g(s_{0p})$ separately, thus providing suboptimal choices for the pump power s_{0p}^{opt}.

Optimization of $f(s_{0p})$

Here, I assume to select the optimal pump power by maximizing the function $f(s_{0p})$, defined in (3.8), instead of the DOA gain G_{DOA}. Hence, the (sub)optimal pump power s_{0p}^{f} satisfies the optimization criterion

$$\begin{aligned} s_{0p}^{f} &\triangleq \max_{s_{0p}} \left\{ f(s_{0p}) \right\} \\ &\quad 0 \leq s_{0p} \leq s_{0p}^{max}. \end{aligned} \tag{3.10}$$

Function $f(s_{0p})$ depends only on the input signals conditions, i.e., on the signals powers, s_{0s} and s_{0p}, and on the angular distance χ_{in} between the Signals Stokes vectors. Hence, the value of $f(s_{0p})$ is independent of the fiber where the lossless polarization attraction process takes place. Moreover, it is easy to demonstrate that the limit of $f(s_{0p})$ when the pump power $s_{0p} \to +\infty$ is zero, confirming that for strongly unbalanced signals powers (i.e., for $s_{0p} \gg s_{0s}$), the repolarization of the signal does not

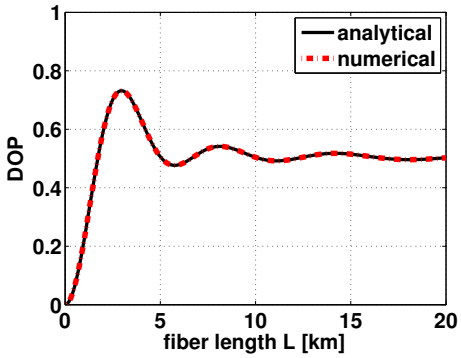

Figure 3.14: Signal DOP for the NLP working in polarization rotation regime: analytical vs numerical solution. The input signals powers are $s_{0p} = s_{0s} = 1$ W. The pump power was analytically evaluated according to criterion (3.10).

occur, since also $G_{\mathrm{DOA}} \to 0$. Physically, this condition corresponds to a pivot vector $\overrightarrow{m} \simeq \overrightarrow{s}_p$; hence, the signal Stokes vector $\overrightarrow{s}_s$ simply rotates around the pump SOP $\hat{s}_p$, without approaching it.

To solve problem (3.10), I thus evaluate the first order derivative of $f(s_{0p})$ with respect to the pump power s_{0p}, $f'(s_{0p}) \triangleq \frac{\partial f(s_{0p})}{\partial s_{0p}}$, that results

$$f'(s_{0p}) = \frac{s_{0s}\left(s_{0s}^2 - s_{0p}^2\right)\left(1 - \mathrm{DOA}_{\mathrm{in}}^2\right)}{m_0^4}. \tag{3.11}$$

By imposing (3.11) equal to zero and considering only the positive solution for the pump power s_{0p} (for physical reason) it is easy to show that the unique solution for the optimization problem (3.10) is $s_{0p}^f = s_{0s}$, hence pump and signal must have the same power.

By imposing equal signals powers $s_{0p}^f = s_{0s} = s_0$ in (3.7), the output DOA can be written as

$$\mathrm{DOA} = \mathrm{DOA}_{\mathrm{in}} + \frac{\left(1 - \mathrm{DOA}_{\mathrm{in}}\right)}{2}\left(1 - \cos\phi_{NL}\right), \tag{3.12}$$

where I replaced the pivot magnitude m_0^2 with its expression, hence $m_0^2 = 2s_0^2\left(1 + \mathrm{DOA}_{\mathrm{in}}\right)$, and recognize that $\left(1 - \mathrm{DOA}_{\mathrm{in}}^2\right) / \left(1 + \mathrm{DOA}_{\mathrm{in}}\right) = \left(1 - \mathrm{DOA}_{\mathrm{in}}\right)$.

By using the DOA expressed as in (3.12) to evaluate its averaged value, $\overline{\mathrm{DOA}} = \mathrm{DOP}$, and plotting it as a function of the fiber length, I obtained the solid (black)

curve reported in Fig. 3.14. Since here the signals power is $s_{0p}^{f} = s_{0s} = 1$ W, as used to obtain Fig. 3.10(a), such a curve exactly coincides with the dot-dashed (red) curve, which represents the DOP of the output signal evaluated numerically by (statistically-)averaging over 10^4 input signal SOP realizations. Such a result theoretically justifies the poor NLP performance obtained in [59], where equal signals power were employed, hence a suboptimal choice for the pump power was made.

Optimization of $g(s_{0p})$

Here, I assume to select the optimal pump power by maximizing the function $g(s_{0p})$, defined in (3.8), instead of the DOA gain G_{DOA}. Hence, the (sub)optimized pump power s_{0p}^{g} satisfies the optimization criterion

$$\begin{aligned} s_{0p}^{g} \quad &\triangleq \quad \max_{s_{0p}} \{g(s_{0p})\} \\ &\qquad 0 \leq s_{0p} \leq s_{0p}^{max}. \end{aligned} \tag{3.13}$$

Function $g(s_{0p})$ is an oscillating function, taking values in the range $0 \leq g(s_{0p}) \leq 2$, that depends on both the input signals conditions, i.e., signals powers and relative position χ_{in}, and on the fiber parameters, i.e., fiber type and length, through the nonlinear phase ϕ_{NL}.

As in the previous section, to solve problem (3.13), I evaluate the first order derivative of $g(s_{0p})$ with respect to the pump power s_{0p}, $g'(s_{0p}) \triangleq \frac{\partial g(s_{0p})}{\partial s_{0p}}$, that results

$$g'(s_{0p}) = -k \frac{s_{0p} + s_{0s}\mathrm{DOA}_{\mathrm{in}}}{m_0} \sin\phi_{NL}, \tag{3.14}$$

where I define $k \triangleq \frac{8}{9}\gamma L_{eff}$. By imposing (3.14) equal to zero, three different solution for s_{0p} exist. The first one is obtained by imposing that the function multiplying $\sin\phi_{NL}$ equal to zero, while the second and third solutions are obtained by imposing $\sin\phi_{NL}$ equal to zero. Below, I analyze the three solutions separately.

1st solution. By imposing $\frac{s_{0p}+s_{0s}\mathrm{DOA}_{\mathrm{in}}}{m_0} = 0$, the first solution that solves $g'(s_{0p}) = 0$ results $s_{0p} = -s_{0s}\mathrm{DOA}_{\mathrm{in}}$. Since the power is a positive quantity, $s_{0p} = -s_{0s}\mathrm{DOA}_{\mathrm{in}}$ represents a physically meaningful solution only when $\mathrm{DOA}_{\mathrm{in}} < 0$, hence when the angle between the input signals SOPs is $90° < \chi_{in} < 180°$. Despite such a solution could represents the solution of the optimization problem (3.13), hence $s_{0p}^{g} = -s_{0s}\mathrm{DOA}_{\mathrm{in}}$, for some particular input signal SOP (such that $\mathrm{DOA}_{\mathrm{in}} < 0$), I rejected it since I am looking for a solution that is valid for all input conditions.

2nd and 3rd solution. The second and third solutions for the problem (3.13) are obtained by imposing $\sin\phi_{NL}=0$, hence they are obtained for $\phi_{NL}=2n\pi$ or $\phi_{NL}=(2n+1)\pi$, with n positive integer. In the first case, with $\phi_{NL}=2n\pi$, function $g(s_{0p})=0$, thus representing a minimum for the DOA gain that is $G_{\mathrm{DOA}}=0$. As stated above, such a solution physically represents a signal SOP that complete a lap around the pivot, thus returning to its initial position ($\mathrm{DOA}=\mathrm{DOA}_{\mathrm{in}}$). On the other hand, with $\phi_{NL}=(2n+1)\pi$, function $g(s_{0p})=2$ takes its maximum value. Such a solution physically represents a signal SOP that completes half a lap around the pivot, thus exchanging its position with the input pump SOP, and analytically justifies numerical results reported in Fig. 3.12(b). Concentrating on such a solution, the optimal pump power must solve the equation

$$\phi_{NL}=k\sqrt{s_{0s}^2+s_{0p}^2+2s_{0s}s_{0p}\mathrm{DOA}_{\mathrm{in}}}=(2n+1)\pi. \tag{3.15}$$

Equation (3.15) admits two solutions for the pump power, indicated with s_{0p}^1 and s_{0p}^2, which are

$$s_{0p}^{1,2}=-s_{0s}\mathrm{DOA}_{\mathrm{in}}\pm\sqrt{s_{0s}^2\left(\mathrm{DOA}_{\mathrm{in}}^2-1\right)+\left(\frac{2n+1}{k}\pi\right)^2}. \tag{3.16}$$

The terms within the square root in (3.16) impose a condition on the positive integer n, in order to obtain a real solution for the pump power (for physical reasons), that is

$$n\geq\left\lceil\frac{ks_{0s}\sqrt{1-\mathrm{DOA}_{\mathrm{in}}^2}}{2\pi}-\frac{1}{2}\right\rceil, \tag{3.17}$$

where $\lceil . \rceil$ represent the upper integer.

For each n that satisfies criterion (3.17), the solution s_{0p}^2, i.e., (3.16) with the minus sign, takes negative value when $\mathrm{DOA}_{\mathrm{in}}>0$, hence when the angle between the input signals SOPs is $0^\circ<\chi_{in}<90^\circ$. Thus, I rejected it since I am looking for a solution that is valid for all input conditions.

On the other hand, the solution s_{0p}^1, i.e., (3.16) with the plus sign, takes positive values for any input condition, hence for any $\mathrm{DOA}_{\mathrm{in}}$, provided that integer n satisfies the further condition[3]

$$n\geq\left\lceil\frac{ks_{0s}}{2\pi}-\frac{1}{2}\right\rceil\geq\left\lceil\frac{ks_{0s}\sqrt{1-\mathrm{DOA}_{\mathrm{in}}^2}}{2\pi}-\frac{1}{2}\right\rceil. \tag{3.18}$$

[3]The further condition on n is needed only for $\mathrm{DOA}_{\mathrm{in}}>0$.

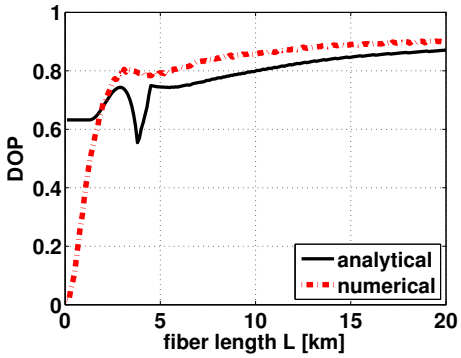

Figure 3.15: Signal DOP for the NLP working in polarization rotation regime: analytical vs numerical solution. The input signal power is $s_{0s} = 1$ W, while the pump power is analytically evaluated according to (3.19), which satisfy criterion (3.13).

Thus, I approximate the optimal pump power s_{0p}^{g}, which solves the optimization problem (3.13), as

$$s_{0p}^{g} = -s_{0s}\mathrm{DOA}_{\mathrm{in}} + \sqrt{s_{0s}^{2}\left(\mathrm{DOA}_{\mathrm{in}}^{2} - 1\right) + \left(\frac{2n+1}{k}\pi\right)^{2}}. \tag{3.19}$$

The DOA in (3.7), evaluated by imposing the optimal pump power s_{0p}^{g} (3.19), becomes

$$\mathrm{DOA} = \mathrm{DOA}_{\mathrm{in}} + 2\frac{s_{0s}s_{0p}^{g}\left(1 - \mathrm{DOA}_{\mathrm{in}}^{2}\right)}{m_{0}^{2}\Big|_{s_{0p}^{g}}}, \tag{3.20}$$

where the pivot magnitude m_0 is evaluated for the optimal pump power s_{0p}^{g} (3.19).

By using the DOA expressed as in (3.20) to evaluate its averaged value, $\overline{\mathrm{DOA}} = \mathrm{DOP}$, and plotting it as a function of the fiber length, I obtained the solid (black) curve reported in Fig. 3.15. Since here the input signal power is $s_{0s} = 1$ W (while the pump power s_{0p}^{g} is evaluated according to (3.19)), such a curve is compared with the dot-dashed (red) curve, which is that reported in Fig. 3.10(b). Thus, the dot-dashed (red) curve represents the DOP of the output signal evaluated numerically by (statistically-)averaging over 10^4 input signal SOP realizations, with an optimized pump power s_{0p}^{opt} that satisfy criterion (3.5). As demonstrated by comparing the two curves in Fig. 3.15, the approximated analytical solution (3.20) for the DOA, from which I evaluated the $\overline{\mathrm{DOA}}$, represents a good model for the NLP performance working in

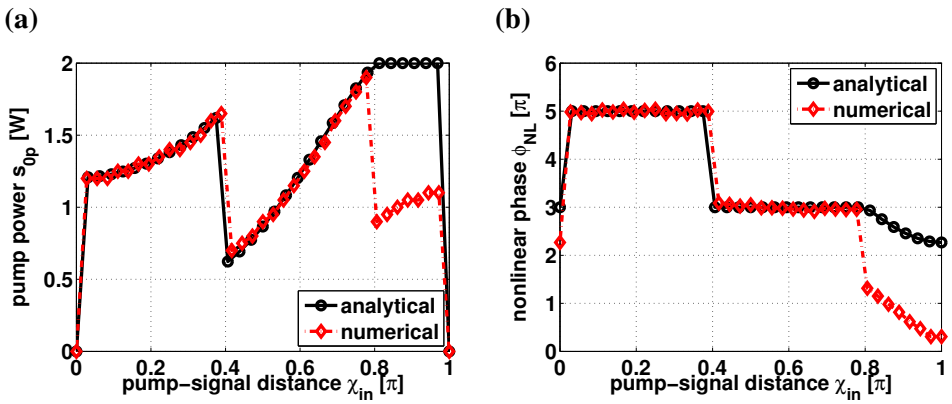

Figure 3.16: Optimal pump power value (a) and corresponding nonlinear phase rotation ϕ_{NL} (b), as a function of the angular distance χ_{in} between the input signal Stokes vectors: analytical vs numerical solutions. The input signal power is $s_{0s} = 1$ W, while the pump power is analytically evaluated according to (3.19), which satisfies criterion (3.13).

the polarization rotation regime (with zero walk-off). In particular, being the solid curve always below the dashed curve, except for short fiber length $L < 3$ km[4], it represents a "lower bound" for the real NLP performance.

As a consequence, the analytical expression (3.19) for the pump power, s_{0p}^{g}, represents a good approximation for the optimal pump power s_{0p}^{opt} that solves the optimization problem (3.5). Such a statement is confirmed in Fig. 3.16, which compares the optimal pump power (a) or the nonlinear phase ϕ_{NL} (b), evaluated by using the analytical expression (3.19) (solid, black, line) or by numerical simulation (dot-dashed, red, line). In particular, the dot-dashed (red) lines in Fig. 3.16 coincide with the curves reported in Fig. 3.12, for a fiber length $L = 10$ km. As can be clearly seen in Fig. 3.16, analytical and numerical solutions overlap as far as the angular distance between the input signals Stokes vectors is $\chi_{in} \leq 0.8\pi$, to which $\mathrm{DOA_{in}} \leq -0.8$ corresponds. The discrepancies between analytical and numerical solutions, for further input signals SOPs (close to the orthogonal condition), explains the discrepancies between the two curves in Fig. 3.15. Moreover, the discrepancies between analytical and numerical solutions in Fig. 3.16, for further input signals SOPs, happens

[4]With $L \to 0$, the pump power $s_{0p}^{g} \to +\infty$, since the fiber length appear at the denominator in expression (3.19). Given the constrain $s_{0p} \leq s_{0p}^{max}$, the pump power remains constant, $s_{0p}^{g} = s_{0p}^{max}$, hence also the DOA, expressed as in (3.20), remains constant.

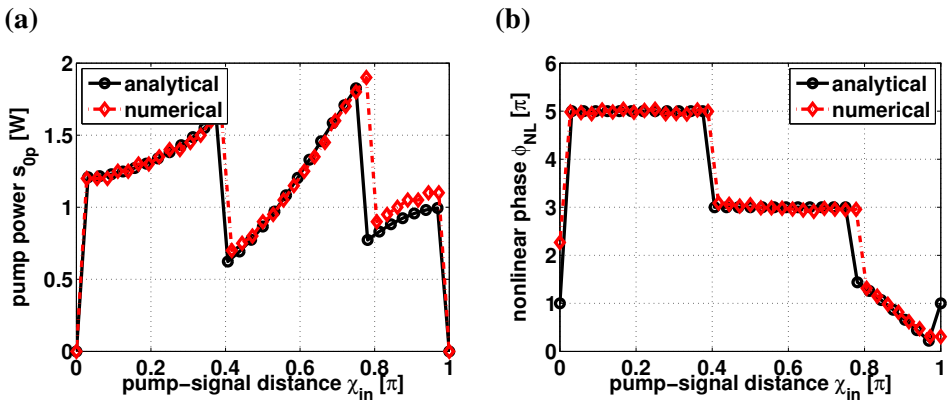

Figure 3.17: Optimal pump power value (a) and corresponding nonlinear phase rotation ϕ_{NL} (b), as a function of the angular distance χ_{in} between the input signal Stokes vectors: analytical vs numerical solutions. The input signal power is $s_{0s} = 1$ W, while the pump power s^g_{0p}, analytically evaluated, is selected between expression (3.19) and $-s_{0s}\mathrm{DOA}_{\mathrm{in}}$.

because in such a region the optimal pump power is well approximated by the solution $s_{0p} = -s_{0s}\mathrm{DOA}_{\mathrm{in}}$(which holds for $\mathrm{DOA}_{\mathrm{in}} < 0$), instead of expression (3.19). To demonstrate this statement, Fig. 3.17 shows the optimal pump power (a) and the nonlinear phase (b), analytically evaluated by selecting the optimal pump power s^g_{0p} between $-s_{0s}\mathrm{DOA}_{\mathrm{in}}$ and the expression (3.19), for each input signal SOP (i.e., for each χ_{in}). Such a curve, reported with solid (black) line, is compared with the numerical results, reported with dot-dashed (red) line. Given the good agreement between the analytical and numerical solutions reported in Fig. 3.17, also the $\overline{\mathrm{DOA}}$, evaluated by employing such an analytical solution for the pump power is close to the DOP evaluated numerically, as verified.

As a final consideration, one could think of using the approximation (3.19) for the pump power within the exact formula (3.7) of the DOA. As a consequence, the $\overline{\mathrm{DOA}}$ evaluated analytically remains almost unchanged with respect to that reported with solid line in Fig. 3.15, except for short fiber, where it follows exactly the numerical results (dot-dashed line in Fig. 3.15).

3.5 PMD-induced degradation of the NLP's performance

Until now I have considered a NLP device realized by a low-PMD optical fiber. In this section, I extend the study of the NLP to the case of fibers characterized by a large PMD coefficient. Results presented in this section were developed within a collaboration with research groups at Brescia University and and St. Petersburg University, and published in [45], where exhaustive numerical simulations of the NLP realized with fibers characterized by different PMD coefficients were performed, for several fiber length and signals powers. Here, I report some of those results to show how large PMD degrades the performance of the NLP device.

With a single propagating field, the primary effect of PMD is to introduce a stochastic delay, which depends on the SOP of the launched field, and whose range is quantified by the differential group delay (DGD) $\Delta\tau$ [67]. This is in turn a random quantity, with maxwellian distribution, whose root mean square value $\Delta\tau_{rms} = \mathrm{D_{PMD}}\sqrt{L}$ depends on the fiber length and the PMD coefficient. Although such an effect can be negligible for pulses whose duration is much larger than $\Delta\tau_{rms}$, another non-negligible effect of PMD occurs in a two channel (pump-signal) scenario, as the one that I am studying here. Indeed, the polarization of optical beams propagating at different wavelengths is subject to different amounts of birefringence. Hence, when two beams are launched into the fiber, the mutual position of their initial SOPs is not maintained along the fiber, and the SOPs eventually *diffuse* on the Poincaré sphere. As demonstrated, signal re-polarization occurs around the SOP of the input pump. For an effective performance of the NLP, it is thus necessary that, despite PMD, pump and signal polarizations evolve in the same way along the fiber.

Fig. 3.18 shows the dependence of the output signal DOP (dot-dashed lines) on the total walk-off delay T_d, as obtained by a NLP realized with a fiber characterized by a small PMD coefficient $\mathrm{D_{PMD}} = 0.05$ ps/km$^{1/2}$ (b), or a large PMD coefficient, $\mathrm{D_{PMD}} = 0.2$ ps/km$^{1/2}$ (c). In Fig. 3.18, the DOP is plotted along with the average $\overline{\mathrm{DOA}}$ (solid lines), measured between the output signal SOPs and the input pump SOP according to equation (1.37). As explained in Sec. 1.3.2, the difference between the two is related to the angular distance between the SOP towards which the signal is attracted and the reference pump SOP. Results are compared with the $\mathrm{DOP} = \overline{\mathrm{DOA}}$ case, obtained by a NLP realized with an (ideal) isotropic fiber, without PMD ($\mathrm{D_{PMD}} = 0$ ps/km$^{1/2}$), and reported in Fig. 3.18(a). In Fig. 3.18, I injected into the NLP Gaussian signal pulses with peak power $P_s = 1$ W and full-width half-maximum (FWHM) equal to 12.5 ps. Moreover, the fiber employed here, with length $L = 20.8$ km, is characterized by a nonlinear Kerr coefficient $\gamma = 1$ W^{-1}km^{-1} and

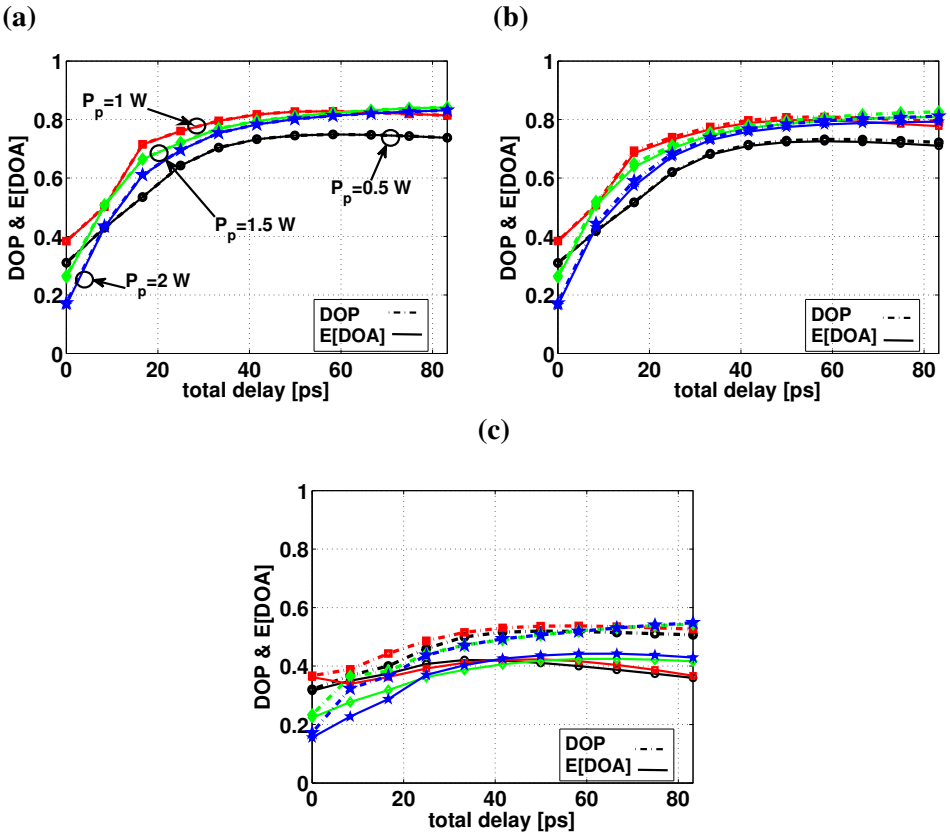

Figure 3.18: Degree of polarization (DOP) (dashed lines) and average degree of attraction ($\overline{\text{DOA}}$) (solid lines) as a function of total delay, in the case of "modern" fibers, with a small PMD coefficient $D_{\text{PMD}} = 0.05$ ps/km$^{1/2}$(b), or "legacy" fibers, with a large PMD coefficient $D_{\text{PMD}} = 0.2$ ps/km$^{1/2}$ (c). Results are compared with those obtained in the case of (ideal) isotropic fibers (a). Different curves are obtained with different pump powers $P_p = 0.5$ W; 1 W; 1.5 W; 2 W (identified by the following symbols, in order: circle, square, diamond, star).

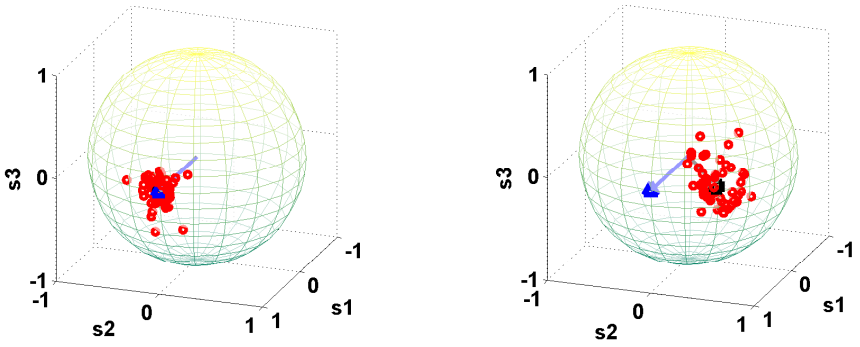

Figure 3.19: Distribution of 50 (initially) random signal SOPs after the NLP with a 20.8 km long fiber, with the pump power $P_p = 2$ W and the input pump SOP on $\hat{s}_1$ (see plots). Without PMD (left), the SOPs surround the pump SOP, which acts as the attraction SOP. With large PMD (right), the attraction SOP $\frac{E\left[\left\langle \vec{s}_s(t)\right\rangle\right]}{\left\|E\left[\left\langle \vec{s}_s(t)\right\rangle\right]\right\|}$ no longer coincides with the pump SOP.

dispersion parameter D = 1 ps/nm/km. Different curves in Fig. 3.18 correspond to different values of the pump power P_p, equal to 0.5 (black, with dots), 1 (red, with squares), 1.5 (green, with diamonds) and 2 W (blue, with stars).

Comparing Fig. 3.18(b) and Fig. 3.18(a), we barely see any difference: the basic reason being that D_{PMD} is sufficiently small to guarantee an almost identical evolution of pump and signal polarizations along the fiber, as it happens in fibers without PMD. On the other hand, when comparing results in Fig. 3.18(c) with those in Fig. 3.18(a), it can be seen that the NLP performance, in terms of DOP is spoiled (i.e., decreased by 0.25) by PMD in the best cases of repolarization, i.e., those with a large walk-off delay. One thing to note in Fig. 3.18(c), when compared with Fig. 3.18(a), is that here DOP and $\overline{\text{DOA}}$ do not coincide any more, hence the signal SOPs is attracted towards an attracting SOP that differs from the input pump SOP. I shall discuss shortly hereafter the reason for this behavior.

Fig. 3.19 compares the output SOPs (red, dots) that are obtained for 50 launched pulses (with their initial SOPs uniform on the Poincaré sphere), after a NLP composed of a single randomly birefringent fiber sample, in the case of no PMD (left) or with a large PMD coefficient $D_{PMD} = 0.2$ ps/km$^{1/2}$ (right). The pump power is $P_p = 2$ W and the walk-off delay is 83 ps: hence the operating conditions are those on the right edge of the (blue) lines with star symbols in Fig. 3.18(a) (no PMD)

and 3.18(c) (large PMD), respectively. The pump SOP is linear horizontal ($\hat{s}_p = \hat{s}_1$), which is reported as a (blue) triangle in Fig. 3.19. The linear birefringence of the fiber has been equalized, before plotting Fig. 3.19, so that output signal SOPs are plotted in the input frame of reference. Hence the difference between the input pump SOP and the attraction SOP $\frac{E\left[\left\langle \vec{s}_s(t)\right\rangle\right]}{\left\|E\left[\left\langle \vec{s}_s(t)\right\rangle\right]\right\|}$, which is reported as a (black) square in Fig. 3.19, can be appreciated. The difference between the two plots in Fig. 3.19 is a graphical representation of the reason why the output signal DOP and $\overline{\text{DOA}}$ may not coincide. In fact, as analytically demonstrated in chapter 1, $\overline{\text{DOA}}$ and DOP only coincide whenever the attraction SOP is constantly parallel to the pump SOP (see (1.38)), as is obviously the case of Fig. 3.19(left), where PMD is absent. This is what happens in Figs. 3.18(a)-3.18(b), with no or little PMD, while in Fig. 3.18(c) it is always $\overline{\text{DOA}} <$ DOP. This is especially true for larger walk-off delays, where a larger wavelength spacing between pump and signal brings about a stronger depolarization due to PMD.

The values of the DOP and the $\overline{\text{DOA}}$ reported in Figs. 3.18(b)-3.18(c) are averaged over different fiber realizations, to take into account the random nature of PMD. Although one would need thousands of fiber samples to properly statistically characterize a pool of randomly birefringent fibers, to limit simulation time to reasonable levels I only tested 10 fibers. However I also report here the standard deviation σ_{DOP} of the DOP values which were obtained from these fiber samples. In Fig. 3.18(c), with large PMD, the standard deviation reaches the highest value ($\sigma_{\text{DOP}} = 0.24$) for the largest walk-off delays (83 ps). Hence, the DOP which is reported in Fig. 3.18(c) is the mean of fiber samples which exhibit strong statistical oscillations that depend on the specific sample, as is typically the case in the presence of PMD. On the contrary, fibers with a small PMD coefficient are subject to little variability and induce much smaller fluctuations on the obtained DOP values: in the case of small PMD, the mean DOP is plotted in Fig. 3.18(b) and σ_{DOP} is at most of the order of 0.01, for all tested walk-off delays. The standard deviation of the DOP values is of course zero, in the case of Fig. 3.18(a), where PMD is not present.

3.6 Polarization attraction with multiple-pumps

Despite the NLP device designed in the co-propagating configuration is more power efficient with respect to the counter-propagating NLP, to generate an effective polarization attraction of the signal SOP, powerful pump laser emitting few hundreds of milliwatts, are needed. The use of such a pump could be a problem, especially if a

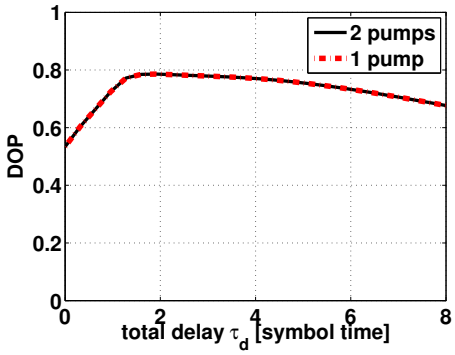

Figure 3.20: Performance of the nonlinear lossless polarizer as a function of the normalized walk-off delay τ_d. (solid) DOP obtained by employing two pump lasers with equal powers P_p and placed at the same wavelengths λ_p; (dot-dashed) DOP obtained by employing a single pump laser with power $2P_p$ and placed at λ_p.

single mode laser is needed, since it could be quite expensive. As a feasible solution of such a (possible) issue, I propose to replace the powerful pump laser with two (or more) pump lasers, less powerful and then less expensive. Thus, in this section I study the effectiveness of lossless polarization attraction, generated by the interaction between the signal and two (or more) pump lasers, with the same polarization. Results reported here represent a "proof of principle" for a *multi-pump NLP* device, since they are early results that need further investigations.

3.6.1 Pumps placement for a multi-pump NLP

I simulated numerically a co-propagating NLP as shown in Fig. 3.1, where, instead of a single pump laser with power $P_p = s_{0p}$, I injected two pump lasers, with the same power $P_{p1} = P_{p2} = P_p$ and linear-horizontal SOPs, i.e., $\hat{s}_{p1} = \hat{s}_{p2} = \hat{s}_1$. I considered a low-PMD fiber ($\mathrm{D_{PMD}} = 0.05$ ps/km$^{1/2}$) with length $L = 20$ km, so that the signal SOP is attracted towards the input pump SOP (as shown in Sec. 3.5). Moreover, the input signal peak power is $P_s = s_{0s} = 200$ mW. I assume the two pump lasers placed at the wavelengths λ_{p1} and λ_{p2}, so that the wavelength displacement between the signal and the two pumps are $\Delta\lambda_1 = |\lambda_{p1} - \lambda_{zdw}|$ and $\Delta\lambda_2 = |\lambda_{p2} - \lambda_{zdw}|$, respectively. Hence, the total walk-off delay between the signal and the two pump lasers are $T_{d1} = \mathrm{D}\Delta\lambda_1 L$ and $T_{d2} = \mathrm{D}\Delta\lambda_2 L$, respectively.

Fig. 3.20 shows the output signal DOP as a function of the total walk-off T_d, nor-

malized with respect to the pulse duration T_s, i.e., as a function of τ_d. Solid (black) curve, in Fig. 3.20, is obtained by injecting two pump lasers placed, in the present case, at the same wavelength $\lambda_{p1} = \lambda_{p2} = \lambda_p$, so that they lie at the same wavelength displacement $\Delta\lambda_1 = \Delta\lambda_2 = \Delta\lambda$ from the signal. Thus, the normalized walk-off between the signal and the two pump lasers is the same, hence $\tau_{d1} = \tau_{d2} = \tau_d$. Moreover the pump lasers have the same power $P_p = 100$ mW, in Fig. 3.20, so that the overall pump power (200 mW) is equal to the signal peak power. With these parameters, solid (black) curve perfectly overlaps with the dot-dashed (red) curve, which represents the DOP obtained by injecting a single pump laser with power 200 mW, placed at $\lambda_p = \lambda_{zdw} + \Delta\lambda$. Such a curve is thus that reported in Fig. 3.2(b) and is used as a reference for the multi-pump NLP performance. As guessed, the effectiveness of LPA generated by one or two pump lasers is the same, since the wavelength displacement and the overall pump power is the same, in the two cases, hence the signal SOP evolves in the same way in both the configurations of the NLP.

To thoroughly investigate the effectiveness of LPA generated by means of two pump lasers, I separately varied the pumps wavelengths, λ_{p1} and λ_{p2} (within the C-band), so as to test different values of the normalized walk-off τ_{d1} and τ_{d2}. Results are plotted in Figs. 3.21, which show the output signal DOP as a function of the normalized walk-off, τ_{d1} and τ_{d2}, between the signal and the two pump lasers. Note that the negative (positive) values of the normalized walk-off indicate that the pump velocity is slower (faster) than the signal velocity. When the normalized walk-off have the same sign, i.e., for values of τ_{d1} and τ_{d2} within the first or third quadrant in Figs. 3.21, both the pump lasers were placed on the same side, with respect to the signal wavelength, hence they are both placed at larger or smaller wavelengths, with respect to λ_{zdw}. On the other hand, when the normalized walk-off have opposite signs, i.e., for values of τ_{d1} and τ_{d2} within the second or fourth quadrant in Figs. 3.21, pumps were placed at the opposite side with respect to the signal wavelength, hence one pump laser was placed at a larger wavelength while the other at a smaller wavelength, with respect to λ_{zdw}. I call the two schemes described above as *asymmetric* or *symmetric* configuration, schematically depicted in Fig. 3.22(left) and (right), respectively. In Figs. 3.21, the power of each pump lasers is $P_p = 50$ mW (a), $P_p = 100$ mW (b), $P_p = 200$ mW (c) and $P_p = 400$ mW (d), respectively.

All plots in Figs. 3.21 show that, when the pumps were placed in the *asymmetric* configuration, the effectiveness of LPA is more robust, with respect to the pumps wavelengths variations, than the case when the pumps were placed as in *symmetric* configuration. In fact, with the *asymmetric* pumps configuration (first or third quadrant), the signal DOP remains high for a wider range of walk-off values, compared

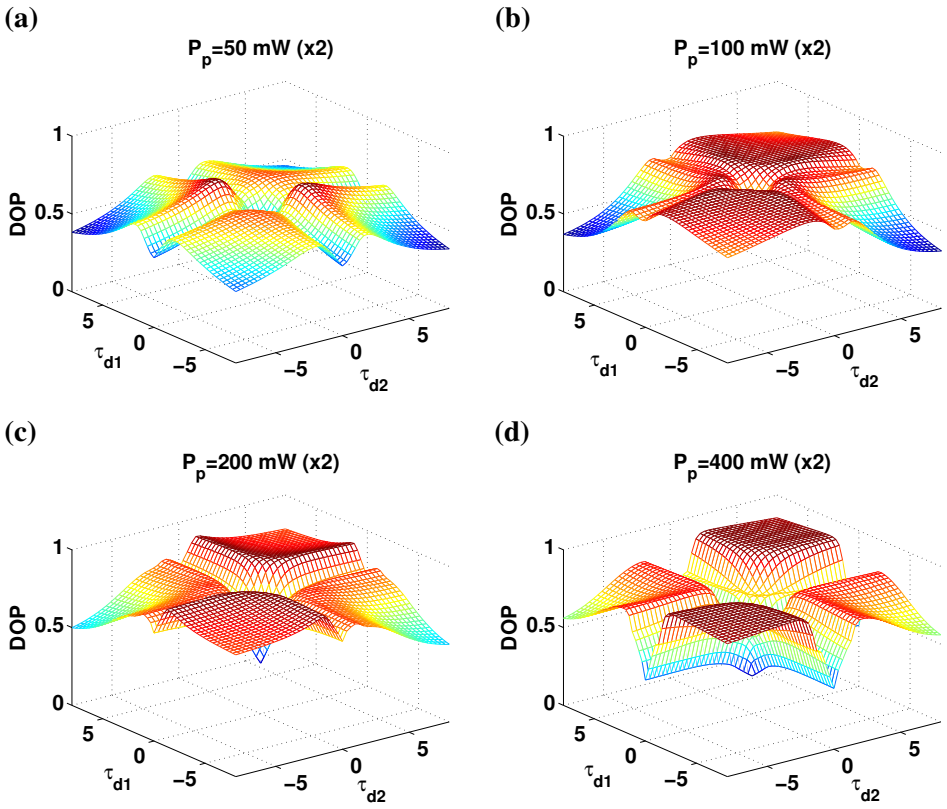

Figure 3.21: Degree of polarization (DOP) as a function of the normalized walk-off τ_{d1} and τ_{d2} between the signal and the two pump lasers, for different values each pump power.

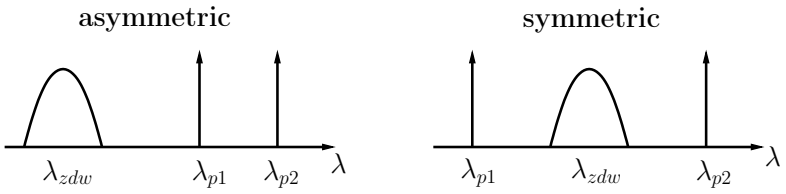

Figure 3.22: Signal and pumps placement. (left) asymmetric configuration: both pump lasers are placed at the same side with respect to the signal. (right) symmetric configuration: signal is placed in between the pump lasers.

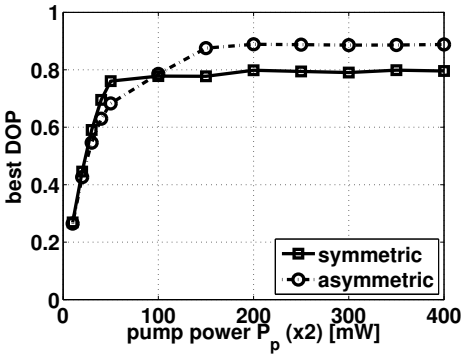

Figure 3.23: Best values of the degree of polarization (DOP) as a function of the pump lasers power. Comparison between the *asymmetric* and *symmetric* pump configurations.

with the *symmetric* pumps configuration (second or fourth quadrant). Moreover, with increasing pump lasers power, the area in the plane (τ_{d1}, τ_{d2}), where an high DOP is obtained, increases more and more, hence the "polarization attraction interval" increases. Regarding the best output signal DOP obtained with the tested pump powers, the better NLP performance is always obtained with the *asymmetric* pumps configuration, except for the lowest power tested ($P_p = 50$ mW): in Fig. 3.21(a), where the best DOP is obtained with the *symmetric* pumps configuration. For all the tested pump powers, the best DOP reached by each pumps configuration (*asymmetric* or *symmetric*), is obtained when the normalized walk-off values are equal to each other, regardless of their signs, hence when $|\tau_{d1}| = |\tau_{d2}|$.

The best output signal DOP, that can be obtained with the *asymmetric* or *symmetric* pumps configuration, is plotted in Fig. 3.23 as a function of the pump laser power P_p. The NLP realized with an *asymmetric* pump configuration always shows better performance than that realized with the *symmetric* pump configuration, except for power levels $P_p < 100$ mW. For both NLP configurations, the best DOP saturates to a maximum value, by increasing the pump power levels, that is DOP $\simeq 0.8$ with the *symmetric* configuration, or DOP $\simeq 0.9$ with the *asymmetric* configuration. This means that, for the system parameters employed here with pump lasers power higher than $P_P = 150$ mW, the performance of the NLP device, in terms of DOP, would not be increased, while the "polarization attraction interval" would be.

From Figs. 3.21 and Fig. 3.23, it is thus clear that in designing a *multi-pump* NLP device, the two pump power lasers must be placed on the same side with respect to

the signal wavelength (*asymmetric* pump configuration).

3.6.2 Pump with distributed power

Returning to Figs. 3.21 and considering the case when the pumps were placed as in *asymmetric* configuration, all plots show that the DOP decreases faster when both pumps are moved away from the signal (e.g., when both τ_{d1} and τ_{d2} increase) with respect to the case when only one pump laser is moved away from the signal, while the other is held still (e.g., when τ_{d1} increases while τ_{d2} is fixed).

This means that LPA is equally effective when both the pump lasers are placed at the same (optimal) wavelength (i.e., when $\lambda_{p1} = \lambda_{p2} = \lambda_p^*$) or when one of the lasers is placed at the (optimal) wavelength, while the other can be placed at any distance from the signal (in the range tested here). Moreover, I have demonstrated in the previous section that the NLP performance obtained with a single laser or with two lasers does not change, provided that two lasers were placed at the same wavelength and the overall pump power is preserved. Such considerations suggest that, by iterating the reasoning above with more than two pump lasers, one can obtain the same effectiveness of LPA as by injecting into the NLP either a single powerful pump laser or a series of (co-polarized) pump lasers much less powerful and distributed on a wide-bandwidth. By taking a last logical step, the series of (co-polarized) lasers distributed on a wide-bandwidth could be seen as a fully-polarized wide-bandwidth source, whose frequency components are uncorrelated. Hence, in this section I propose a first numerical demonstration of the NLP device realized with a pump whose power, instead of being concentrated on a single frequency (laser), is distributed on a large bandwidth (wide-bandwidth source).

As a first step, I compare the NLP effectiveness obtained with a single powerful pump laser or with a series of (co-polarized) pump lasers much less powerful and distributed on a wide-bandwidth. Results are plotted in Fig. 3.24, which shows the DOP of the output signal as a function of the number of pumps injected into the NLP, for three values of the bandwidth ($B_{i\%}$) within which the laser were distributed. The bandwidth values $B_{i\%}$ reported in Fig. 3.24, are defined as the wavelength displacement between the two pump lasers, $B_{i\%} \triangleq |\lambda_{p2} - \lambda_{p1}|$, such that the DOP decreases by $i\%$ with respect to the best DOP obtainable by injecting a single pump laser, placed at the optimal wavelength λ_p^*. Operatively, to obtain $B_{i\%}$ I selected, for a fixed overall pump power, the optimal pump wavelength λ_p^* that maximize the DOP with a single pump laser. Then, by injecting two pump lasers (with the same overall power), I placed the first laser at $\lambda_{p1} = \lambda_p^*$, while I varied the wavelength of the second laser, λ_{p2}, so that to obtain the values of $B_{i\%}$ searched. Then, as the number of pumps n

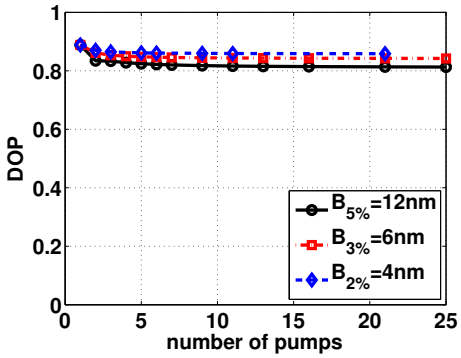

Figure 3.24: Degree of polarization (DOP) as a function of the pumps number n. Each pump has a power $P_{pi} = P_p/n$, where $P_p = 400\,mW$ is the overall pumps power. Pumps are placed equidistantly within a bandwidth $B_{i\%}$, hence pumps wavelengths displacement $B_{i\%}/(n-1)$.

increases, I placed the lasers at equidistant wavelengths $B_{i\%}/(n-1)$ within the bandwidth $B_{i\%} = \left|\lambda_{p2} - \lambda_p^*\right|$.

As an example[5], in Fig. 3.24 the overall pump power is $P_p = \sum_{i=1}^{n} P_{pi} = 400$ mW, where $P_{pi} = P_p/n$ is the power of each laser, so that $\lambda_p^* = \lambda_{zdw} + 2.8$ nm, while the three curves correspond to the bandwidths $B_{5\%} = 12$ nm, $B_{3\%} = 6$ nm and $B_{2\%} = 4$ nm. Curves in Fig. 3.24 show that the signal DOP settles down to a value always larger than 0.8 by increasing the pumps number, hence by decreasing the power of each pump until a minimum power $P_{pi} = 16$ mW. Thus, I demonstrated that the NLP can work also with pump whose power is a wide bandwidth. Moreover, when the pump lasers are distributed on a smaller bandwidth, the value of the DOP floor increases; as a result, there is a bandwidth $B_{0\%}$ such that, if the pump lasers are distributed in that bandwidth, the DOP remains constant and equal to the best DOP obtainable.

As stated above, as a second step, it should be demonstrated that the series of (co-polarized) lasers distributed on a wide-bandwidth could be seen as a fully-polarized wide-bandwidth source, whose frequency components are uncorrelated. As an examples of such a sources, one could consider a light emitting diode (LED) source or a noise source (e.g., ASE noise source), filtered through an ideal polarizer in order to make them fully-polarized. Such an issue is under investigation. Note however that

[5]The values of the bandwidths reported here refer to an input signal with duration $T_s = 100$ ps.

a noise source has been used by Guasoni *et al.* in [68], to experimentally realize an all-fiber based chaotic polarization scrambler, hence a device that makes a sort of "inverse function" with respect to the NLP device[6].

[6]In the chaotic polarization scrambler, a fully-polarized signal (nonlinearly) interacts with a depolarized pump (noise source, in [68]), so that to obtain a depolarized output signal.

Chapter 4

LPA of telecom signals: application to all-optical OSNR enhancement

Despite the growing interest in studying lossless polarization attraction (LPA), manifested by the scientific community, few other applications of the nonlinear lossless polarizer (NLP) have been proposed so far, beside repolarization. In this framework, interesting applications include the all-optical nonlinear processing and regeneration of a 40 Gb/s modulated telecom signal [47], the design of optical flip-flop memories [49], the realization of an all-optical fast chaotic polarization scrambler [68] and the enhancement of the optical signal-to-noise ratio (OSNR) of a telecom signal [50–53]. I focus in particular upon the latter application, that I shall hereafter refer to as *noise cleaning*, introduced by our research group, for the first time [50]. In particular, I have shown that an all-optical *noise cleaner* device is able to almost double the OSNR of a telecom signal [53]. Such a device can be implemented based on a NLP in one of the two configurations mentioned above. Noise cleaning based on a counter-propagating NLP (see chapter 2) has proven to be effective for telecom signals whose SOP does not change across many (thousands) consecutive bits, i.e., where the *polarization coherence time* is of the order of the whole bit-packet. On the contrary, using a NLP in the co-propagating configuration (see chapter 3), the noise cleaning capabilities extend to telecom signals whose polarization coherence time is as short as the bit period.

In this chapter, I present a comprehensive picture of a noise cleaner based on NLP, in both configurations. I shall compare the two solutions, with counter- and co-

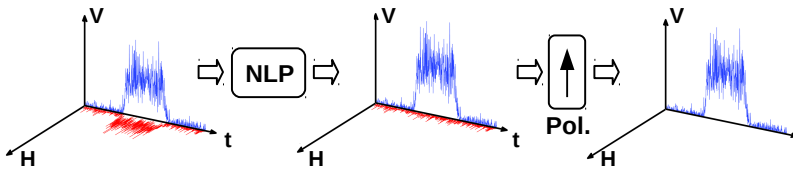

Figure 4.1: Principle of operation of a noise cleaner based on a nonlinear lossless polarizer.

propagating pump, for signals with a fast or slowly varying SOP. Moreover, I shall quantify the performance of the proposed noise cleaner through the traditional notion of noise figure F and measure OSNR according to the standard method described by ITU-T [69]. Finally, I propose a method to theoretically estimate the OSNR gain achieved by the noise cleaner.

4.1 Principle of operation

The idea behind the noise cleaning approach is that, when a polarized signal is affected by unpolarized additive white Gaussian noise (AWGN), such as the amplified spontaneous emission (ASE) noise, one can get rid of the orthogonally polarized noise component, by filtering through an ideal polarizing filter, aligned with the signal SOP. In the general case, the noiseless signal component is partially (de-)polarized. Hence, in order to obtain an OSNR enhancement, the noiseless signal should first be repolarized towards a unique SOP, coinciding with the transparent eigenstate of the polarizing filter, before passing through it. Otherwise, the polarization fluctuations of the signal would be transformed into intensity fluctuations, leading to a further degradation of the OSNR. I can thus employ a NLP, before the polarizing filter, whose task is to attract the signal SOP (unknown and time-varying, in general) towards the transparent eigenstate of the ideal polarizing filter.

A two-stage device results, as schematically depicted in Fig. 4.1, where the first stage is a NLP, able to control the signal SOP, and the second stage is an ideal polarizing filter (*Pol.*). The three plots in Fig. 4.1 show how the optical power of the input signal, initially split between the horizontal (red) and vertical (blue) polarization components, is attracted by the NLP towards, e.g., the vertical polarization. This is assumed to be the transparent SOP of the *Pol.*, so that the vertically polarized optical power passes through the filter unattenuated, while the orthogonally (horizontally) polarized optical power is filtered out. A similar picture holds for any attracting

SOP (hence for any input pump SOP), provided that the attracting SOP of the NLP coincides with the transparent SOP of *Pol.*, i.e., that the NLP and *Pol.* are properly aligned. One possible method to achieve such an alignment is to rotate the orientation of *Pol.*, e.g., by using a polarization controller, so that the average power at the output of *Pol.* is maximized. Otherwise, such an alignment could be achieved also by changing the input pump SOP, while maintaining the orientation of *Pol.* fixed. In the following of this chapter, however, I will assume that the alignment between NLP and *Pol.* is ensured, without further discussing the possible techniques to meet this condition.

If the noiseless signal component is effectively attracted by the NLP, while the unpolarized noise component is not, the resulting OSNR is enhanced. Since signal repolarization is detrimental, if applied to polarization multiplexed formats [53], in the following, I shall concentrate on signals with a "legacy" binary amplitude modulation format, i.e., on-off keying (OOK), modulated at $R = 10$ Gb/s.

It has been shown that NLPs realized in a counter-propagating configuration or in a co-propagating configuration are characterized by different *transient times*; in all cases, they provide an effective LPA only for input signals whose SOP is stable for a period larger than their transient time. Despite possible depolarization effects — such as linear polarization mode dispersion (PMD) or nonlinear XPolM, suffered by the signal along the transmission channel — the *coherence time* of the noiseless signal SOP is typically much larger than that of unpolarized noise. Hence, a NLP can be designed so as to effectively act only on the noiseless signal component and not on the noise. The proposed device thus exploits a novel approach, to discriminate noise power from signal power, based on polarization rather than on frequency, as is typical of optical band pass filters (OBPF) that are present at the front-end of an optical receiver. A fundamental difference between the two approaches is that the noise cleaner is able to mitigate not only the noise power outside the signal bandwidth, but also that within the signal bandwidth, while preserving the signal power.

Assuming an ideal behavior of the NLP, the SOP of the noiseless input signal component would be attracted towards the transparent eigenstate of *Pol.* and pass through it without any power loss, while unpolarized noise would not be attracted and remain unpolarized, so that half of its power would be suppressed by *Pol.*. I am thus tempted to conclude that the noise cleaner can increase the OSNR by 3 dB, which is then the theoretical maximum OSNR gain achievable by the device in Fig. 4.1. **This is however the application of a linear reasoning to a nonlinear device**, where the superposition of effects does not hold, hence the noise cleaner performance has to be directly verified. In the following, I numerically evaluate the noise cleaner

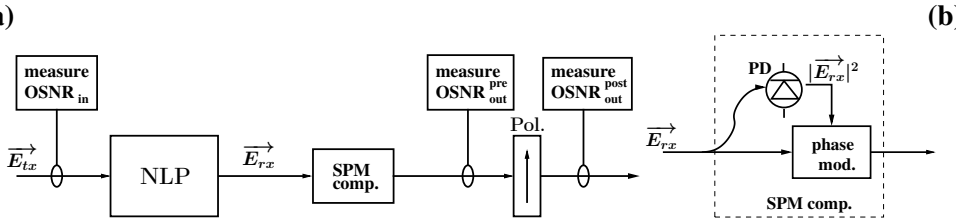

Figure 4.2: (a) Noise cleaner setup, composed by a nonlinear lossless polarizer (NLP) followed by an ideal polarizer filter (*Pol.*); (b) schematic of the SPM compensating subsystem, used here to ease the output OSNR measurements.

performance, as obtained in different scenarios.

4.2 System setup and simulation parameters

Fig. 4.2(a) shows the proposed noise cleaner setup, that I numerically simulated. The first section is a NLP, where a fully-polarized CW pump laser, with power P_p, is coupled with the input signal, so as to attract the signal SOP towards the pump SOP. The NLP can be realized in the counter-propagating configuration (see chapter 2), or in the co-propagating configuration (see chapter 3). In both cases, the NLP includes a $L = 20$ km long dispersion-shifted fiber (DSF), with attenuation $\alpha = 0.2$ dB/km, Kerr coefficient $\gamma = 1.99$ W^{-1}km^{-1} and PMD coefficient $\mathrm{D_{PMD}} = 0.05$ ps/km$^{0.5}$ (so that propagation is governed by the Manakov equation).

As recalled in Sec. 4.1, the two NLP configurations are characterized by different transient times, hence are suitable for input signals with different polarization coherence times. I numerically simulated the noise cleaner in Fig. 4.2 by injecting input signals with different polarization coherence times, power and duration. In all cases, the input signal was placed at the fiber zero dispersion wavelength (λ_{zdw}) and is represented by the (lowpass equivalent) Jones vector $\overrightarrow{E}_{tx}(t) = \overrightarrow{A}_{tx}(t) + \overrightarrow{W}(t)$, where the noiseless input $\overrightarrow{A}_{tx}(t)$ is an intensity-modulated telecom signal with a fixed mean power P_s, while $\overrightarrow{W}(t)$ is unpolarized AWGN, modeling ASE noise, whose power P_w is varied so as to test different values of $\mathrm{OSNR_{in}} = P_s/P_w$. For the practical values of $\mathrm{OSNR_{in}}$ tested here (larger than 10 dB) the overall power, hence the amount of nonlinear distortion, is effectively dictated by signal power, and not by noise power.

The signal output by the NLP is $\overrightarrow{E}_{rx}(t) = \overrightarrow{A}_{rx}(t) + \overrightarrow{N}(t)$, where noise $\overrightarrow{N}(t)$ is no longer white. As further discussed in Sec. 4.4, colored noise makes the measure-

ment of the output OSNR sensitive to the bandwidth of the signal spectrum, which is broadened by Kerr distortions, during nonlinear propagation. While XpolM is the driving force of LPA, self- and cross-phase modulations (SPM, XPM) are irrelevant for LPA. Being the pump CW, XPM just yields a constant phase shift, while SPM produces a spectral broadening of the signal. The last Kerr distortion is degenerate four-wave mixing (FWM), which is negligible, for the parameter values used here, as I numerically verified (see chapter 3). The purpose of the "SPM Comp." subsystem in Fig. 4.2(b) is to remove the SPM-induced spectral broadening, in order to ease OSNR measurement. The task of equalizing SPM distortions, that is normally unfeasible in the analog domain, can be accomplished here by a phase modulator driven by the photodetected (PD) signal intensity [70], since chromatic dispersion is absent at the signal wavelength λ_{zdw}.

The output OSNR was measured before ($\mathrm{OSNR}_{\mathrm{out}}^{\mathrm{pre}}$) and after ($\mathrm{OSNR}_{\mathrm{out}}^{\mathrm{post}}$) the polarizing filter *Pol.*, as shown by the blocks in Fig. 4.2(a). In all simulations I ensured that, as remarked in Sec. 4.1, the pump SOP and the transparent eigenstate of *Pol.* are aligned to each other, so that only the attracted portion of signal (and noise) passes through the filter and contributes to the measurement of $\mathrm{OSNR}_{\mathrm{out}}^{\mathrm{post}}$.

4.3 Polarization control of a noisy signal

Unpolarized noise degrades the degree of polarization (DOP) of the input signal, hence can spoil the mutual time-coherence of pump and signal SOPs, which is a necessary prerequisite for LPA. Although the performance of NLPs has been characterized as a function of system parameters [34,41,45,46], few studies account for the presence of noise in the attracted signal [47,53]. Thus, I analyzed the performance of a NLP, in the presence of noise, in both counter- and co-propagating configurations, for input signals characterized by a polarization coherence time that is either "long", i.e., of the order of a bit-packet (*packetwise polarized signals*), or "short", i.e., of the order of a single bit (*bitwise polarized signals*). Hence, referring to a "legacy" bit-rate of 10 Gb/s, the polarization coherence time ranges between 100 ps (a single bit period) and about 1 μs (a long Ethernet packet of 10^4 bits).

4.3.1 Packetwise polarized signals (slowly-varying SOP)

I first analyze the NLP effectiveness in controlling the SOP of an amplitude modulated optical signal characterized by a "slowly-varying" SOP, i.e., of a packetwise polarized signal, whose polarization is constant over the entire packet. For these signals,

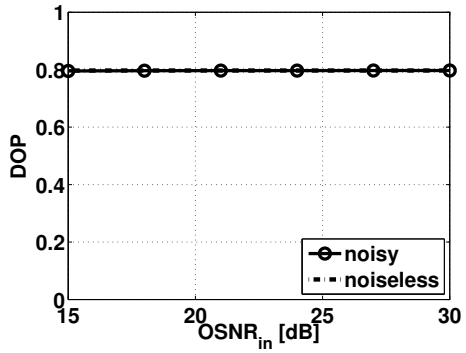

Figure 4.3: Performance of a counter-propagating NLP, obtained for packetwise polarized signals.

a NLP designed in the counter-propagating configuration has already been proven to be effective in controlling the signal SOP in a noiseless scenario (see chapter 2).

As demonstrated in chapter 2, the repolarization obtained by a counter-propagating NLP on an intensity-modulated, fully-polarized bit packet, with mean power P_s, is the same as that obtained on an input signal consisting of a single polarized pulse, with the same energy and power P_s. I set the pulse duration to $T_s = 1$ μs (the same as used in chapter 2), so that it is representative of a packet of 10^4 OOK bits (@10 Gb/s). I set the pump SOP as linear-horizontal (the same results are obtained for any other pump SOP, as verified), to which the polarizing filter *Pol.* in Fig. 4.2(a) is aligned, while the input signal SOP is varied for each transmitted packet, so that, statistically, it uniformly covers the Poincaré sphere. To avoid packet-to-packet nonlinear interactions mediated by the pump, I assume that only one packet travels into the NLP at a time.

In order to obtain an effective attraction of the noiseless signal, with a counter-propagating NLP, powerful signals are needed. Exploiting a property of LPA, whose performance roughly depends on the product between signal and pump power (see chapter 2), I employed strongly unbalanced power levels. In order to limit SPM, I set the signal mean power to $P_s = 0.6$ W, much less than the pump power $P_p = 2.4$ W.

Simulation results, reported in Fig. 4.3, show that a significant DOP $\cong 0.8$ is reached, at the output of the NLP, for a noiseless input signal, plotted as a reference, with a dot-dashed line. The (superimposed) solid line with symbols represents the DOP obtained for a noisy input signal, as a function of $\mathrm{OSNR}_{\mathrm{in}}$, in a range of practical interest. Results clearly show that the control of the signal SOP performed by the NLP is not spoiled by the presence of additive noise, hence an effective perfor-

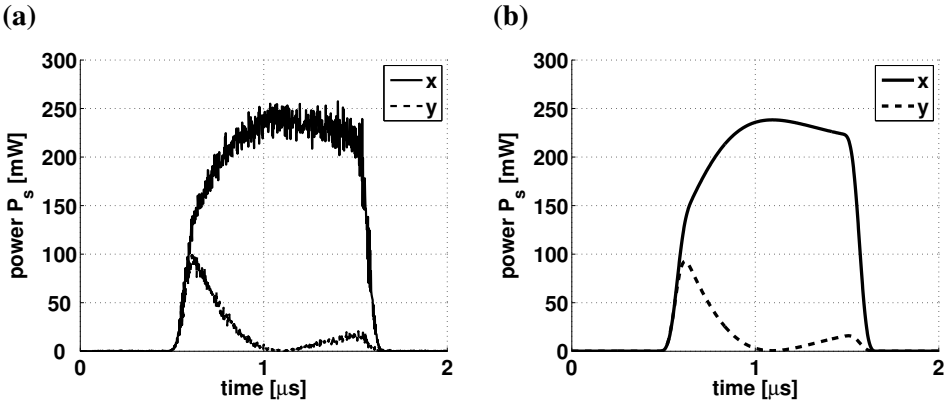

Figure 4.4: Power profile of the noisy (a) or noiseless (b) signal, at the output of the NLP. The input signal is right-circularly polarized ($\hat{s}_3$), while the input pump is linearly-horizontal polarized ($\hat{s}_1$), hence aligned with the x polarization.

mance of the noise cleaner can be expected, at least for the $\mathrm{OSNR}_{\mathrm{in}}$ values tested here. A further decrease of the $\mathrm{OSNR}_{\mathrm{in}}$, below 15 dB, would result in a gradual DOP degradation, due to the addition of unpolarized noise, as demonstrated in [50]. For each DOP value in Fig. 4.3, simulation results were averaged over 100 random input packet SOPs and 10 random noise realizations. Counter-propagation of signal and pump was numerically solved using the SCAOS algorithm (see chapter 2) [44].

As a further demonstration of the effectiveness of the NLP in the presence of noise, Fig. 4.4 shows the power profile of the noisy signal (a) at its output (before the *Pol.*), compared with the power profile of the noiseless signal (b). Here, as an example, the input signal is right-circularly polarized ($\hat{s}_3$), hence the input (noiseless) signal power is equally distributed between the two orthogonal polarizations x and y. This is no longer true at the output of the NLP (Fig. 4.4), where the signal power is almost entirely aligned with the x polarization, being the pump linearly-horizontal polarized ($\hat{s}_1$). As clearly seen in Fig. 4.4, the temporal dynamic with which the pulse power is attracted towards the x polarization is almost the same for both the noisy (a) or noiseless (b) signal. The noisy signal appears as if the unpolarized noise were added to its noiseless component after LPA takes place, although this is not the case, being the NLP a nonlinear device.

As already stated, the effectiveness of the counter-propagating NLP does not extend to signals with polarization coherence times much shorter than a microsecond, because of the longer transient time of the LPA process, as shown in chapter 2.

4.3.2 Bitwise polarized signals (fast-varying SOP)

Given the severe performance degradation of a counter-propagating NLP in controlling the SOP of a short packet, i.e., of an input signal whose duration is shorter than the transient time of the NLP, I cannot expect any gain on the OSNR of such signals, from the noise cleaner with the counter-propagating NLP. A solution is to implement the NLP in the co-propagating geometry, that has been proven able to control the SOP of signals with duration as short as the bit period (see chapter 3). In order to verify its potentials, I evaluated its performance for modulated bit packets whose polarization coherence time is of the order of one bit period, hence for bitwise polarized signals. In numerical simulations, the transmitted noiseless signal $\overrightarrow{A}_{tx}(t)$ consisted of a stream of 2560 bits with OOK modulation at 10 Gb/s ($T_p = 256$ ns), with a random SOP for each OOK pulse, uniformly distributed over the Poincaré sphere, so that the input DOP is zero.

In chapter 2, I have shown how packet-to-packet nonlinear interactions mediated by the pump are detrimental for the repolarization of consecutive packets. Similarly, for bitwise polarized signals, the bit-to-bit nonlinear interactions mediated by the pump are detrimental for the co-propagating NLP performance and I should avoid them. To do so, I chose a return-to-zero (RZ-OOK) modulation format, so as to introduce a guard interval between two consecutive OOK pulses. Moreover, as demonstrated in chapter 3, the effectiveness of a co-propagating NLP is maximized when the walk-off delay between signal and pump is roughly twice the signal pulse duration. In order to satisfy both conditions above, I chose a RZ-OOK format with duty-cycle 33%. Hence, in the simulation results that follow, each bit is encoded on a pulse with duration $T_s = 33.3$ ps, and a nearly optimal walk-off $T_d = 64$ ps can be reached by properly selecting the pump wavelength. Furthermore, $T_s + T_d$ is less than the bit-period ($T_b = 100$ ps), which guarantees the absence of nonlinear pulse-to-pulse interactions mediated by the pump.

Fig. 4.5(a) shows the DOP of the output noisy signal $\overrightarrow{E}_{rx}(t)$ as a function of $\mathrm{OSNR}_{\mathrm{in}}$ (solid line with symbols). Results were obtained by setting the pump power at $P_p = 0.4$ W and the signal mean power at $P_s = 33.3$ mW (peak power equal to 200 mW). **The overall transmitted power is almost an order of magnitude lower than the one transmitted in Sec. 4.3.1, which confirms again the superior power efficiency of the co-propagating NLP configuration**. The DOP obtained for a noiseless input signal, equal to 0.86, is plotted along, as a reference (dot-dashed line). For lower $\mathrm{OSNR}_{\mathrm{in}}$ values, the decrease of the output DOP demonstrates a degradation of the NLP effectiveness. As was already observed for a counter-propagating NLP [50], part of the decrease of DOP is a trivial consequence of the addition of unpolarized

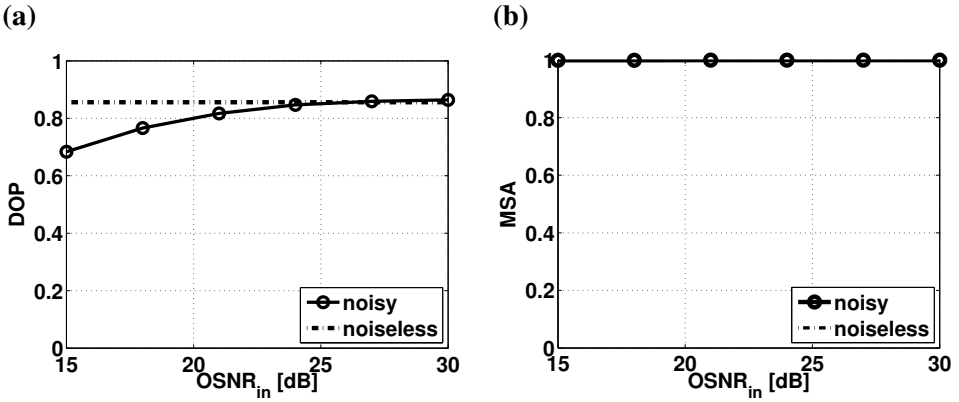

Figure 4.5: Performance of an optimized co-propagating NLP, obtained for bitwise polarized signals (as well as for longer polarization coherence times): (a) degree of polarization (DOP); (b) mean SOP attraction (MSA).

noise at the input. To demonstrate this assertion, I report in Fig. 4.5(b) the mean SOP attraction (MSA) (see chapter 1) evaluated for the noisy signal (solid line) along with the reference MSA evaluated for the noiseless signal (dot-dashed line). The noisy signal at the NLP output is always aligned, on average, with the input pump SOP, being the MSA constantly equal to 1, for all tested $\mathrm{OSNR}_{\mathrm{in}}$ values. Nonetheless, comparing results in Figs. 4.3 and 4.5(a) proves that a co-propagating NLP, with input signals characterized by a fast-varying SOP, is more sensitive to noise than a counter-propagating NLP.

This is not surprising, given the large difference between the walk-off experienced by pump and probe signals in the two configurations of the NLP. As stated in chapter 2, in a counter-propagating NLP, due to the large walk-off imposed by its geometry, the filter describing the pump-probe nonlinear cross-interactions [65] has such a narrow bandwidth that the pump cannot follow the variation of the probe intensity, also in the noiseless case, but it "sees" only the average probe power. On the other hand, in the co-propagating NLP, the much smaller walk-off (about two bits) makes the filter bandwidth larger [65], so that the pump becomes sensitive to the probe intensity variations imposed by the noise, which thus affect the nonlinear cross-interactions between pump and signal.

It should be remarked that the effectiveness of the co-propagating NLP, just shown for bitwise polarized signals, also extends to signals with longer polarization coherence times, such as those examined in Sec. 4.3.1. For the same system parame-

ters used in Fig. 4.5, I obtained the same DOP values, when increasing the coherence time of the transmitted signal. Such a flexibility of the co-propagating NLP configuration occurs here because the key system parameters (i.e., the duty cycle of the signal and the total walk-off delay between signal and pump) were selected ad hoc, so that each pulse interacts with the pump as if it were propagating alone through the NLP, no matter how many consecutive pulses are transmitted. With the parameters chosen here, it is as if each pulse had a dedicated portion of the pump, with the duration of one bit period T_b, to perform lossless polarization attraction towards the pump SOP. As stated in chapter 3, this is no longer true when the duty cycle of the RZ-OOK modulation increases, since the conditions for the simultaneous achievement of an optimal walk-off ($T_d \simeq 2T_s$) and a proper guard interval between adjacent pulses ($T_b - T_s \geq T_d$) cannot be satisfied. In such a situation, one can design the co-propagating NLP so that it works in the *polarization rotation regime* (see Sec. 3.4, chapter 3), or can employ a counter-propagating NLP, if the signal to be attracted is packetwise polarized and long enough.

4.4 Noise cleaning

After the NLP stage has performed a LPA of the signal towards the pump SOP, the *Pol.* stage yields an OSNR gain by filtering out the orthogonal noisy signal component. In order to estimate the OSNR gain, I resorted to the classical definition of noise figure, $\mathrm{F} = \mathrm{OSNR}_{\mathrm{in}}/\mathrm{OSNR}_{\mathrm{out}}$, and calculated F^{-1}, both before and after the polarizing filter *Pol.*, as depicted in Fig. 4.2(a):

$$\mathrm{F}^{-1}_{\mathrm{pre,post}} = \frac{\mathrm{OSNR}^{\mathrm{pre,post}}_{\mathrm{out}}}{\mathrm{OSNR}_{\mathrm{in}}}. \tag{4.1}$$

All OSNR values were numerically evaluated according to the ITU-T recommendations [69], on a standard reference bandwidth $B_0 = 0.1$ nm. In particular, the noisy signal was first filtered on the signal bandwidth, to get the signal plus noise power $P_T = P_R + P'_N$, then on an outer noise bandwidth, to estimate noise power P_N alone. The output OSNR was eventually evaluated as $\mathrm{OSNR} = (P_T - P_N)/P_N$. Note that the noise power measured on the two bandwidths is the same ($P_N = P'_N$) if and only if the output noise is white. Since the NLP is a nonlinear device, one must expect a colored noise at the output and, accordingly, some mismatches in the measurements.

Fig. 4.6 shows F^{-1} as a function of $\mathrm{OSNR}_{\mathrm{in}}$, obtained for a noise cleaner with a counter- (a) or a co-propagating (b) NLP configuration. In the first case (Fig. 4.6(a)), the input signal is the (isolated) packetwise polarized signal with $T_s = 1$ μs (i.e.,

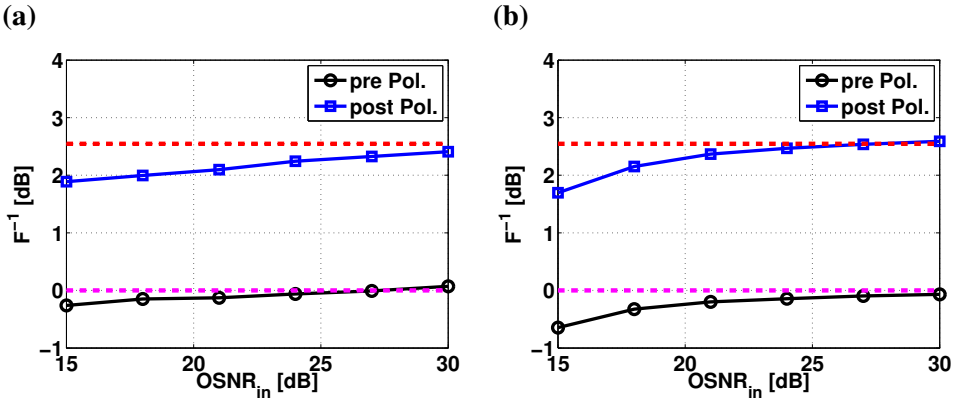

Figure 4.6: Inverse noise figure F^{-1}, evaluated before (pre) and after (post) the polarizing filter, that yields the OSNR Gain. Simulation results are obtained for a noise cleaner with a counter- (a) or a co-propagating (b) NLP configuration.

that used to obtain Fig. 4.3), otherwise the counter-propagating noise cleaner is not effective (since the NLP is not effective, as was numerically verified in chapter 2). In the second case (Fig. 4.6(b)), the input signal is the bitwise polarized signal with 33% RZ-OOK (i.e., that used to obtain Fig. 4.5), although the co-propagating noise cleaner is equally effective for signals with slowly-varying SOP (as was numerically verified), as a consequence of an equally effective repolarization. In both Figs. 4.6(a) and (b), the solid line with circles (black) and that with squares (blue), report the F^{-1} values obtained by measuring $OSNR_{out}$ before or after the *Pol.*, respectively, as evidenced in Fig. 4.2(a) by the blocks labeled "measure $OSNR_{out}^{pre,post}$,,.

The top dashed (red) lines represent an upper limit to the performance of the device, and are located at 2.5 dB and at 2.7 dB, in Figs. 4.6(a) and (b), respectively. As further discussed in Sec. 4.5, such a limit is due to the non ideal polarization control performed by the NLP on the signal, as evidenced by the DOP values in Figs. 4.3 and 4.5. Even in the noiseless case, a DOP < 1 reveals that a portion of the output signal power is still orthogonal to the pump polarization, hence is suppressed by the *Pol.*, along with half of the noise power. If the ideal condition DOP $= 1$ were met by the NLP, the upper limit for the noise cleaner performance would be equal to 3 dB.

On the other hand, the lower dashed (magenta) lines in Figs. 4.6, located at 0 dB, represent the theoretical reference value that should be measured before the polarizing filter *Pol.*. In fact, the measurement of $OSNR_{out}^{pre}$ should yield exactly the same value as $OSNR_{in}$, since, as seen in Fig. 4.2, the noisy input field $E_{tx}(t)$ undergoes

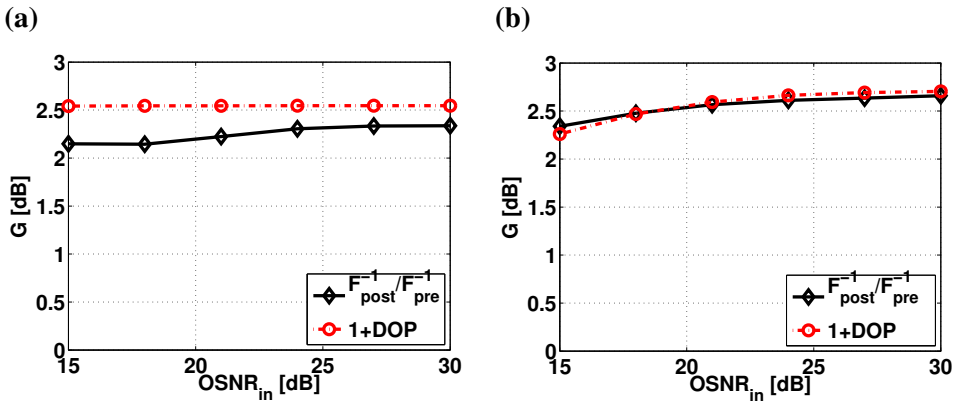

Figure 4.7: Effective OSNR gain, calculated as the increase in the inverse noise figure F^{-1}, due to a noise cleaner with a counter- (a) or a co-propagating (b) NLP configuration. Dashed lines show the results of the theoretical approximation, as a function of input OSNR: $G = 1 + DOP$.

pure phase and polarization distortions, both in the fiber (SPM, XPM, XpolM) and in the phase modulator, up to *Pol.*. **Thus, there is no exchange of energy between the frequency components of signal and noise, hence their power ratio (unaffected by scattering loss) is constant**. However, as lower $OSNR_{in}$ values were tested by increasing the "noise load" P_w, the total transmitted power increases and so does the spectral broadening of the signal (despite SPM compensation). A consequent "leakage" of signal power onto the noise measurement bandwidth yields an overestimation of P_N, at the expense of an underestimated P_T, as I numerically verified, causing an increasing underestimation of $OSNR_{out}$.

Indeed, the artifact described above, that causes the mismatch between simulation results for F^{-1}_{pre} and its theoretical zero value in Fig. 4.6, is related to the standard OSNR measurement technique [69], hence affects both solid curves of each plot in Fig. 4.6. Thus, to get rid of such an artifact, I can estimate the actual OSNR gain G as the difference (in dB) between the solid curves in Fig. 4.6, i.e.,

$$G = \frac{F^{-1}_{post}}{F^{-1}_{pre}} = \frac{OSNR^{post}_{out}}{OSNR^{pre}_{out}}. \tag{4.2}$$

Fig. 4.7 shows G, plotted with solid (black) lines, obtained by a noise cleaner realized with a counter- or a co-propagating NLP configuration (Figs. 4.7(a) and (b), respec-

tively). In both cases, I obtained an OSNR gain between 2 dB and 3 dB, demonstrating that the proposed noise cleaner can effectively regenerate amplitude-modulated optical signals.

4.5 Theoretical approximation

The dashed (red) curves in Fig. 4.7 represent an estimate of G, that can be evaluated from the measurement of the DOP of the signal output by the NLP, as follows.

In addition to the DOP, the effectiveness of a NLP, in the absence of noise, can be quantified by the average fraction ρ of signal power that has the same SOP as the pump (see chapter 1). Being the pump SOP aligned with the polarizing filter *Pol.*, ρ is the fraction of signal energy that passes through *Pol.* in Fig. 4.2 (a). As opposed to a noiseless signal, pure input noise is not attracted and remains unpolarized at the output, as numerically verified, so that 50% of its power is suppressed by *Pol.*. Although linearity does not hold here, I can approximate G as the ratio of attracted signal to noise power: $\rho/0.5$. In the absence of noise ($\mathrm{OSNR_{in}} = \infty$), simulation results showed that $\rho = 0.90$ for the counter-propagating NLP acting on a packetwise-polarized signal (Sec. 4.3.1), while $\rho = 0.93$ results for the co-propagating NLP acting on a bitwise-polarized signal (Sec. 4.3.2). Hence, 90% or 93% of the signal power was attracted towards the pump SOP, in the two scenarios. From these figures, I got the approximate G, equal to $0.90/0.5$ (2.5 dB) and $0.93/0.5$ (2.7 dB), respectively, marked by the upper dashed (red) lines in Figs. 4.6. Further theoretical analysis of LPA in the noiseless case, reported in chapter 1, has shown that the fraction ρ is in turn related to the DOP of the output signal $\overrightarrow{E}_{rx}(t)$, by the simple relationship $\rho = (1 + \mathrm{DOP})/2$, where DOP is obviously evaluated before the *Pol.* (one would trivially get $\mathrm{DOP} = 1$, after the polarizing filter). Still assuming that the output unpolarized noise power is halved by *Pol.*, the approximation derived above for G becomes $\rho/0.5 = (1 + \mathrm{DOP})$, reported in Figs. 4.7 with dashed (red) lines. Note that the OSNR gain estimates in Figs. 4.7(a) and (b) as a function of $\mathrm{OSNR_{in}}$ were evaluated straightforwardly, i.e., by summing 1 to the numerical values in Figs. 4.3 and 4.5 (and converting to the log scale).

As seen in Fig. 4.7, DOP decreases by decreasing $\mathrm{OSNR_{in}}$, as the input noise increases. As stated in Sec. 4.3.2, the degradation of the output DOP is an expected behavior, physically related to the decrease of the input DOP due to the additive noise, despite the repolarization provided by the NLP. In Fig. 4.7, I can see a very good match between the theoretical approximation and the actual OSNR gain reached by the noise cleaner, at least in the co-propagating configuration. Larger discrepancies

are observed in Fig. 4.7(a), for the counter-propagating configuration. The difference between G and its estimate is however below 0.4 dB, compared to OSNR gain values always above 2 dB, in any of the tested configurations, further confirming the noise cleaning capabilities of the proposed device.

4.6 Further practical considerations

In this chapter, I proposed an all-optical fiber-based device, able to accomplish simultaneously both polarization control and noise mitigation of an amplitude-modulated optical signal affected by unpolarized additive noise. Having a NLP at its core, the noise cleaner is conceived for modulated optical signals with single polarization carrier. The proposed device was thought to be applied within an optical link, at the receiver side, once the channel of interest is extracted by the wavelength division multiplexed (WDM) comb. The noise cleaner is based on the simple concept of suppressing the orthogonally polarized half of additive noise, through a polarizing filter, hence ideally reaching a 3 dB enhancement of the OSNR.

The receivers implemented in commercial optical transmission systems, aim at the maximization of the OSNR by filtering the optical signal through an OBPF, before it is photodetected (hence converted in the electrical domain). Such a filter, in addition to selecting the optical channel from the WDM comb, has the important task of suppressing the portion of noise power lying outside the signal bandwidth, while preserving the signal spectrum (hence the useful signal power), as much as possible. Thus, the noise power is discriminated from the signal power based on the frequency components and it is impossible to mitigate noise power within the signal bandwidth without altering the signal spectrum, hence the useful signal power. For the first time, to my knowledge, the presented device offers the possibility to discriminate noise power from signal power by a technique exploiting the polarization, instead of frequency. As a fundamental result, the noise cleaner is able to mitigate not only the noise power outside the signal bandwidth, but also the one within the signal bandwidth, without altering the signal spectrum.

The implementation of a noise cleaner within an optical network would substantially lead to two important practical implications. Assuming a perfect behavior of the device, a 3 dB enhancement of the OSNR at the receiver would allow halving the transmitted signal power, thus increasing the power efficiency of the system, without degrading the receiver performance. On the other hand, the OSNR enhancement could be exploited to extend the reach (e.g., to double the number of amplified spans) of the optical link, while maintaining the same transmitted signal power, again with-

out any degradation of the receiver performance.

As an extension of this work, I have considered the possibility to apply the noise cleaning several times, with the aim of further increases the OSNR gain G, even beyond the 3 dB limit reached by a single device. To this aim, I have conceived to put the noise cleaner in a "loop", so that the noisy signal can passe through it several times before being detected. In such a scenario, since the noise cleaner discriminates noise power from signal power exploiting polarization, once the noisy signal has passed through the noise cleaner the first time, signal and noise are co-polarized, hence there is no way to further discriminate noise from signal unless the pump SOP, hence the SOP towards which the signal is repolarized, is changed in the subsequent passages through the noise cleaner.

Assuming, for instance, to take the (fully-polarized) noisy signal at the output of the noise cleaner, with SOP $\hat{s}_{//}$, and to bring the SOP of the noiseless signal component onto a SOP orthogonal to the one that the noisy signal had at the input, hence towards $\hat{s}_{\perp} \perp \hat{s}_{//}$. Ideally, the noiseless signal component is completely attracted, hence it has SOP $\hat{s}_{\perp}$, while the (fully-polarized) noise is not attracted, hence it has SOP $\hat{s}_{//}$. Thus, the noiseless signal component and noise (both fully-polarized, ideally) have orthogonal SOPs, hence an ideal polarizer aligned with the signal SOP, $\hat{s}_{\perp}$, would remove completely the noise, so as to obtain a noiseless signal (OSNR $= \infty$) at the output of the noise cleaner loop. To achieve this goal, the pump SOP, determining the SOP of the useful signal at the output of the noise cleaner, must be shifted from $\hat{s}_{//}$, at the first noise cleaner passage, to $\hat{s}_{\perp}$, at the following passages. Since the nonlinear cross-polarization interactions between signal and pump reduce to scalar XPM, for orthogonal signal-pump SOPs, the LPA would not work, as already noted. In practice, the attraction from $\hat{s}_{//}$ to the orthogonal SOP $\hat{s}_{\perp}$ needs at least three noise cleaner cycles. In the first passage, the pump attracts the signal SOP towards $\hat{s}_{//}$, then, in the second passage the pump attracts the signal SOP towards a SOP in between $\hat{s}_{//}$ and $\hat{s}_{\perp}$. Finally, in the last passage, the pump attracts the signal SOP towards $\hat{s}_{\perp}$.

Without worrying about the problem of how to change the pump SOP at any loop of the noise cleaner, hence of rotating the ideal polarizer to align it with the pump SOP, I performed several simulations in which the noisy signal travels through the noise cleaner three times, in order to completely delete the noise from the useful signal. Results show that the OSNR obtained by a single noise cleaner is little increased by the following passages through the device.

As another solution to implement a chain of noise cleaner devices, one could think of placing a noise cleaner after each amplifier (e.g., EDFA) along the transmission line, thus creating an "amplifier/noise cleaner" scenario. In this case, the

polarization of the signal would be recovered "span-by-span" and the noise figure of each amplifier would be (ideally) halved. However, in such a scenario, the nonlinear interactions occurring within the NLP would involve the CW pump and the WDM comb. Of course, in a WDM system the nonlinear interaction involves the pump and N>1 channels, hence it is no longer a two-channel phenomenon, as in classical LPA. To the best of my knowledge, no one has ever studied LPA within a WDM system.

Conclusions

Within the research activity performed during my Ph.D., I investigated an *all-optical fiber-based* device for the *ultra-fast* control of the polarization of optical signals. Such a device is thought to be implemented within the *transparent all-optical networks* of future generation. Within these networks, the processing and the regeneration of the signal will be performed in the optical domain, as opposed to the current optical networks where the processing/regeneration is performed in the electrical domain, thus providing an increase in the processing speed and in the overall network bandwidth.

Among the different polarization controller devices that can be taken in consideration (e.g., ideal polarizer, polarizer based on photorefractive materials, active polarizer, *etc.*), I focused my attention on the (fiber-based) nonlinear lossless polarizer (NLP), that is the most recently investigated technology, with experimental demonstration appearing only few years ago [2, 6]. Since the NLP allows to perform a fast control of the polarization, while preserving the signal intensity, it represents a promising solution to be employed in transparent all-optical networks of future generation. In particular, the NLP performs polarization control by exploiting the physical phenomenon of *lossless polarization attraction* (LPA). LPA is a Kerr-based phenomenon, generated by the nonlinear *cross-polarization modulation* (XpolM) interaction between a (possibly depolarized) optical signal (whose polarization has to be controlled) and a fully polarized continuous wave (CW) pump laser. Whatever the input signal polarization, the output signal polarization is attracted towards the pump polarization, without any loss of power, due to polarization rotation. The fully-polarized CW pump, in designing a NLP device, can be either injected at the opposite fiber end with respect to the signal, thus implementing a *counter-propagating NLP*, or at the same fiber end with respect to the signal, thus implementing a *co-propagating NLP*.

In my Ph.D., I investigated the original counter-propagating configuration of the NLP and I contributed massively to the introduction of the co-propagating config-

uration, which has been proved to be more flexible and power efficient. Moreover, based on the NLP, I proposed a novel all-optical *noise cleaning* device able to almost double the optical signal-to-noise ratio of a (possibly depolarized) signal affected by unpolarized additive noise.

Regarding the counter-propagating NLP, I characterized, by numerical simulation, the performance of the device, when its free parameters (signal and pump power; nonlinear fiber length) are varied. To simulate the counter-propagation of optical signals, I introduced a novel iterative algorithm, named SCAOS, based on the split-step Fourier method. Moreover, I introduced the degree of attraction (DOA), which is an analytical instruments that allows to quantify the polarization attraction, highlighting the trade-off between the mean polarization attraction and an inevitable DOP degradation. I found that the attraction of the signal polarization towards that of a counter-propagating CW pump increases with the pump-signal power product, which allows the designer to trade power between signal and pump. The results found on the average attraction of randomly polarized signals yield the rule for setting the power levels. Although longer fibers increase the performance of the device, length should be limited by the possible presence of PMD. Results show that fiber lengths beyond 10 km only yield a marginal improvement on performance. Anyway, the original counter-propagating configuration of the NLP requires long (microseconds) transient time and large signals power (watts), due to the relative propagation velocity between signal and pump imposed by the geometry, that is fixed and relativistic (i.e., equal to the speed of light). As a consequence, a counter-propagating NLP can repolarize only powerful signals with a slowly-varying polarization.

In order to exploit the additional degree of freedom given by the relative propagation velocity between signal and pump, i.e., the signal-pump walk-off, I introduced the NLP designed in co-propagating configuration. In particular, I characterized the performance of the co-propagating NLP as a function of relative propagation velocity between signal and pump. I demonstrated that a scaling rule exists, so that the optimal performance (DOP) can be achieved for any signal pulse duration, provided that the signal-pump walk-off is tuned accordingly, by placing the pump at an optimal wavelength. As a consequence, I showed that the *polarization attraction regime* occurs only when the Kerr nonlinearity and the walk-off are carefully balanced. In such a case, the signal polarization evolves along a spiral trajectory, ideally collapsing onto the pump SOP. On the other hand, when the signal-pump walk-off is too small or to large with respect to the *optimal* walk-off, the NLP operates in the *polarization rotation regime*, where the signal polarization evolves along a circular trajectory, that never results in a genuine polarization attraction. However, I showed that an NLP

operating in the polarization rotation regime, when signal-pump walk-off is zero, can be designed so as to provide an effective polarization control. Moreover, I studied the impact of the polarization mode dispersion (PMD) on the performance of the NLP whenever a randomly birefringent telecom fiber is employed for the repolarization process. The presence of a small amount of PMD, such as that brought about by recently manufactured fibers, does not substantially alter the performance of the NLP and is well tolerated even in the case of the longest tested fiber. On the other hand, a further increase of PMD, for instance due to the use of legacy fibers with a relatively large PMD coefficient, causes a degradation of the NLP performance. Finally, I proposed to replace the powerful pump laser, employed to generate LPA, with two (or more) pump lasers, less powerful hence less expansive, thus implementing a *multi-pump NLP* device. Although results reported in this thesis represent a "proof of principle" for a *multi-pump NLP* device (since they are early results that need further investigations), they prove that such a solution could be feasible.

Last but not least, the proposed noise cleaner device is based on the simple concept of suppressing the orthogonally polarized half of additive noise through a polarizing filter, hence ideally reaching a 3 dB enhancement of the OSNR. The discrimination of noise power from signal power relies on the polarization; hence, the device is able to mitigate even noise power lying within the signal bandwidth, while fully preserving signal power. I tested, by numerical simulations, the device realized with both configurations of the NLP and applied them to the noise cleaning of signals with amplitude modulation at 10 Gb/s and with different speeds of variation of their polarization (i.e., different polarization coherence time). Results show that signals with a polarization that is constant over thousands of bits (i.e., for packetwise-polarized signals) benefit by both configurations of the noise cleaner, with an effective gain of the OSNR between 2 and 3 dB, at least for the input OSNR values of practical interest. A similar gain was obtained as well for signals with a fast-varying polarization, on the scale of a bit period (i.e., for bitwise-polarized signals), by resorting to the co-propagating configuration of the noise cleaner. I showed that the achieved OSNR gain is strictly related to the performance of the NLP and can be theoretically estimated after measuring the DOP of signals at its output.

Note that signal repolarization is detrimental, if applied to polarization multiplexed formats, hence we can apply the NLP device to optical signals with single polarization modulation formats. Consistently, I concentrated on signals with a "legacy" binary amplitude modulation format, i.e., on-off keying (OOK). Despite the introduction, in the last decade, of polarization multiplexed formats in high-speed (100 Gb/s) coherent optical systems, the 10 Gb/s – OOK remains the most widespread format

in nowadays optical networks scenario. Thus, although in the coming years it is expected that the 100 Gb/s market will overtake the incomes of 10 Gb/s systems, in the transport networks, 10 Gb/s-OOK networks will still be used for many years, both in transport networks as well as in future metropolitan area networks. Moreover, although phase modulation formats (e.g., PSK and QPSK) with single polarization carrier are rarely implemented, the presented device could be employed also with such formats. I conjecture that the effectiveness of the NLP could even increase, in this case, since the CW pump would interact with a signal characterized by constant intensity.

Appendix A

Useful matrix properties

Pauli matrices

In the context of Polarimetry[1], *Pauli matrices* are defined as

$$\sigma_0 = \begin{bmatrix} 1 & 0 \\ 0 & 1 \end{bmatrix}; \sigma_1 = \begin{bmatrix} 1 & 0 \\ 0 & -1 \end{bmatrix}; \sigma_2 = \begin{bmatrix} 0 & 1 \\ 1 & 0 \end{bmatrix}; \sigma_3 = \begin{bmatrix} 0 & -j \\ j & 0 \end{bmatrix}, \quad \text{(A.1)}$$

which represent a basis for all 2×2 complex matrices; the first matrix σ_0 is the 2×2 identity matrix (often identified by I). The Pauli matrices are *hermitian*, hence $\sigma_i = \sigma_i^\dagger$ (with $i = 0, ..., 3$), where $\dagger$ represents the adjoint operator, i.e., the transposed and conjugate of a vector or matrix.

Projector matrix

The *projector matrix* of the Jones vector $\overrightarrow{A}$ is defined as the 2×2 matrix $P_A \triangleq \overrightarrow{A}\overrightarrow{A}^\dagger$. By resorting to the Pauli matrices σ_i, with $i = 0, ..., 3$, the projector matrix P_A can be written as a function of the Stokes vector $\overrightarrow{a} = [a_1, a_2, a_3]^T$, corresponding to the Jones vector $\overrightarrow{A}$, as

$$P_A = \frac{1}{2} a_0 \sigma_0 + \frac{1}{2} \overrightarrow{a} \cdot \overrightarrow{\sigma}. \quad \text{(A.2)}$$

[1] In the context of Quantum Mechanics, the matrices σ_1, σ_2, σ_3 are often defined with a permutation of indices, such that $\sigma_1 = \begin{bmatrix} 1 & 0 \\ 0 & 1 \end{bmatrix}$ and so forth.

In (A.2), a_0 represents the magnitude of the Stokes vector $\overrightarrow{a}$, hence $a_0 = \| \overrightarrow{a} \|$, while $\overrightarrow{\sigma} \triangleq [\sigma_1, \sigma_2, \sigma_3]^T$ is the *spin vector*, so that $\overrightarrow{a} \cdot \overrightarrow{\sigma} = \sum_{i=1}^{3} a_i \sigma_i$.

Similarly, the *transposed projector matrix* of the Jones vector $\overrightarrow{A}$ is defined as the 2×2 matrix $P_A^T \triangleq \overrightarrow{A}^* \overrightarrow{A}^T$. By resorting to the properties of the Pauli matrices for which $\sigma_i^T = \sigma_i$ $(i = 0, 1, 2)$, while $\sigma_3^T = -\sigma_3$, the transposed projector matrix P_A^T can be expressed as a function of the projector matrix P_A, as $P_A^T = P_A - a_3 \sigma_3$.

Equation of motion

The propagation equation of a Jones vector $\overrightarrow{A}$ can be written, in a general form, as [71]

$$\frac{\partial \overrightarrow{A}}{\partial z} = -\frac{j}{2} \mathbf{H} \overrightarrow{A},$$

where $\mathbf{H} = h_0 \sigma_0 + \overrightarrow{h} \cdot \overrightarrow{\sigma}$ is a 2×2 matrix, decomposed with its Pauli coordinates $\overrightarrow{h} = [h_1, h_2, h_3]^T \in \mathbb{R}$ and $h_0 = h_{0r} + j h_{0i} \in \mathbb{C}$. The equation of motion of the Stokes vector $\overrightarrow{a}$, corresponding to the Jones vector $\overrightarrow{A}$, results [71]

$$\frac{\partial \overrightarrow{a}}{\partial z} = \overrightarrow{h} \times \overrightarrow{a} + h_{0i} \overrightarrow{a}.$$

If $\overrightarrow{h}$ is complex, an extra term appears, including $\Im \left\{ \overrightarrow{h} \right\}$, which is related to polarization dependent loss (PDL) [71], not considered here.

Bibliography

[1] A. A. M. Saleh and J. M. Simmons, "All-Optical networking – evolution, benefits, challenges, and future vision," Proc. of IEEE, vol. 100, pp. 1105-1117 (2012).

[2] J. Fatome, S. Pitois, P. Morin, and G. Millot, "Observation of light-by-light polarization control and stabilization in optical fibre for telecommunication applications," Opt. Express, vol. 18, pp. 15311-15317 (2010).

[3] G. Millot and S. Wabnitz, "Nonlinear polarization effects in optical fibers: polarization attraction and modulation instability," J. Opt. Soc. Am. B, vol. 31, pp. 2754-2768 (2014).

[4] G. P. Agrawal, *Nonlinear Fiber Optics*, 4th ed., Academic Press, New York (2007).

[5] G. P. Agrawal, *Applications of Nonlinear Fiber Optics*, 2nd ed., Academic Press, New York (2008).

[6] S. Pitois, J. Fatome, and G. Millot, "Polarization attraction using counterpropagating waves in optical fiber at telecommunication wavelengths," Opt. Express, vol. 16, pp. 6646–6651 (2008).

[7] K. Cvecek, K. Sponsel, R. Ludwig, C. Schubert, C. Stephan, G. Onishchukov, B. Schmauss, and G. Leuchs, "2R-Regeneration of an 80-Gb/s RZ-DQPSK signal by a nonlinear amplifying loop mirror," IEEE Photon. Technol. Lett., vol. 19, pp. 146–148 (2007).

[8] S. Boscolo, S. K. Turitsyn, and K. J. Blow, "Nonlinear loop mirror-based all-optical signal processing in fiber-optic communications," Opt. Fiber Technol., available online (2008).

[9] E. Ciaramella, F. Curti and S. Trillo, "All-optical signal reshaping by means of four-wave mixing in optical fibers," IEEE Photon. Technol. Lett., vol. 13, pp. 142–144 (2001).

[10] P. Honzatko, A. Kumpera, and P. Skoda, "Effects of polarization dependent gain and dynamic birefringence of the SOA on the performance of the ultrafast nonlinear interferometer gate, " Opt. Express, vol. 15, pp. 2541-2547 (2007).

[11] Y. Takahashi, A. Neogi, H. Kawaguchi, "Polarization dependent nonlinear gain in semiconductor optical amplifiers," J. Quantum Electron., vol. 34, pp. 1660–1672 (1998).

[12] R. Noe, H. Heidrich, and D. Hoffmann, "Endless polarization control systems for coherent optics," J. Lightwave Technol., vol 6, pp. 1199–1208 (1988).

[13] N. G. Walker and G. R. Walker, "Polarization control for coherent communications," J. Lightwave Technol., vol. 8, pp. 438–458 (1990).

[14] M. Martinelli, P. Martelli, and S. M. Pietralunga, "Polarization stabilization in optical communications systems," J. Lightwave Technol., vol. 24, pp. 4172–4183 (2006).

[15] B. Koch, R. Noe, V. Mirvoda, H. Griesser, S. Bayer, and H. Wernz, "Record 59 krad/s polarization tracking in 112 Gb/s 640 km PDMRZ- DQPSK transmission," IEEE Photon. Technol. Lett., vol. 22, pp. 1407–1409 (2010).

[16] N. Rossi, P. Serena, and A. Bononi, "Stratified-sampling estimation of PDL-induced outage probability in nonlinear coherent systems," J. Lightwave Technol., vol. 32, pp. 4905-4911 (2014).

[17] J. E. Heebner, R. S. Bennink, R. W. Boyd, and R. A. Fisher, "Conversion of unpolarized light to polarized light with greater than 50% efficiency by photorefractive two-beam coupling," Opt. Lett., vol. 25, pp. 257–259 (2000).

[18] S. Popov and E. Vanin, "Polarization dependence of Raman gain on propagation direction of pump and probe signal in optical fibers," in *Proceedings of Laser and Electro-Optics (CLEO) 2001*, Baltimore (USA), paper CTuJ5.

[19] S. Popov, S. Sergeyev, and A. T. Friberg, "The impact of pump polarization on the polarization dependence of the Raman gain due to the breaking of a fiber's circular symmetry," J. Opt. A: Pure Appl. Opt., vol. 6, S72 (2004).

[20] M. Martinelli, M. Cirigliano, M. Ferrario, L. Marazzi, and P. Martelli, "Evidence of Raman-induced polarization pulling," Opt. Express, vol. 17, pp. 947-955 (2009).

[21] L. Ursini, M. Santagiustina, and L. Palmieri, "Raman nonlinear polarization pulling in the pump depleted regime in randomly birefringent fibers," IEEE Photon. Technol. Lett., vol. 23, pp. 254-256 (2011).

[22] S. V. Sergeyev, "Activated polarization pulling and de-correlation of signal and pump states of polarization in a fiber Raman amplifier," Opt. Express, vol. 19, pp. 24268-24279 (2011).

[23] S. Sergeyev and S. Popov, "Two-section fiber optic Raman polarizer," IEEE J. Quantum Electron., vol. 48, pp. 56-60 (2012).

[24] S. Sergeyev, S. Popov, and A. T. Friberg, "Virtually isotropic transmission media with fiber Raman amplifier," IEEE J. Quantum Electron., vol. 46, pp. 1492-1497 (2010).

[25] N. J. Muga, M. F. S. Ferreira, and A. N. Pinto, "Broadband polarization pulling using Raman amplification," Opt. Express, vol. 19, pp. 18707-18712 (2011).

[26] F. Chiariello, L. Ursini, L. Palmieri, and M. Santagiustina, "Polarization attraction in counterpropagating fiber Raman amplifiers," IEEE Photon. Technol. Lett., vol. 23, pp. 1457-1459 (2011).

[27] P. Morin, S. Pitois, and J. Fatome, "Simultaneous polarization attraction and Raman amplification of a light beam in optical fibers," J. Opt. Soc. Am. B, vol. 29, pp. 2046-2052 (2012).

[28] A. Zadok, E. Zilka, A. Eyal, L. Thévenaz, and M. Tur, "Vector analysis of stimulated Brillouin scattering amplification in standard single-mode fibers," Opt. Express, vol. 16, pp. 21692-21707 (2008).

[29] J. Fatome, S. Pitois, and G. Millot, "Experimental evidence of Brillouin-induced polarization wheeling in highly birefringent optical fibers," Opt. Express, vol. 17, pp. 12612 (2009).

[30] Z. Shmilovitch, N. Primerov, A. Zadok, A. Eyal, S. Chin, L. Thévenaz, and M. Tur, "Dual-pump push-pull polarization control using stimulated Brillouin scattering," Opt. Express, vol. 19, pp. 25873–25880 (2011).

[31] J. F. L. Freitas, C. J. S. de Matos, M. B. Costa e Silva, and A. S. L. Gomes, "Impact of phase modulation and parametric gain on signal polarization in an anomalously dispersive optical fiber," J. Opt. Soc. Am. B, vol. 24, pp. 1469–1474 (2007).

[32] M. Guasoni, V. V. Kozlov, and S. Wabnitz, "Theory of polarization attraction in parametric amplifiers based on telecommunication fibers," J. Opt. Soc. Am. B, vol. 29, pp. 2710–2720 (2012).

[33] B. Stiller, P. Morin, D. M. Nguyen, J. Fatome, S. Pitois, E. Lantz, H. Maillotte, C. R. Menyuk, and T. Sylvestre, "Demonstration of polarization pulling using a fiber-optic parametric amplifier," Opt. Express, vol. 20, pp. 27248–27253 (2012).

[34] M. Barozzi and A. Vannucci, "Optimal pump wavelength placement in lossless polarization attraction," in *Proceedings of Fotonica 2013* (AEIT - Federazione Italiana di Elettrotecnica, Elettronica, Automazione, Informatica e Telecomunicazioni), Milano (Italy), paper P.12 (2013).

[35] V. V. Kozlov and S. Wabnitz, "Theoretical study of polarization attraction in high-birefringence and spun fibers," Opt. Lett., vol. 35, pp. 3949-3951 (2010).

[36] E. Assémat, S. Lagrange, A. Picozzi, H. R. Jauslin, and D. Sugny, "Complete nonlinear polarization control in an optical fiber system," Opt. Lett., vol. 35, pp. 2025-2028 (2010).

[37] S. Lagrange, D. Sugny, A. Picozzi, and H. R. Jauslin, "Singular tori as attractors of four-wave-interaction systems," Phys. Rev. E, vol. 81, pp. 016202 (2010).

[38] V. V. Kozlov, J. Nuño, and S. Wabnitz, "Theory of lossless polarization attraction in telecommunication fibers," J. Opt. Soc. Am. B, vol. 28, pp. 100-108 (2011).

[39] E. Assémat, D. Dargent, A. Picozzi, H. R. Jauslin, and D. Sugny, "Polarization control in spun and telecommunication optical fibers," Opt. Lett., vol. 36, pp. 4038-4040 (2011).

[40] E. Assémat, A. Picozzi, H. R. Jauslin, and D. Sungy, "Hamiltonian tools for the analysis of optical polarization control," J. Opt. Soc. Am. B, vol. 29, pp. 559-571 (2012).

[41] V. V. Kozlov, J. Fatome, P. Morin, S. Pitois, G. Millot, and S. Wabnitz, "Nonlinear repolarization dynamics in optical fibers: transient polarization attraction," J. Opt. Soc. Am. B, vol. 28, pp. 1782-1791 (2011).

[42] M. Barozzi and A. Vannucci, "Performance analysis of lossless polarization attractors," in *Latin America Optics and Photonics Conference*, OSA Technical Digest (online), São Sebastião (Brasil), paper LM3C.4 (2012).

[43] M. Barozzi, A. Vannucci, and D. Sperti, "A simple counterpropagation algorithm for optical signals (SCAOS) to simulate polarization attraction," in *Proceedings to Fotonica 2012* (AEIT - Federazione Italiana di Elettrotecnica, Elettronica, Automazione, Informatica e Telecomunicazioni), Firenze (Italy), paper A6.4 (2012).

[44] M. Barozzi, A. Vannucci, and D. Sperti, "Lossless polarization attraction simulation with a novel and simple counterpropagation algorithm for optical signals," J. Europ. Opt. Soc. Rap. Public., vol. 7, pp. 12042 (2012).

[45] V. V. Kozlov, M. Barozzi, A. Vannucci, and S. Wabnitz, "Lossless polarization attraction of copropagating beams in telecom fibers," J. Opt. Soc. Am. B, vol. 30, pp. 530–540 (2013).

[46] M. Barozzi and A. Vannucci, "Performance characterization and guidelines for the design of a counter-propagating nonlinear lossless polarizer," J. Opt. Soc. Am. B, vol. 30, pp. 3102–3112 (2013).

[47] P. Morin, J. Fatome, C. Finot, S. Pitois, R. Claveau, and G. Millot, "All-optical nonlinear processing of both polarization state and intensity profile for 40 Gbit/s regeneration applications," Opt. Express, vol. 19, pp. 17158-17166 (2011).

[48] J. Fatome, S. Pitois, P. Morin, E. Assémat, D. Sungy, A. Picozzi, H. R. Jauslin, G. Millot, V. V. Kozlov, and S. Wabnitz, "A universal optical all-fiber omnipolarizer," Scientific Rep., DOI 10.1038 (2012).

[49] P. Y. Bony, M. Guasoni, E. Assémat, S. Pitois, D. Sugny, A. Picozzi, H. R. Jauslin, and J. Fatome, "Optical flip–flop memory and data packet switching operation based on polarization bistability in a telecommunication optical fiber," J. Opt. Soc. Am. B, vol. 30, pp. 2318–2325 (2013).

[50] M. Barozzi and A. Vannucci, "A novel device to enhance the OSNR based on lossless polarization attraction," in *Proceedings of Fotonica 2013* (AEIT -

Federazione Italiana di Elettrotecnica, Elettronica, Automazione, Informatica e Telecomunicazioni), Milano (Italy), paper C6.5 (2013).

[51] M. Barozzi and A. Vannucci, "All-optical noise cleaning based on co-propagating lossless polarization attraction," in *Proceedings of IEEE International Conference on Photonics (ICP 2013)*, Melaka (Malaysia), paper D3-AM1-C.2 (2013).

[52] M. Barozzi, A. Vannucci, and G. Picchi, "All-optical polarization control and noise cleaning based on a nonlinear lossless polarizer," in *Proceedings of SPIE – volume on Photonics, Devices and Systems VI*, Prague (Czech Republic), doc. ID PPR100-71 (2015, to be published).

[53] M. Barozzi and A. Vannucci, "Lossless polarization attraction of telecom signals: application to all-optical OSNR enhancement," J. Opt. Soc. Am. B, vol. 31, pp. 2712-2720 (2014).

[54] R. C. Jones, "A new calculus for the treatment of optical systems," JOSA, vol. 31, pp. 488-493 (1941).

[55] S. Huard, *Polarisation de la lumière*, Masson Ed., Paris (1994).

[56] C. R. Menyuk, "Pulse propagation in an elliptically birefringent Kerr medium," IEEE J. Quantum Electron., vol 25, pp. 2674-2682 (1989).

[57] P. K. A. Wai and C. R. Manyuk, "Polarization mode dispersion, decorrelation, and diffusion in optical fibers with randomly varying birefringence," J. Lightwave Technol., vol. 14, pp. 148-157 (1996).

[58] D. Marcuse, C. R. Menyuk, and P. K. A. Wai, "Application of the Manakov-PMD equation to studies propagation in optical fibers with randomly varying birefringence," J. Lightwave Technol., vol. 15, pp. 1735-1746 (1997).

[59] V. V. Kozlov, K. Turitsyn, and S. Wabnitz, "Nonlinear repolarization in optical fibers: polarization attraction with copropagating beams," Opt. Lett., vol. 36, pp. 4050-4052 (2011).

[60] A. Bononi, A. Vannucci, A. Orlandini, E. Corbel, S. Lanne, and S. Bigo, "Degree of polarization degradation due to cross-polarization modulation and its impact on polarization-mode dispersion compensator," J. Lightwave Technol., vol. 21, pp. 1903-1913 (2003).

[61] D. Breuer, H.-J. Tessmann, A. Gladisch, H. M. Foisel, G. Neumann, H. Reiner, and H. Cremer, "Measurements of PMD in the installed fiber plant of Deutsche Telekom," in *IEEE LEOS Summer Topical Meetings*, Vancouver (Canada), pp. MB2.1–MB2.2 (2003).

[62] P. Serena, M. Bertolini, and A. Vannucci, *Optilux toolbox*, http://optilux.sourceforge.net/Documentation/optilux_doc.pdf.

[63] W. H. Press, S. A. Teukolsky, W. T. Vetterling, B. P. Flannery, *Numerical Recipes in C*, 2nd ed., Cambridge University Press, Cambridge (1992).

[64] C. D. Poole and D. L. Favin, "Polarization-mode dispersion measurements based on transmission spectra through a polarizer," IEEE J. Lightwave Technol., vol. 12, pp. 917–929 (1994).

[65] G. Bellotti, M. Varani, C. Francia, and A. Bononi, "Intensity distortion induced by cross-phase modulation and chromatic dispersion in optical-fiber transmission with dispersion compensation," IEEE Photon. Technol. Lett., vol. 10, pp. 1745-1747 (1998)

[66] K. Turitsyn and S. Wabnitz, "Stability analysis of polarization attraction in optical fibers," Opt. Commun., vol 307, pp. 62-66 (2013).

[67] A. Bononi and A. Vannucci, "Is there life beyond the principal states of polarization?," Opt. Fiber Technol., vol. 8, pp. 257–294 (2002).

[68] M. Guasoni, J. Fatome, and S. Wabnitz, "Intensity noise-driven nonlinear fiber polarization scrambler," Opt. Lett., vol. 39, pp. 5309-5312 (2014).

[69] *Optical system design and engineering considerations*, ITU-T Series G Supplement 39 (09/2012).

[70] C. Xu, L. Mollenauer, and L. Xiang, "Compensation of nonlinear self-phase modulation with phase modulator," Electron. Lett., vol. 38, pp. 1578–1579 (2002).

[71] N. J. Frigo, "A generalized geometrical representation of coupled mode theory," IEEE J. Quantum Electron., vol. QE-22, pp. 2131-2140 (1986).

Acknowledgments

I wish to thank, in particular, my supervisor, Chiar.mo Prof. Armando Vannucci, for the continues inspiration and the fruitful collaboration.

Part of this work was performed within the PRIN2008 (Programma Di Ricerca Scientifica di Rilevante Interesse Nazionale 2008) project “Non-linear cross-polarization interactions in photonic devices and systems (POLARIZON)”, financially supported by Ministero dell’Istruzione, dell’Università e della Ricerca (MIUR).